EFFECTS OF TEMPERATURE AND DISSOLVED $LiClO_4$ ON THE VISCOELASTIC AND DYNAMIC PROPERTIES OF POLY(ETHYLENE OXIDE), (PEO) MELTS

by

Radoslav B. Bogoslovov

Master of Science in Physics
University of Nevada, Las Vegas, Las Vegas, Nevada
2003

Master of Science in Engineering Physics
Sofia University, Sofia, Bulgaria
1996

A dissertation submitted in partial fulfillment
of the requirements for the

Doctor of Philosophy Degree in Physics
Department of Physics
College of Sciences

Graduate College
University of Nevada, Las Vegas
December 2005

– Thesis Approval Page –

ABSTRACT

Effects of Temperature and Dissolved $LiClO_4$ on the Viscoelastic and Dynamic Properties of Poly(ethylene Oxide), (PEO) Melts

by

Radoslav B. Bogoslovov

Dr. James Selser, Examination Committee Chair
Professor of Physics
University of Nevada, Las Vegas

Poly(ethylene oxide)/lithium perchlorate ($PEO/LiClO_4$) complexes are widely studied as a prototype solid polymer electrolyte in rechargeable lithium-polymer batteries. Characterizing the structure and dynamics of the system in its molten state is important for understanding the role of the polymer environment in lithium ion transport and conductivity. A fiber-optic coupled Fabry-Perot interferometer is employed in the investigation of the electrolyte viscoelastic and dynamic properties, which are both related to the intrachain local mobility and therefore to ion diffusion. The properties of the system are studied as a function of composition, temperature, and frequency. Structural relaxation processes are observed both in the neat polymer melt and in the salt containing electrolytes. For the neat PEO-1K melt the relaxation is identified as Maxwell-Debye single-exponential relaxation ($\beta = 1$). The relaxation time follows Arrhenius temperature dependence with activation energy of the order of 10-11 kJ/mol.

Upon addition of salt, the character of the relaxation persists with $\beta = 1$, while the characteristic relaxation time slows down and the activation energy increases slightly. The slowdown of the dynamics is more pronounced at lower temperatures. In addition, with increasing salt concentration the elastic modulus increases significantly making the system stiffer at all temperatures, while the maximum of the storage modulus is shifted to higher temperatures. These effects result in a decrease in polymer segmental mobility and consequently in reduction of lithium ion diffusivity, with increased salt concentration. A unique *q*-dependent measurement is performed, allowing the investigation of the Brillouin frequency and linewidth as a function of frequency. It revealed a double-step relaxation in the electrolyte. The two relaxations are identified as secondary relaxations with Maxwell-Debye character ($\beta = 1$). The lower-frequency relaxation is stronger and has Arrhenius temperature behavior of the relaxation time. It is attributed to conformal fluctuations of the chain segments between transient crosslinks formed by the EO-Li^+ complexation in the melt. The higher-frequency relaxation is weaker, especially at higher temperatures and more difficult to resolve. It is possible it results from librational motions or conformal rearrangements of the uncomplexed polymer dihedrals and seems to be strongly affected by the specifics of the local chain conformation and the EO-Li^+ complexation in the melt.

TABLE OF CONTENTS

LIST OF FIGURES

ACKNOWLEDGEMENTS

It is a pleasure to thank my advisor, Dr. James Selser and my committee member, Dr. David Shelton for their guidance, valuable discussions and support during the completion of this project. I also thank my committee members, Dr. Stephen Lepp and Dr. Boyd Earl.

I thank the U.S. DOE (Office of Basic Energy Sciences) Grant No. DE-FG03-00ER15052, UNLV, and the Bigelow Foundation for financially supporting this work. In addition, I thank A. Sanchez, W. O'Donnell, and J. Norton for technical support. I also thank Dr. R. Pecora and Dr. G. D. Patterson for providing additional components for the F-P interferometer as well as for valuable discussions.

Finally, I want to thank my family and especially my wife Ana for their support and encouragement as well as Prof. Chris Stojanoff who gave my graduate studies an excellent start and direction.

CHAPTER 1

INTRODUCTION

Solid polymer electrolytes (SPEs) are an important class of conducting solid-state ionic materials. Among a variety of applications in electrochemical devices, they show significant potential in secondary (rechargeable) lithium/polymer batteries. Polymer electrolytes exhibit a number of advantages over conventional liquid electrolytes. For example, the viscoelasticity of polymers combines both solid-like and liquid-like properties, making them particularly suited to commercial applications. Batteries based on SPEs are compact, lightweight, durable and safe. Since they comprise the mechanical and technological properties of plastics, they can be formed and molded in complex shapes and structures and are subject to well developed and cost effective manufacturing techniques. The prototypes as well as the first commercial batteries showed high-capacity, high power densities and good charge-discharge characteristics. Some of the possible applications of this type of batteries include off-peak power storage, lightweight power supplies in electric and hybrid vehicles, batteries for portable electronic devices, backup power supplies, etc. An example of a working battery of this type already on the market is the one developed by *Avestor* (Boucherville, Quebec, Canada) – a company created as a partnership between two major energy industry corporations, *Hydro-Québec* (Canada) and *Kerr-McGee* (USA).[1]

One of the most studied systems for SPEs is poly(ethylene oxide) (PEO) complexed by lithium perchlorate ($LiClO_4$). At room temperature, PEO is in a bi-phasic semi-crystalline state. It is characterized by glass transition temperature of about –40^oC and melting temperature of the crystalline phase of about 60^oC (for high molecular weight PEO). Below the melting point, the PEO/$LiClO_4$ complex also consists of both fluid amorphous regions and salt enriched crystalline regions.[2] It was shown that lithium ion transport occurs exclusively in the amorphous, non-crystallized regions of the polymer host.[3] It was also found that the conductivity of PEO/$LiClO_4$ electrolytes reaches practically useful values (of about 10^{-4} S/cm) only at temperatures of 60-80^oC, or higher. Adding liquid plasticizers (to lower the operational temperature) promotes deterioration of the electrolyte's mechanical properties and increases its reactivity towards the lithium metal anode. These considerations have led to the concept of a "dry" (plasticizer-free) and "warm" (operating temperatures between 60^oC and 80^oC) polymer battery. This concept is implemented in the battery by *Avestor* mentioned above. For these reasons, the present study is focused exclusively on the molten state of the system.

Despite remarkable progress in the last decade toward designing lithium/polymer batteries and the considerable body of experimental and theoretical research in the area, there is still a lack of understanding of the mechanism that the polymer host plays in battery ion transport. Although the details are not yet fully understood, it is widely accepted that lithium ions are coordinated with several ether oxygen atoms belonging to a single or multiple adjacent polymer chains. They are transported through the system via re-coordination with other ether oxygens.[4,5] Better understanding of the processes on a fundamental level will ultimately lead to higher performance and better design of

polymer batteries. For example, formation and disruption of coordination bonds should be accompanied by relaxations of the local chain structure. Librational motion and conformational transitions of the polymer backbone dihedrals will also be evidenced by relaxations. Accordingly, some of the parameters of interest include the time scales, the energy barriers, and the temperature and frequency dependence of these relaxations. On a much larger length scale, dipole-dipole interactions result in the formation of a transient network structure in the pure polymer melt, which, is evidenced by collective relaxation modes. Upon addition of salt, this network structure is enhanced by the lithium-oxygen interactions. Both phenomena can be studied non-invasively by dynamic light-scattering techniques.

In recent years, our research group has been involved in extensive studies of the bulk properties of molten PEO and PEO-melt/$LiClO_4$ solutions. Both the structure and dynamic behavior of these systems have been investigated at various temperatures, for a range of salt concentrations, and for two different polymer molecular weights.[6,7,8,9] In our studies, we employ both static light-scattering (SLS) and dynamic light-scattering (DLS) techniques, including photon correlation spectroscopy (PCS) and Rayleigh-Brillouin light scattering. Analysis by PCS of the light scattered by density fluctuations in the molten PEO revealed long-ranged structure. It was identified as a transient physical network formed by the polymer in the melt. The structure persisted for temperatures throughout our experimental range (up to 140^{o}C) and after the addition of $LiClO_4$ (at least for salt concentrations up to 28 weight percent). The results for PEO-1K were interpreted in terms of the behavior of a random elastic PEO network immersed in a viscous PEO damping liquid. The studies were corroborated by viscometry and rheometry experiments

performed in parallel with the light-scattering experiments. They revealed that the network and the liquid component are strongly coupled and the diffusive motions of the network component are strongly damped by the viscous liquid component (overdamped system). As a model system, the "wet gel" model similar to that investigated by T. Tanaka, *et al.*[10] was used.

Recently, Rayleigh-Brillouin dynamic light-scattering measurements using a Fabry-Perot (F-P) interferometer were initiated. This technique allows studies of both the viscoelastic properties as well as the structural relaxation dynamics of the polymer melt and polymer/salt complexes, which are both related to the polymer chain local mobility and therefore to the Li^+ ion diffusion. As earlier studies[11,12] on poly(propylene glycol) complexed with lithium and sodium salts suggested, this kind of measurement can provide valuable information, linking the structural relaxation of the polymer backbone, the free-ion concentration and the observed conductivity of the electrolyte.

Besides the important investigation of the Li^+ ion diffusion and conductivity, which is significant for the performance of the battery electrolytes, there are more general and fundamental problems that can be approached using this experimental technique. Among them are the relaxation properties of glass-forming liquids in general, the significance and the mechanism of the dynamic glass transition and the faster structural relaxations in such systems, the relation between mechanical and electrical relaxations, the coupling between different relaxation mechanisms, etc.

Although photon correlation spectroscopy (PCS) and Brillouin spectroscopy are both dynamic light-scattering techniques, they probe different physical phenomena at different timescales (Fig. 1.1). PCS spans a very broad dynamic range and can be used to study

processes such as the Brownian motion of particles in suspension and the diffusion of molecules in dilute polymer solutions or collective phenomena in concentrated polymer solutions and polymer melts. The accessible frequency range is typically from 10^{-3} to 10^{7} Hz, corresponding to characteristic times for the processes between hours to hundreds of nanoseconds. Naturally, the dynamics of the processes probed in this range are represented in time space. By using PCS, we were able to study in detail the collective diffusion of the polymer network formed by the polymer in its melted state. For example, the characteristic times for the collective diffusion in PEO (M_W=1050) were in the range from 0.1 to 1 seconds.

On the other hand, Fabry-Perot interferometry opens an additional dynamic range enabling observation of faster processes with characteristic times ranging from nanoseconds to picoseconds and corresponding frequencies between 10^{7} and 10^{12} Hz. In

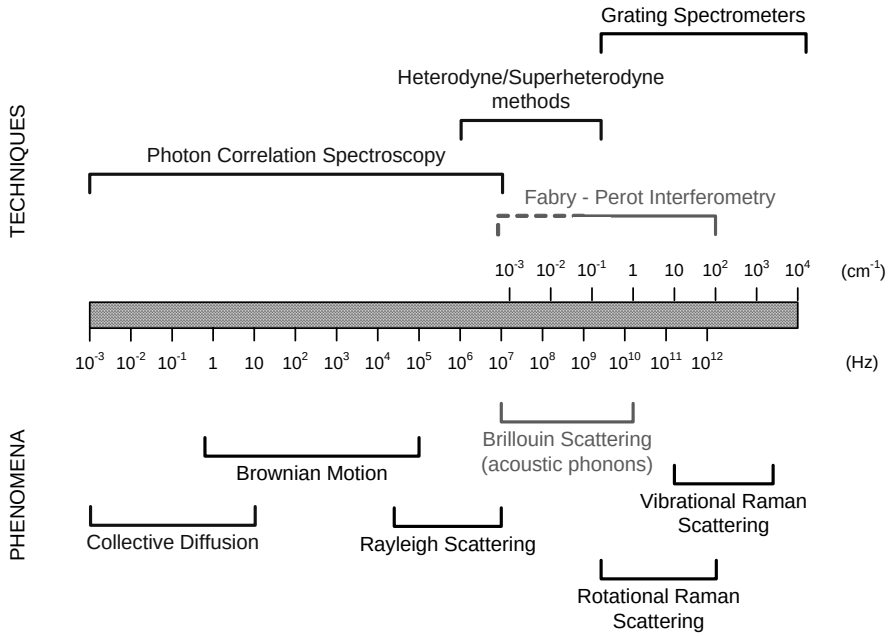

Fig. 1.1 – Laser spectroscopy

this sense, the two techniques are complementary, providing information about the dynamics of the system over a very broad time range. The natural representation for the F-P data is in frequency space.

Another very appealing light-scattering technique which emerged recently is based on heterodyne and superheterodyne detection methods.[13,14,15] It shows very good resolution in the frequency range between 10 MHz and 3 GHz and has the potential to complement the traditional Fabry-Perot interferometers for frequencies below 1 GHz, where they are very difficult to operate.

One of the characteristic and novel features of our light-scattering setup is the use of fiber-optic coupling of the scattered light into both the Fabry-Perot interferometer and the PCS setup allowing simultaneous or consecutive measurements with both techniques, conducted without changing the conditions or disturbing the sample. It presents an open system where other techniques (for example, superheterodyne detection and a grating spectrometer) can be easily incorporated. Therefore, it combines instruments in a single experimental setup allowing the study of a very broad dynamic range – some 15-17 orders of magnitude in frequency.

Since the late 1980s, significant effort has been put into incorporating fiber-optic detection into dynamic light scattering experiments. In his pioneering work,[16] Brown made an intriguing observation: he found that the collection efficiency of a single-mode fiber seemed to match or even surpass that of the classical two-pinhole detection optics in PCS experimental setups. Later, it was shown by Rička[17] both theoretically and experimentally, that in a PCS experiment with single-mode fiber detection, one can achieve the theoretical maximum for the coherence factor while maintaining high light-

collection efficiency. Recently, we implemented fiber-optic detection in both PCS and F-P measurements. The design features, performance and characteristics of the experimental setup along with some preliminary results are presented in earlier reports.[9,18] Both single-mode and multimode fiber coupling were considered, and the effects of the fiber core diameter and mode structure on the resolution of the Fabry-Perot interferometer were studied in detail. It was demonstrated that the fiber-coupled setup performs as well as or better than the classical (pinhole) interferometer. It is worth noting that among other advantages of the fiber-coupled Fabry-Perot interferometer, is the unique possibility of accessing a broad continuous range of scattering angles. It is this distinctive feature of the setup that allowed the first-of-a-kind q-dependent measurements of the Brillouin frequency and linewidth of the scattered light reported in the present study.

This dissertation is structured as follows: In the next chapter, we describe the fiber-optic approach in the experimental setup. After a brief description of the experimental components and the operation of the Fabry-Perot interferometer, special attention is devoted to the light collection and the alignment of the system, especially the proper alignment for the angle-dependent measurements, which is critical. The Rayleigh-Brillouin spectrum emerging from scattering from density fluctuations in the medium is considered in Chapter 3. We present some of the relevant viscoelastic theories and introduce the notion of the relaxation phenomena and discuss their effect on the observed spectra. Some of the necessary assumptions and simplifications are summarized. Next, the viscoelastic and dynamic quantities of interest are defined and their temperature dependence is considered. Chapter 4 focuses on the relaxation behavior in glass-forming

substances and more specifically in polymeric systems and the relation between relaxation processes, polymer chain mobility and charge transport properties in polymer electrolytes. The present study is placed in perspective with results from other experimental techniques such as mechanical and dielectric relaxation as well as neutron scattering available in the literature for PEO-Li^+ electrolytes. In Chapter 5, we describe some of the specifics of the experimental procedure, data collection and data reduction as well as the analysis of the experimental error bars. Chapter 6 presents the experimental results. Temperature dependence, concentration dependence and scattering wave-vector dependence are considered, followed by discussion. In conclusion, the findings and their implications are summarized in Chapter 7.

CHAPTER 2

EXPERIMENTAL SETUP

2.1. Experiment layout

The experimental setup designed, built and used in this work is schematically shown in Fig. 2.1. We use an argon-ion laser Innova-100 (*Coherent*, Palo Alto, California) operating in a single longitudinal and transverse mode at $\lambda = 514.5$ nm. The single mode operation is accomplished by using a solid Fabry-Perot etalon in the laser cavity. The power of the incident laser beam at the location of the sample was typically in the range 50–150mW depending on the sample. The laser output is vertically polarized and moderately focused at the center of the sample cell. The focusing lens is an achromatic doublet with focal length $f = 300$ mm and a beam size at the waist is $\sim 100 \mu$m.

Two sample-cell holders were used depending on the temperature range and the scattering geometry. The first one (Fig. 2.1-a) is referred to as the "high-temperature cell" and has a temperature range up to 150^{o}C, but allows for 90^{o} scattering angle only, and the second one (Fig. 2.1-b) is referred to as the "goniometer assembly" with a temperature range up to 80^{o}C and variable measurement angles. The high-temperature cell was custom designed and built in-house for this application. It is made of a well-isolated massive copper block intended to equilibrate the heat distribution. There are three electrical heaters, allowing for differential supply of heat at different locations on the

surface of the copper block. The heaters are controlled by a programmable proportional-integral (PI) controller receiving feedback from four platinum RTD detectors located at different locations inside the block. This design allowed compensation of any temperature gradients. The temperature range for the cell is between 30°C and 150°C with a set point accurate to about $\pm 0.5\,^{o}$C and long-term stability better than $\pm 0.05\,^{o}$C. There are four optical ports at 90° in the copper cell – two for the incident laser beam and two for detection. The light scattered by the sample is passed through a polarizer and coupled into the single-mode detection fiber by an aspheric lens with $f = 15.3$ mm focal length (*Thor Labs Inc.*, Newton, New Jersey).

The goniometer assembly along with the sample holder, index matching vat and

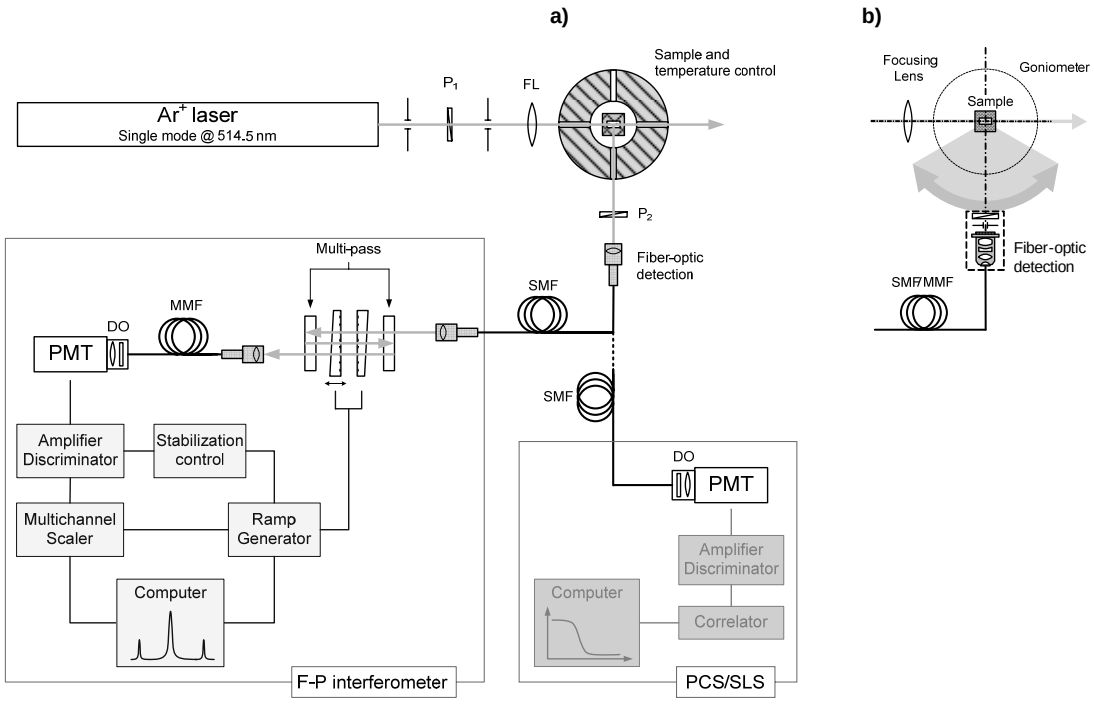

Fig. 2.1 – Fiber-optic setup: a) high-temperature cell; b) goniometer assembly

temperature control are part of a standard light-scattering setup for photon correlation spectroscopy and static light scattering (PCS/SLS) model BI-200SM from *Brookhaven Instruments Corp.* (Holtsville, New York). As an index matching liquid we use toluene in a temperature controlled vat. The temperature is set in the range between 30°C and 80°C and is controlled and monitored to ±0.5 °C. The angle of the goniometer arm is adjusted by a stepper-motor or manually in the range of angles between 0° and 160° (only the range from 20° to 160° was used). The angle was set with ±0.05° accuracy. To couple the scattered light into the receiver end of the fiber we use a 20x magnification microscope objective and compact five-axis spatial filter assembly both from *Newport Corp.* (Irvine, California), modified to accommodate standard fiber connectors in place of its pinhole. The spatial filter assembly is mounted on the goniometer arm and it provides sufficient degrees of freedom for precise alignment. The entire assembly is rather robust against misalignment. The optimal magnification for the microscope objective is determined by the best possible match with the numerical aperture of the fiber and the desired dimensions of the scattering volume in the sample. There is a variety of other coupling solutions for use with optical fibers such as the aspheric lens mentioned above. For polarization dependent measurements, a polarizer is used in front of the optical assembly. It is essential to resolve the polarization of the scattered light before it is coupled into the fiber since a standard optical fiber scrambles the polarization dependent information in the signal.

A single-mode fiber and a small-diameter multimode fiber are used in different measurements reported here. The limitations in the implementation of multimode fibers with the present experimental setup were outlined elsewhere.[9,18] Both fibers are supplied

as 5-meter FC-connectorized cables from *Thor Labs Inc* with fibers from *Nufern* (East Granby, Connecticut). The single-mode fiber used has nominal parameters as follows: cut-off wavelength 430 nm, mode field diameter (MFD; $1/e^2$ – near field) of 3.5 μm, and numerical aperture $NA = 0.13$. The multimode fiber has nominal parameters: cut-off wavelength 1350 nm, mode field diameter of 9.5 μm (at 1060 nm), and $NA = 0.13$.

As shown in Fig. 2.1, once the scattered light is coupled into the receiving fiber, it can be directed to either of the two instruments, the PCS/SLS or the Fabry-Perot interferometer, and then detected, analyzed and stored by the appropriate electronic equipment. The details of the PCS/SLS system will not be discussed here, since in the present study only Brillouin scattering results, obtained with the Fabry-Perot interferometer are reported. A plane-parallel Fabry-Perot interferometer from *Burleigh Instruments* (now *EXFO Burleigh Products Group Inc.*, Victor, New York) in a triple-pass configuration was used. The operation and characteristics of the interferometer will be described in detail in Section 2.2. The input collimation and the output collection on both sides of the F-P interferometer are performed by aspheric lenses in fiber-optic collimator assemblies, connectorized with FC and SMA standard connectors, respectively. The output fiber with 600 μm core diameter (multimode) is from *Thor Labs Inc.* and its purpose is to direct the light to the photomultiplier tube (PMT). The PMT optics consisted of a laser band-pass filter (10 nm) for 514.5 nm wavelength and an aspheric imaging lens.

2.2. The Fabry-Perot interferometer

The classical plane-parallel Fabry-Perot interferometer is schematically shown in Fig. 2.2(a). The sample is illuminated by a laser beam in a typical light scattering geometry. Single-mode operation of the laser is essential and it is usually achieved by introducing an etalon inside the laser resonator. The scattered light from the sample is collimated by the first lens, L_1, and then passed through the two parallel Fabry-Perot mirror plates with adjustable spacing, d. For simplicity, we assume a refractive index $n=1$ (air filled mirror spacing), normal incidence and negligible absorption. The second lens, L_2, collects the light and the output signal is detected through a pinhole with diameter a_2

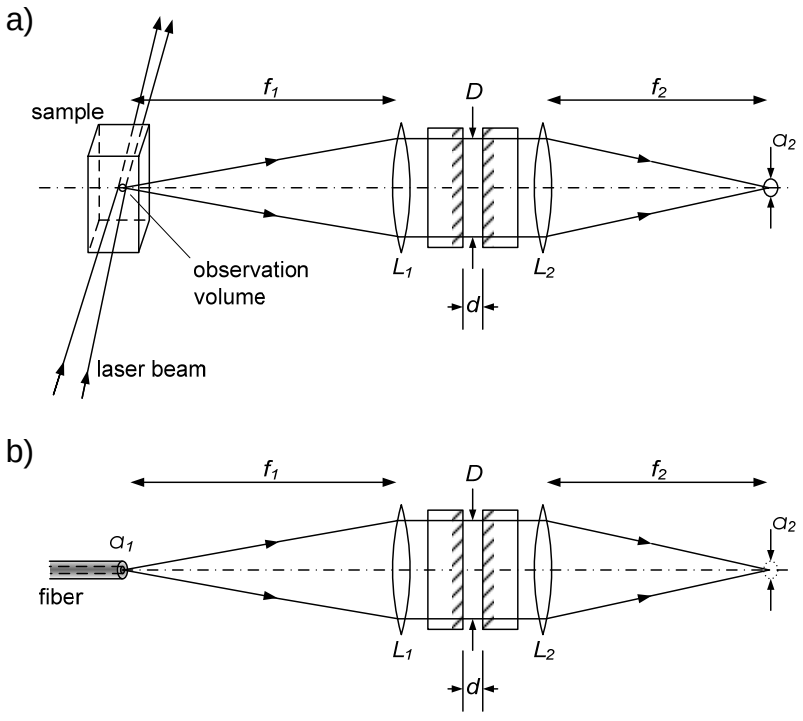

Fig. 2.2 – a) Classic (pinhole) and b) fiber-coupled plane-parallel F-P interferometer. Collimating lens L_1 with focal length f_1; detector lens L_2 with focal length f_2; D – mirror aperture; d - adjustable mirror spacing

which selects only rays incident on the Fabry-Perot within a narrow angular range. The diameter of the pre-image of the pinhole a_2 and the size of the illuminating laser beam determine the scattering volume in the sample. When an optical fiber delivers the signal to the input of the interferometer [Fig. 2.2(b)], the only difference is that the angular selection is performed with the fiber core of diameter a_1 serving as the limiting aperture.

The theory of operation and the transfer function of the F-P interferometer are considered in many textbooks[19,20,21] and apart from a brief description will not be repeated here. The transmittance function under the above simplifying assumptions is periodic with maxima occurring when an interference condition is fulfilled (Fig. 2.3).

The reflected and transmitted light intensities are given by:

$$\frac{I_r}{I_i} = \frac{Q_R \sin^2 \frac{\delta}{2}}{1 + Q_R \sin^2 \frac{\delta}{2}} \tag{2.1}$$

$$\frac{I_t}{I_i} = \frac{1}{1 + Q_R \sin^2 \frac{\delta}{2}} \tag{2.2}$$

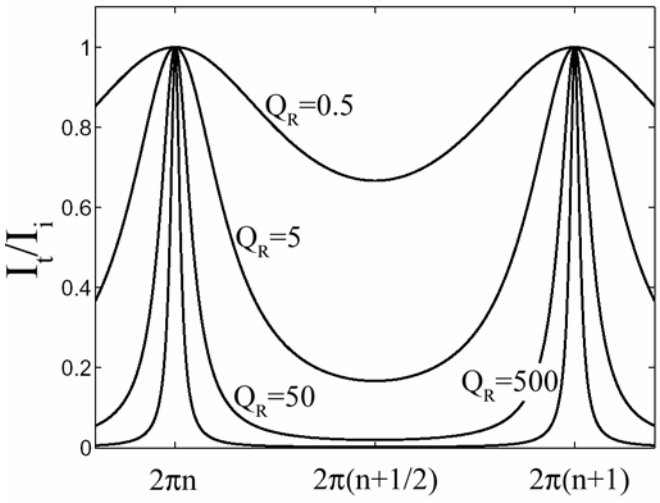

Fig. 2.3 – Transmittance function I_t / I_i of a plane-parallel Fabry-Perot interferometer for different reflectivities R of 0.1, 0.42, 0.75, 0.91 (quality factors 0.5, 5, 50, and 500, respectively).

where I_i, I_r and I_t are the incident, reflected and transmitted intensities, respectively,

$$\frac{\delta}{2} = \frac{2\pi d}{\lambda}\cos\varphi \tag{2.3}$$

with λ the laser wavelength and φ the incidence angle from the normal to the surface. For normal incidence, $\cos\varphi = 1$. The quality factor for the reflectivity Q_R is often denoted as the finesse coefficient (or coefficient of finesse):

$$Q_R = \frac{4R}{(1-R)^2} \tag{2.4}$$

with R the reflectance (defined for light intensity) of the F-P mirror plates. The transmittance without absorption is therefore $T = 1 - R$. In the general case, where the absorption, A is not negligible, $R + T + A = 1$ and the transmitted intensity is reduced by the factor t called the transmission factor

$$t = \left(1 - \frac{A}{1-R}\right)^2 . \tag{2.5}$$

A plot of the transmittance function for maximum transmission, $t = 1$, and for different values of Q_R (different reflectivity) is shown in Fig. 2.3. Two adjacent interference orders are separated by a frequency interval called the free spectral range (FSR, measured in Hz)

$$\Delta\nu_{FSR} = \frac{c}{2d}, \tag{2.6}$$

where c is the speed of light in vacuum. Two properties are characteristic for the transmission function: the full-width at half maximum (FWHM), $\Delta\nu_{FWHM}$ and the suppression of light between the maxima, measured by the contrast, $C=I_{max}/I_{min}$

$$C = \frac{(1+R)^2}{(1-R)^2}. \tag{2.7}$$

The ratio of the peak separation to the FWHM width of a peak defines the finesse of the instrument

$$F = \frac{\Delta\nu_{FSR}}{\Delta\nu_{FWHM}}. \tag{2.8}$$

In the ideal case considered so far, assuming no absorption, perfect flatness of the two reflecting surfaces and perfectly collimated illumination beam, corresponding to infinitely small aperture a_1 and ideal lens system, the finesse depends only on the reflectivity. It is often referred to as the reflectivity finesse

$$F_R = \frac{\pi\sqrt{R}}{1-R}. \tag{2.9}$$

In a real instrument, one has to consider the effects of imperfect reflecting surfaces, finite aperture size, monochromatic aberrations of the collimating optics, etc. All these imperfections lower the finesse and the instrument's resolution. The total or effective finesse is given by

$$\frac{1}{F_{eff}^2} = \frac{1}{F_R^2} + \frac{1}{F_M^2} + \frac{1}{F_A^2} + \ldots \tag{2.10}$$

The two most significant corrections are given by the flatness finesse

$$F_M = \frac{M}{2}, \tag{2.11}$$

with M being the flatness figure for the mirror's surface with root-mean-square (rms) flatness λ/M, and the aperture (pinhole) finesse

$$F_A = \frac{\lambda}{d}\frac{4f_1^2}{a_1^2}, \tag{2.12}$$

with f_1 being the focal length of the collimator (Fig. 2.2). The combination of the reflectivity and flatness finesse, $F_{RM} = \left(F_R^{-2} + F_M^{-2}\right)^{-1/2}$ is a fixed parameter for a given mirror set and in the case of a small fiber diameter determines the width and shape of the transmission function. The degree of collimation depends on the angular size of the fiber aperture as seen by the collimator (see also the inset in Fig. 2.4)

$$\theta_1 = \frac{a_1}{2 f_1}. \tag{2.13}$$

The angular size of the aperture a_1 can be decreased by increasing the focal length f_1 of the collimator until the beam diameter fills the entire useful aperture, D of the

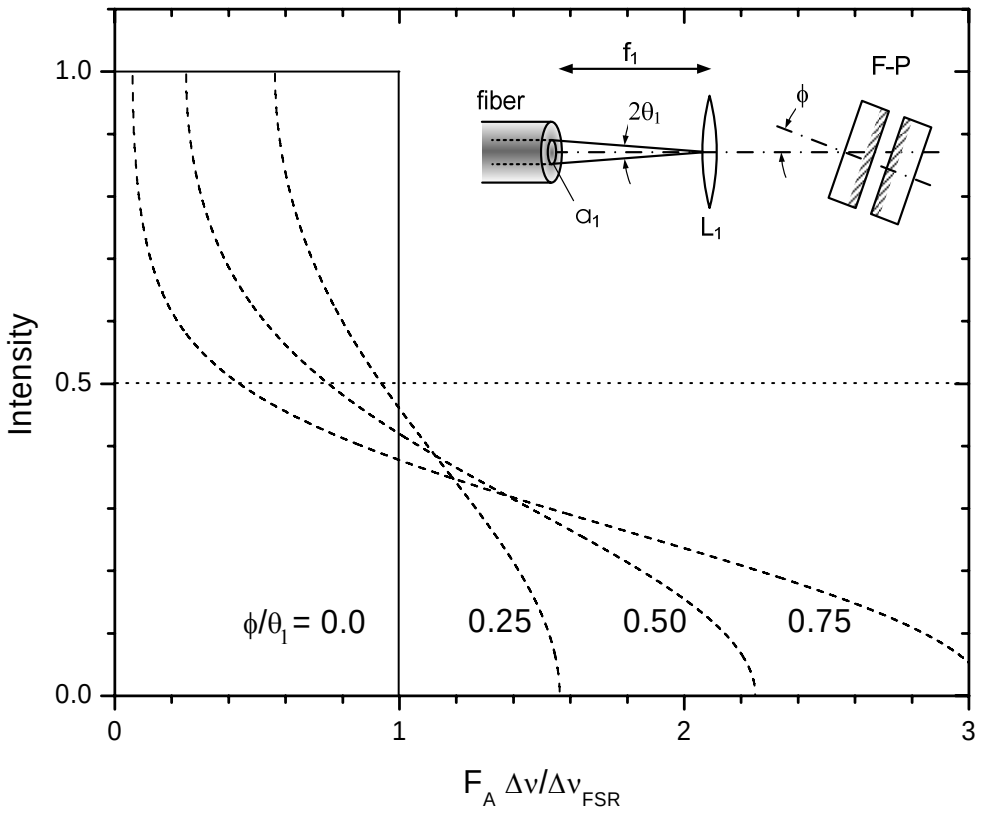

Fig. 2.4 – Misalignment effect. ϕ – misalignment angle between collimator axis and F-P axis; θ_1 – angular size of the fiber aperture (see text).

interferometer. When θ_1 approaches $\sqrt{\lambda / F_{RM} d}$, the beam through the interferometer is not sufficiently collimated, F_A becomes comparable to F_{RM}, and the effective finesse is reduced according to Eq. (2.10).

If F_A is much lower than F_{RM}, the transmission is dominated by the fiber aperture and it is strongly dependent on the mutual alignment between the collimator axis and the interferometer axis. In the limit $F_A \gg F_{RM}$ and perfect alignment, the transmission peak will have the rectangular shape shown by the solid line in Fig. 2.4. However, if the two axes are misaligned by angle ϕ, the lineshape will be deformed as shown by the dashed curves in Fig. 2.4 for several values of the misalignment parameter ϕ / θ_1. The maximum transmission remains the same but the width at half-maximum decreases. Since the peaks have a long tail and are highly asymmetric, this regime is very unsuitable for spectroscopic applications. It can occur when high reflectivity mirrors and large multimode fiber diameters are combined.[18] The single-mode and the small-diameter multimode fibers used in the present study essentially behave as a point source illumination of the Fabry-Perot interferometer. Therefore a diffraction limited collimation can be achieved and the finesse of the instrument is not reduced considerably from its reflectivity-flatness value.

Fabry-Perot interferometers in multipass configuration[22,23] offer high contrast and are well suited to study the spectra from samples such as polymers where the central Rayleigh peak is very strong. In general, more passes give higher contrast but lower throughput. The triple-pass systems are usually the primary choice but five-pass systems are also in use.[20] For the present application, a triple-pass system gives the optimal combination of high contrast and reasonably good transmission.

In multipass operation, the transmission function is obtained from the single-pass function [Eq. (2.2)] raised to the *n*-th power where *n* is the number of passes.[20] This leads to theoretical expressions for the resulting contrast, finesse and transmission:

$$C_n = (C_1)^n , \tag{2.14}$$

$$F_n = F_1 \frac{1}{\sqrt{2^{1/n} - 1}} , \tag{2.15}$$

$$t_n = (t_1)^n , \tag{2.16}$$

where C_1, F_1 and t_1 are the contrast, finesse and transmission for single pass obtained through Eqs. (2.7), (2.9) and (2.5), respectively. The factor $\left(2^{1/n} - 1\right)^{-1/2}$ in the expression for the finesse for triple pass is ~ 1.961. In the real interferometer, due to various imperfections, the observed values are lower than the theoretically predicted. For example, for the set of mirror plates used in our interferometer the measured reflectivity, transmission and absorption are $R \approx 94\%$, $T \approx 5\%$ and $A \approx 1\%$, and the following values are typically observed

	single-pass	triple-pass
finesse, *F*	~ 50	~ 80
contrast, *C*	~ 10^3	~ $10^7 - 10^8$
transmission factor, *t*	~ 60%	~ 15% – 20%

The shape of the instrumental profile changes from a Lorentzian form, *L*, in the case of single-pass configuration to a Lorentzian-cubed, L^3. The instrumental profiles *L* and L^3 are calculated for the set of mirrors discussed above and are compared in Fig. 2.5(a). In Fig. 2.5(b), the experimentally obtained instrumental function in triple-pass configuration

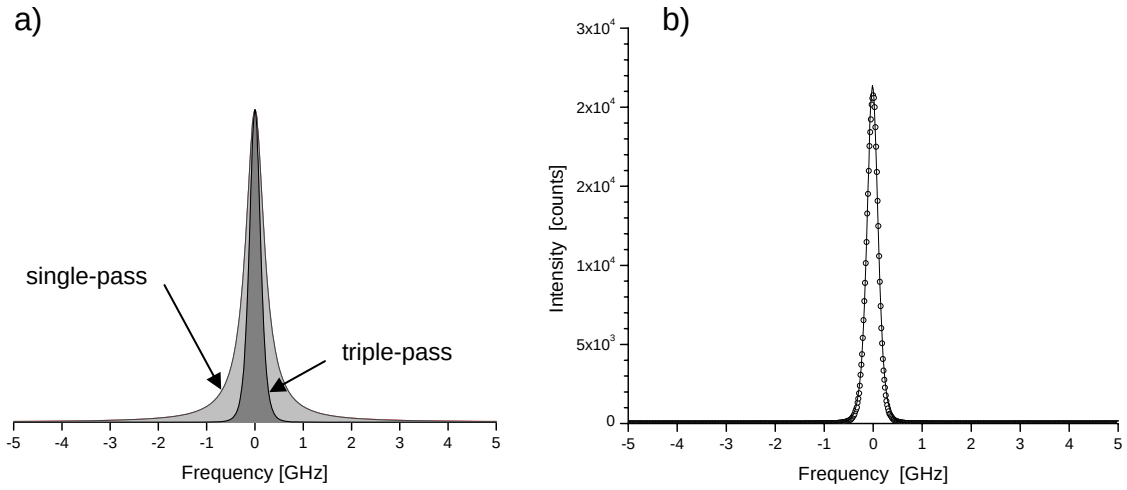

Fig. 2.5 – a) single-pass vs. triple-pass instrumental profile; b) measured triple-pass instrumental function (data points) and L^3 fit (solid line)

(points) and the best fit with L^3 function (solid line) are shown. As is evident in the figures, the triple-pass instrumental function is narrowed and the tail of the profile is greatly reduced to result in the high contrast. The latter feature is of great importance for studying polymer spectra since in such systems the weak Brillouin features in the spectrum will be completely obscured by the long tails of the very strong Rayleigh peak if a single-pass interferometer is used.

The determination of the exact form and especially the width of the instrumental function is very important since they are used in the deconvolution of the "true" Rayleigh-Brillouin spectrum from the experimentally observed spectrum and will be discussed in detail in Sec. 5.2.

2.3. Light collection: scattering geometry and alignment

In a well-aligned system the excitation (laser) beam and the receiver (fiber) beam intersect at the center of rotation of the goniometer and lie in one plane at all angles of the

goniometer arm (Fig. 2.6). Both beams are well approximated as Gaussian beams with wave vectors $\mathbf{k}_e$ and $\mathbf{k}_s$ inside the scattering volume. An angle θ between the excitation and the observation beam determines the scattering vector $\mathbf{q} = \mathbf{k}_s - \mathbf{k}_e$ with magnitude

$$q = \frac{4\pi n}{\lambda} \sin\frac{\theta}{2}. \tag{2.17}$$

The geometry described can be easily visualized by coupling part of the laser beam into the back end of the receiving fiber. The two beams are clearly visible in the index matching liquid which greatly assists the initial alignment.

The choice of the optimal beam parameters is considered in detail by Rička *et al*.[17,24] Here, we briefly summarize their conclusions. In the case of perfect alignment and the Gaussian beam approximation, the average signal at the detector is inversely proportional to the radius of the excitation beam, ω_e, and it is independent of the radius of the

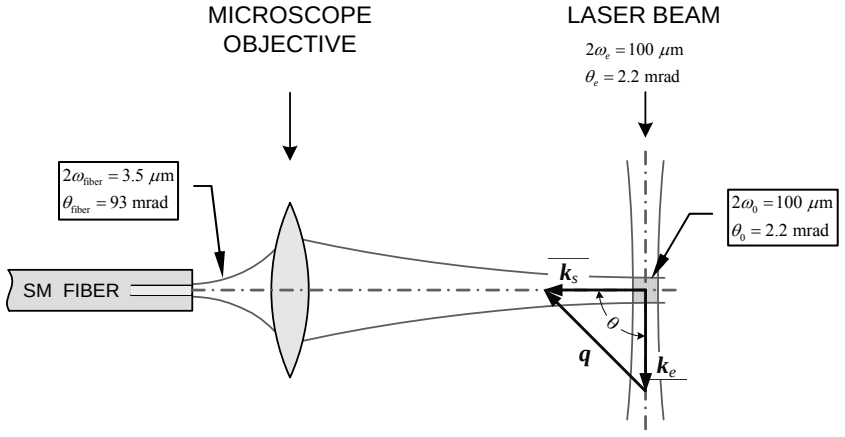

Fig. 2.6 – Single-mode fiber detection. The half-angle divergence of the excitation and observation beams in the toluene sample, θ_e and θ_o, were calculated using the expression $\theta_x = \tan^{-1}(\lambda / n\pi\omega_x)$, with $\lambda = 514.5$ nm and refractive index $n = 1.5$. The beam divergence of the fiber mode in air, $\theta_{\text{fiber}} = 0.093$ rad, is less than the nominal numerical aperture of the fiber, NA = 0.13

observation beam, ω_o [see Eq. (26) in Ref. 17]. Therefore, the light-collection efficiency increases linearly with decreasing excitation beam diameter. In practice, the focusing of the laser beam is limited by the power density in the sample which leads to thermal effects. On the other hand, the observation beam can be expanded without sacrificing light-collection efficiency – by increasing the observation beam diameter, the number of observed scatterers increases quadratically, but the signal collected from each scatterer decreases correspondingly since the solid angle of the light-collection decreases. Working with a larger receiver beam diameter makes the setup less sensitive to misalignment and since the collection solid angle is smaller, the uncertainty in the scattering vector, $\mathbf{q}$, is reduced.

It was demonstrated[16,17,24,25] that good alignment and adequate light-collection efficiency in both photon correlation spectroscopy and static light scattering can be achieved by using graded index (GRIN) lenses and a receiver beam slightly focused or collimated with a beam diameter at the location of the sample in the range from 0.3 to 1 mm. As discussed in Ref. 18 and shown in Fig. 2.1, our setup uses a microscope objective or an aspheric lens to couple the scattered light into the single-mode or the multimode fiber. Both the laser and receiver beams are focused to an equal spot size about 100 μm in diameter. Even with such small beam diameters, the alignment at any fixed scattering angle is very easy. Initially, a fraction of the laser beam is coupled in the backward direction in the fiber. The beam emerging from the receiver end (which is visible in the index matching liquid) is then intersected with the excitation beam at the center of the index matching vat. Subsequently, the receiving fiber is connected to the PMT and fine adjustment is performed by maximizing the signal (we simply used the

light scattered by the toluene in the vat) while the fiber beam is translated vertically across the excitation beam profile.

Proper alignment at all scattering angles is more difficult, but not impossible. Here, we describe one possible alignment procedure which gives quick alignment as well as a quantitative measure of the error in the observation angle. Initially, the index matching vat filled with toluene is centered as well as possible with respect to the center of rotation of the goniometer and the incoming laser beam. This step is important since both the observation and the excitation laser beams are refracted by the cylindrical wall of the vat. The vat is aligned at the center of rotation by using the reflections of both beams from its surfaces. By rotating the goniometer, the beam emerging from the fiber end is directed into the vat at various incoming angles between 20^o and 160^o. The laser beam always enters the vat at 180^o where the vat has by design a flat optical input window. Both the cylindrical shape and the surface quality of the vat should be very good. In fact, for this measurement it was necessary to hand-select among several vats one with good cylindrical shape. As scattering cells containing the samples, we use standard round NMR tubes (O.D. = 5 mm, *Wilmad-Labglass*, Buena, New Jersey). For alignment, we use a separate identical NMR tube, partially filled with toluene. The sample and the alignment NMR tubes can be easily substituted in the sample cell holder, which was designed to retain the exact position of the cylindrical cell with respect to the beams and the axis of the goniometer. In order to get the highest visibility (brightness) of the features described below, the level of toluene in the NMR cell should slightly exceed the toluene level in the vat.

If the center of the NMR cell is observed from above, the area where the two beams intersect looks similar to that shown in the snapshots in Fig. 2.7. In these snapshots the laser beam is always vertical and enters the cell from 180°. The angles corresponding to the goniometer scale are also shown in one of the panels. The straight lines correspond to the two beams (laser and fiber). The ring is an image of the beams after reflection at the cylindrical wall of the NMR cell. It is strongly affected by refraction as the light passes the top free toluene surface, which has a meniscus shape due to the strong wetting effect near the glass wall. The fact that the beams are observed through this refracting meniscus and the strong curvature of the NMR wall makes the feature very sensitive to even slight misalignments. Indeed, if the incoming beams do not enter the cell at direction exactly

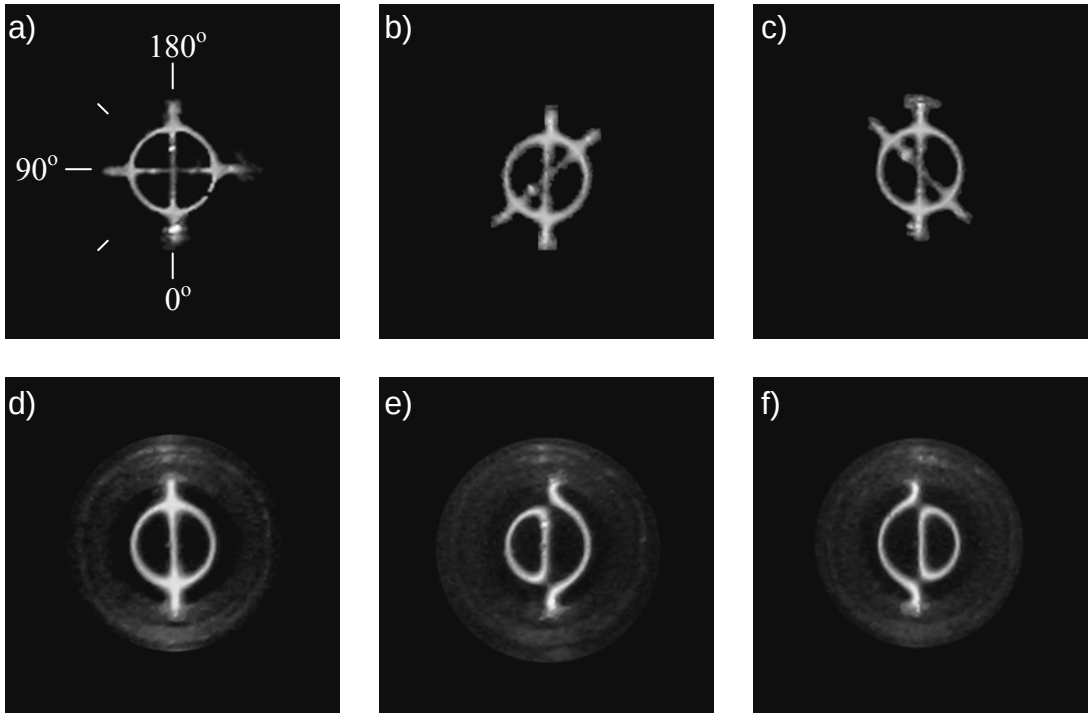

Fig. 2.7 – Alignment procedure using a round 5-mm NMR tube filled with toluene. The laser beam is vertical from top to bottom in all panels and the fiber beam is from left to right in the top three panels.

normal to the cylindrical wall, they are distorted and both the beams and the ring appear significantly deformed. The snapshots in the top line show both beams visible with the fiber beam pointing at (a) 90^o, (b) 45^o, and (c) 135^o. In these cases the cell is well aligned with the axis of rotation. In the bottom row, only the laser beam is visible and the fiber beam is blocked for clarity. In panel (d), the cell is very well aligned against the beam which is evident from the symmetry on both sides of the beam. In panels (e) and (f), the cell is slightly misaligned to the left and to the right, respectively. In the shown examples, the center of the cell was displaced perpendicular to the beam by about 200μm which is about two beam diameters. In fact, the diagnostic of the method is much more sensitive since a visible deformation of the symmetry is detectable even at displacements as small as 50 μm or less. When the fiber beam is used instead of the laser beam, the cylindrical cell is aligned simultaneously at all angles between 0^o and 180^o (limited to 160^o in our experimental layout) by rotating the goniometer while continuously monitoring the pattern. The system is aligned when the regularity in the shape of the pattern is preserved at all angles [examples are shown at three angles in panels (a) – (c)]. This ensures that the laser beam and the observation beam intersect at the center of rotation for all angles of the goniometer. It should be noted that slight deviations might always be present due to the imperfections of the glass surfaces of both the index-matching vat and the NMR cell, but they are kept small by selecting good quality components.

The reasoning above allows for the estimation of an upper limit for the error in the scattering angle at the location of the scattering volume. For example, in our setup from simple geometry arguments a misalignment of the rotation axis by ±50 μm translates to ±0.3 mrad or about $\pm 0.015^o$ error in the scattering angle. Other factors, such as replacing

the alignment NMR cell with the NMR tubes containing the samples as well as replacing the fiber at the detection optic assembly, also affect the alignment and the overall uncertainty after various tries was estimated to better than $\pm 0.05^{o}$.

To test the alignment at different scattering angles we used the following standard procedure: the scattering intensity from toluene, $I(\theta)$ was recorded as a function of the scattering angle, θ. Since toluene is a Rayleigh scatterer, the quantity $I(\theta)\sin(\theta)$, which represents the intensity corrected for the scattering volume, should be independent of scattering angle. As we tested the alignment between 20^{o} and 160^{o} in 5^{o} increments, the quantity $I(\theta)\sin(\theta)$ at each measured angle was averaged over 20 runs each with 1 second duration and corrected for dark count and dead time of the PMT. The output of the alignment procedure is shown in Fig. 2.8. It demonstrates that the quantity $I(\theta)\sin(\theta)$ is constant to within $\pm\ 2.0\%$. It should be noted that the alignment with larger beam diameters or even slightly defocused receiver beams (which in effect lowers the angular resolution of the receiver) is much easier to achieve.[26] For example, Suparno *et al.*[25] demonstrated $I(\theta)\sin(\theta)$ constant to within $\pm\ 3\%$ for scattering angles in the range from 15^{o} to 160^{o} using a GRIN lens and collimated receiver beam with a diameter of 800 μm.

In the case of the Fabry-Perot interferometer, the ability to perform detection easily at various scattering angles and therefore the ability to vary the scattering wavevector $\mathbf{q}$, presents a substantial improvement over the conventional pinhole setup. Historically, angle-dependent measurements with F-P interferometers were performed very rarely. The size and weight of the interferometer makes it practically impossible for it to be repositioned at different angles with respect to the excitation laser beam. On rare

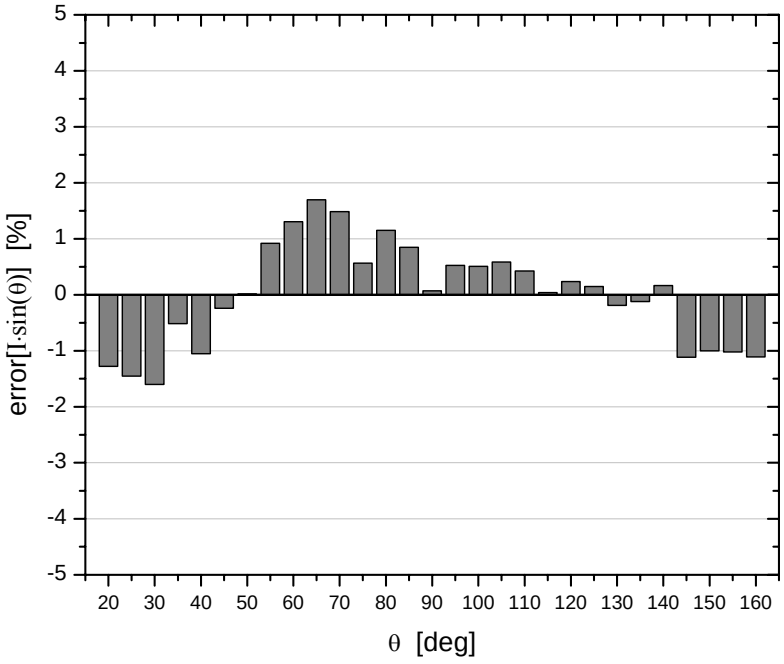

Fig. 2.8 – Alignment test for scattering angles between 20^o and 160^o

occasions, sophisticated optical designs were employed that allowed the axis of the laser beam to be rotated with respect to the stationary axis of the interferometer.[27] These methods are difficult to implement and align and have had only limited application. Due to the lack of a convenient multi-angle setup, the vast majority of experiments published in the literature are limited to 90^o scattering angle. By contrast, the fiber-optic approach facilitates convenient access to a broad continuous range of scattering angles. As we will show in Chapters 5 and 6, we are routinely collecting data in the range between 20^o and 160^o in 5^o increments, and this entire range of angles can be covered in a single day of measurements.

CHAPTER 3

THEORY AND BACKGROUND

3.1. Viscoelasticity of liquids and the light-scattering spectra

Spontaneous microscopic fluctuations always occur in a system at finite temperature. They are dissipated in the medium the same way external disturbances are – through diffusion, viscous flow and thermal conduction. By observing such fluctuations one can study transport properties in the system at thermodynamic equilibrium and obtain basic information about the dynamics of the fluid. Thermal fluctuations occur naturally with a distribution of wavelengths and frequencies. For long-wavelengths and low-frequency fluctuations, the fluid behaves like a continuum and the response can be described by the equations of hydrodynamics. In such a case, the space and time variations are slow on the scales of molecular processes, collision mean free path, and inverse collision frequency. When the condition of slow variations is not fully satisfied, the fluid behavior is expected to deviate from the predictions of hydrodynamic calculations. The transition is smooth and it is appropriate to extend the hydrodynamic description by retaining the basic structure of the equations, but replacing the thermodynamic derivatives and transport coefficients with functions which can vary in space and time. This resulting theory is called generalized hydrodynamics and provides a description of the fluid dynamics over a wider range of spatial and temporal variations.[28] At wavelengths comparable to the

intermolecular distances, the local (molecular) structure of the fluid becomes important. Then the continuum picture is no longer valid and the system must be described as an assembly of interacting particles in the framework of molecular dynamics. In a light scattering experiment, the wavelengths probed, Λ, are on the order of the wavelength of the visible light

$$\Lambda = \frac{2\pi}{q} = \frac{\lambda}{2n\sin(\theta/2)}, \tag{3.1}$$

therefore, the hydrodynamic limit applies and generalized hydrodynamic theory provides a good description. The wavelength, Λ, associated with the momentum transfer, specifies the wavelength of the density fluctuation being measured, λ is the laser wavelength and θ is the scattering angle.

On a microscopic level, the relaxation dynamics in the liquid are understood as coupling of the fluctuations to some internal or external degrees of freedom. If some degree of freedom is relaxing with a relaxation time comparable to the inverse frequency of the fluctuation, this is observed in the resulting spectrum as a relaxation feature. The details of the microscopic description continue to pose an extraordinarily difficult problem in experimental and theoretical chemical physics due to the large number of degrees of freedom which in most cases are not independent but rather are strongly interacting.

On a macroscopic level, the structural properties of a viscoelastic liquid can be characterized by its time-dependent response to applied pressure or shear stress. Thermal fluctuations in the liquid occur spontaneously and continuously. Local perturbations, which result from these fluctuations, disturb the equilibrium state of the liquid. Each degree of freedom (mode) of the system returns to its equilibrium value through a

relaxation process. The modes for which the relaxation is slow compared to the molecular interaction time are the collective modes. These diffusive processes involve a large number of particles and their relaxation time is proportional to the square of their characteristic wavelength which is large compared to the intermolecular distances.

In a simple, monatomic fluid there are three longitudinal and two transverse hydrodynamic modes (see Ch.5 in Ref. 28). The transverse modes are purely diffusive shear modes. One longitudinal mode is a purely diffusive heat-diffusion mode, which results from entropy fluctuations at constant pressure. The remaining two longitudinal modes are propagating acoustic modes (sound waves). They arise from pressure fluctuations at constant entropy and propagate with the adiabatic sound velocity, v_s, and have a lifetime $(\Gamma q^2)^{-1}$ where Γ is the classical acoustic attenuation coefficient. The two transverse (shear) modes are completely decoupled from the longitudinal modes. The thermal diffusivity mode is weakly coupled to the two acoustic modes, which in many cases can be neglected. In a light-scattering experiment, the incident light is scattered by density fluctuations in the fluid, which originate from the hydrodynamic modes. The isotropic spectrum results from the scattering from the three longitudinal hydrodynamic modes (Fig. 3.1). The central (Rayleigh) peak corresponds to the thermal diffusivity mode. The two spectral lines shifted in frequency by $\pm v_s q$ are the Stokes and anti-Stokes components of the Brillouin-Mandelstam doublet. The spectrum is described by a simple Lorentzian for the Rayleigh peak and the spectrum for a damped harmonic oscillator for the Brillouin peaks

$$I(\omega) = \frac{I_0}{\omega} \mathrm{Im}[(\omega^2 - \omega_B^2 - i\omega\Gamma_B)^{-1}], \tag{3.2}$$

or

$$I(\omega) = I_0 \frac{\Gamma_B}{(\omega^2 - \omega_B^2)^2 + (\omega\Gamma_B)^2}, \tag{3.3}$$

where ω_B and Γ_B are the Brillouin frequency and linewidth, respectively, and I_0 is a constant amplitude. The detailed shape of the Rayleigh-Brillouin spectrum from a simple monatomic fluid is considered in the literature.[29,30]

In molecular liquids, energy transfer may occur between internal degrees of freedom and the translational degrees of freedom, in which case there will be coupling between a mode characteristic of intramolecular motions and the collective modes describing density fluctuations which are responsible for the light-scattering spectrum. Such a coupling becomes important when the energy fluctuations in the internal degrees of freedom relax on a time scale comparable to the hydrodynamic characteristic times.

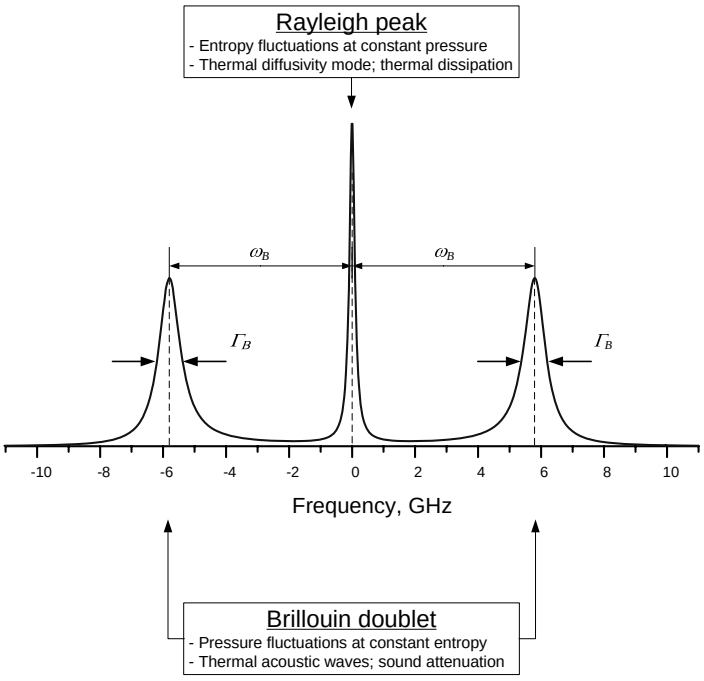

Fig. 3.1 – Rayleigh-Brillouin spectrum

When energy transfer takes place between translational motion and molecular internal degrees of freedom, the process is known as thermal relaxation. Section 3.2 summarizes the results of a theory that considers a thermal relaxation process with (i) weak coupling between intramolecular and translational degrees of freedom, and (ii) assumes a single relaxation time process for the decay of the energy in the internal modes.

Another type of relaxation process, known as structural relaxation,[31] is typical of highly viscous fluids such as associated liquids like glycerol as well as in polymer melts, and it strongly temperature-dependent. It appears as a slow response of the system to readjust structurally to local changes in density and temperature. Usually it is treated phenomenologically by introducing a frequency-dependent longitudinal viscosity (or equivalently, frequency-dependent longitudinal modulus) following the case of the thermal relaxation. The light-scattering spectrum of a structurally relaxing fluid will thus exhibit features that are qualitatively similar to those of a thermally relaxing fluid. In this case, the central Mountain peak (see below) is interpreted as associated with the structural relaxation mode.

For optically anisotropic molecules, the isotropic spectrum is not separated from the anisotropic spectrum. In general, the isotropic spectrum is determined by longitudinal fluctuations, although orientational dynamics can also have a contribution through rotation-translation coupling. The anisotropic spectrum results from shear and orientational dynamics as well as collision-induced scattering. Experimentally, the spectra are collected using different polarization geometries. If the recorded spectrum is obtained when both the incident and the detected light are vertically polarized, it is denoted as the vertical-vertical (VV) or polarized spectrum. In the case when the incident

and the scattered light have mutually perpendicular polarizations (for example, vertical-horizontal, VH), it is referred to as depolarized scattering.

The VV spectrum results from a combination of both isotropic and anisotropic scattering components. For example, at 90^o scattering angle

$$I_{VV}(\mathbf{q},\omega) = I_{iso}(\mathbf{q},\omega) + \frac{4}{3} I_{ani}(\mathbf{q},\omega), \tag{3.4}$$

where the isotropic component, $I_{iso}(\mathbf{q},\omega)$ can be written as

$$I_{iso}(\mathbf{q},\omega) = I_{iso} S(\mathbf{q},\omega), \tag{3.5}$$

where I_{iso} is the integrated intensity and $S(\mathbf{q},\omega)$ is the dynamic structure factor. The anisotropic component, $I_{ani}(\mathbf{q},\omega)$ can be directly measured by depolarized scattering since

$$I_{VH}(\mathbf{q},\omega) = I_{ani}(\mathbf{q},\omega). \tag{3.6}$$

To obtain the $I_{iso}(\mathbf{q},\omega)$ from VV measurements, the anisotropic component is either subtracted[32, 33] or, if it is very weak and broad, it is regarded as a small contribution to the background or simply ignored.

3.2. Generalized hydrodynamics (Mountain's theory)

The polarized Rayleigh-Brillouin spectrum of a liquid was analyzed by Mountain.[34,35] He developed an expression for the frequency distribution of the isotropic light scattered by a liquid with internal (vibrational) molecular degrees of freedom, which are weakly coupled to the translational modes. He further assumed that the energy transfer between internal degrees of freedom and translational modes is described by a single relaxation time, τ. This approach is equivalent to the Maxwell theory of

viscoelasticity and the model is known as the Maxwell-Debye model. The frequency dependent bulk viscosity can be written as

$$\eta_V(\omega) = \eta_V + \frac{b_1/\rho}{1+i\omega\tau}, \tag{3.7}$$

where η_V is the frequency-independent part of the bulk viscosity, ρ is the mass density, and b_1 is given by

$$b_1 = \frac{(C_p - C_V)C_i}{(C_V - C_i)C_p} v_0^2 \tau = (v_\infty^2 - v_0^2)\tau, \tag{3.8}$$

where, C_p and C_V are the heat capacities at constant pressure and volume, respectively, C_i is the vibration (internal) heat capacity, and v_0 and v_∞ are the sound velocities at low and high frequencies corresponding to the relaxed and non-relaxed values, respectively. The equations are reduced to the classical hydrodynamic spectrum when there is no sound dispersion, i.e., for $v_\infty = v_0 = v_s$ (the adiabatic sound velocity).

The solution for the linearized hydrodynamic equations yields the following expression for $S(\mathbf{q},\omega)$:

$$S(\mathbf{q},\omega) = \frac{1}{\pi} S(\mathbf{q}) \frac{N_1(\omega)D_1(\omega) + N_2(\omega)D_2(\omega)}{D_1^2(\omega) + D_2^2(\omega)} \tag{3.9}$$

where

$$N_1(\omega) = -\omega^2 + \gamma D_T q^2 D_L q^2 + (1-1/\gamma)v_0^2 q^2 + b_1 q^2(\omega^2\tau + \gamma D_T q^2)/(1+\omega^2\tau^2), \tag{3.10}$$

$$N_2(\omega) = \omega[(\gamma D_T q^2 + D_L q^2) + b_1 q^2(1-\gamma D_T q^2\tau)/(1+\omega^2\tau^2)], \tag{3.11}$$

$$D_1(\omega) = v_0^2 q^2 D_T q^2 - \omega^2[\gamma D_T q^2 + D_L q^2 + b_1 q^2(1-\gamma D_T q^2\tau)/(1+\omega^2\tau^2)], \tag{3.12}$$

$$D_2(\omega) = \omega[-\omega^2 + v_0^2 q^2 + \gamma D_T q^2 D_L q^2 + b_1 q^2(\omega^2\tau + \gamma D_T q^2)/(1+\omega^2\tau^2)]. \tag{3.13}$$

In these equations, D_T is the thermal diffusivity and D_L is the longitudinal kinematic viscosity, defined as:

$$D_T = \lambda_T / \rho C_p , \tag{3.14}$$

$$D_L = (\eta_V + \tfrac{4}{3}\eta_S)/\rho , \tag{3.15}$$

with λ_T being the coefficient of thermal conductivity, $\gamma = C_p / C_V$ the heat capacity ratio, η_V and η_S the frequency-independent bulk and shear viscosities, respectively. The quantities D_T and D_L are diffusion coefficients for the diffusion of heat and longitudinal momentum, respectively. The linewidths, due to frequency-independent thermal and viscosity broadening are defined as (HWFM):

$$\Gamma_T = D_T q^2 , \tag{3.16}$$

$$\Gamma_L = D_L q^2 , \tag{3.17}$$

respectively.

The above result is simplified considerably for frequencies in the regime available to Brillouin spectroscopy for which $\omega \gg \Gamma_T$ (the width of the Rayleigh line). In this case, Eq. (3.9) becomes

$$S(\mathbf{q},\omega) = \frac{1}{\pi} S(\mathbf{q}) \frac{v_0^2 q^2 / \gamma [D_L q^2 + b_1 q^2 /(1+\omega^2\tau^2)]}{[\omega^2 - v_0^2 q^2 - b_1 q^2 \omega^2 \tau /(1+\omega^2\tau^2)]^2 + [\omega D_L q^2 + \omega b_1 q^2 /(1+\omega^2\tau^2)]^2} \tag{3.18}$$

For details on the derivation of the above results, see the original papers from Mountain[34,35] or the treatment in Chapter 10 of Ref. 36.

The most striking feature of the spectrum given by Eq. (3.18) is the presence of a second central component known as the Mountain peak, with a linewidth of the order of τ^{-1}. In the experimental spectra the existence of this relaxation mode is observed as a

broad background between the Rayleigh line and the Brillouin peaks, which in turn will appear asymmetrical and displaced from their "classical" position (at $\omega_0 = v_0 q$) to a new position $\omega_B = v_s q$. The effect is known as sound dispersion, i.e., $\omega_B > \omega_0$ and $v_s > v_0$. The Mountain peak is typically broad and has low intensity which makes it difficult for direct experimental observation but its effect on the sound velocity and the Brillouin linewidth can be measured.[37]

3.3. Structural relaxation in polymeric liquids (Wang's theory)

In a viscous molecular liquid such as a polymer melt, interactions between molecules as well as between segments of the same molecule play an important role in the Rayleigh-Brillouin spectrum. In light-scattering experiments, it was observed that Mountain's theory cannot account for the relatively large dispersion in the sound velocity, the maximum of the Brillouin linewidth with respect to temperature and the fact that the spectra are quite insensitive to the macroscopic viscosity and molecular weights beyond a certain low threshold value. In order to address those issues, Lin and Wang[38] assume that there is appreciable coupling between translation and structural rearrangement motions of the polymer chain in a longitudinal direction. The density fluctuations are coupled to velocity and energy fluctuations, and so, density, velocity and energy fluctuations form a complete set of dynamic variables, which are not coupled to other variables. In contrast to Mountain's approach, they consider coupling of internal as well as external degrees of freedom to translation. Similarly to Mountain, they assume a single exponential relaxation with characteristic relaxation time, τ_2. The result is an isotropic light-scattering spectrum characterized by a dynamic structure factor given by

the same general form as in Eq. (3.9), but the factors are now given by the following expressions:

$$N_1(\omega) = -\omega^2\{1+[\alpha_2''(\omega)/\omega]\} + \alpha_2'(\omega)\alpha_3' + (1-1/\gamma)\omega_0^2, \tag{3.19}$$

$$N_2(\omega) = \omega\{\alpha_2'(\omega) + \alpha_3'[1+\alpha_2''(\omega)/\omega]\}, \tag{3.20}$$

$$D_1(\omega) = -\omega^2\{\alpha_2'(\omega) + \alpha_3'[1+\alpha_2''(\omega)/\omega]\} + (\alpha_3'/\gamma)\omega_0^2, \tag{3.21}$$

$$D_2(\omega) = \omega\{-\omega^2[1+\alpha_2''(\omega)/\omega] + \alpha_2'(\omega)\alpha_3' + \omega_0^2, \tag{3.22}$$

where

$$\alpha_2'(\omega) = \frac{K_{22}(0)\tau_2}{1+\omega^2\tau_2^2}, \tag{3.23}$$

$$\alpha_2''(\omega) = -\frac{K_{22}(0)\tau_2^2\omega}{1+\omega^2\tau_2^2}, \tag{3.24}$$

$$\alpha_3' = \gamma D_T q^2. \tag{3.25}$$

In the above expressions, $\omega_0 = v_0 q$ is the relaxed sound frequency and the quantity $K_{22}(0)$ is proportional to the longitudinal elastic modulus, and can be written as

$$K_{22}(0) = \omega_\infty^2 - \omega_0^2 = (R_\omega - 1)\omega_0^2, \tag{3.26}$$

where $R_\omega = \omega_\infty^2/\omega_0^2$ is the relaxation strength, and $\omega_\infty = v_\infty q$.

The spectrum is qualitatively similar to the one obtained by Mountain with the central component due to the structural relaxation, and width determined by the inverse structural relaxation time, τ_2. Finally, τ_2 is the time required for the strain induced by the propagating sound wave to relax as the molecules rearrange themselves to a new equilibrium configuration.

3.4. Generalization of the Brillouin spectrum

In many practical cases the dynamics of the viscous liquid is more complicated and cannot be described by a single relaxation as in the cases considered above. Since the central Rayleigh line, due to the thermal diffusion mode, has a trivial Lorentzian lineshape and its linewidth is typically $\Gamma_T \ll \Gamma_B < \omega_B$, it is omitted from the following expressions. The isotropic scattered intensity can be written as

$$I(\omega) = \frac{I_0}{\omega} \mathrm{Im}\{[\omega^2 - \omega_0^2 - i\omega\gamma_0 - \omega m(\omega)]^{-1}\}, \tag{3.27}$$

or

$$I(\omega) = I_0 \frac{\gamma_0 + m''(\omega)}{[\omega^2 - \omega_0^2 + \omega m'(\omega)]^2 + \omega^2[\gamma_0 + m''(\omega)]^2}, \tag{3.28}$$

which is the power spectrum of a damped harmonic oscillator with a frequency dependent damping function $\gamma(\omega) = \gamma_0 + m''(\omega)$, where γ_0 is the frequency-independent damping, i.e. γ_0 contains all "fast" damping processes that are not explicitly represented by $m''(\omega)$. Eq. (3.28) is a generalization of Eq. (3.3) with all the unknown physics about the relaxation processes (thermal and structural relaxation) hidden in the complex function $m(\omega) = m'(\omega) + im''(\omega)$. This representation is very general since $m(\omega)$ is the Laplace transform of the memory function $m(t)$, which can be constructed to include structural relaxation, thermal relaxation, and translation-orientation coupling for liquids of anisotropic molecules.[28] In the simplest case, where $m(\omega) = 0$, i.e. no relaxation dynamics is present, Eq. (3.28) reduces to the Brillouin spectrum for simple monatomic liquids given by Eq. (3.3). In the case where $m(\omega)$ is chosen to represent the relaxing frequency dependent longitudinal viscosity with a single relaxation time, τ, the equation

reduces to the form introduced by Mountain, i.e. Eq. (3.18). If a structural relaxation is considered as the process responsible for the damping of the sound waves and included along with the coupling to internal (vibrational) degrees of freedom, the results of the Wang's theory are recovered.

Ideally, the $I_{iso}(\mathbf{q},\omega)$ spectra should be analyzed to yield $m(\omega)$ directly. However, in practice, this is very difficult since the spectra only cover a frequency range of one or two decades, while $m(\omega)$ extends over many decades. Furthermore, the shape of $I(\omega)$ is relatively insensitive to the detailed form of the memory function $m(\omega)$.[29] Usually, parameterized models for $m(\omega)$ are selected and the parameters are varied to optimize the fits at each temperature.

If a single relaxation time model is assumed (such as in the Mountain and Wang's theories), the prototype memory function is the single exponential relaxation $e^{-t/\tau}$. It is usually called the Debye relaxation and was first used by Maxwell in his theory of viscoelasticity. The complex function $m(\omega)$ has the form

$$m(\omega) = \Delta^2 \frac{i\tau}{1 - i\omega\tau} \tag{3.29}$$

In this case, the $m'(\omega)$ and $m''(\omega)$ can be conveniently separated

$$m'(\omega) = -\Delta^2 \frac{\omega\tau^2}{1 + \omega^2\tau^2}, \tag{3.30}$$

$$m''(\omega) = \Delta^2 \frac{\tau}{1 + \omega^2\tau^2}, \tag{3.31}$$

with Δ^2 being a coupling parameter signifying the strength of the relaxation. (Note that the definitions for $m'(\omega)$ and $m''(\omega)$ are equivalent to $\alpha_2''(\omega)$ and $\alpha_2'(\omega)$, given by

Eqs. (3.24) and (3.23), respectively.) The parameter Δ has units of frequency and will be compared to other traditional relaxation strength parameters in Sec. 3.5.

If more than one relaxation time contributes, the function $m(\omega)$ can be constructed as a sum over the individual contributions, and will be represented as a sum over terms like (3.29). In the continuum case

$$m(\omega) = \Delta^2 \int_0^\infty w(\tau) \frac{i\omega\tau}{1 - i\omega\tau} d\tau \,, \tag{3.32}$$

where Δ^2 is the total relaxation strength for all processes that couple to the longitudinal modes and $w(\tau)$ is the distribution of relaxation strengths for these processes. The integration is over all relaxation times, i.e. over all contributing relaxation processes.[37,39,40]

Another widely used form of the memory function, which assumes a specific distribution of relaxation times, is based on the stretched-exponential Kohlrausch-Williams-Watts[41] (KWW) function $e^{-(t/\tau)^{\beta_{KWW}}}$. An approximation to the Fourier transform of this function is the Cole-Davidson (CD) function[42, 43]

$$m(\omega) = \Delta^2 \left[\frac{i\tau}{(1 - i\omega\tau)^{\beta_{CD}}} \right] \tag{3.33}$$

Both Eqs. (3.29) and Eq. (3.33) have been frequently used, along with Eq. (3.28) to analyze Brillouin-scattering spectra. There are other more complicated models for the function $m(\omega)$,[44] which are mainly used when the temperature is reduced toward the glass transition temperature of the system and will not be discussed here. Instead, we will consider the parameters of the Maxwell-Debye and Cole-Davidson models and more specifically their use for fitting the experimental spectra.

The primary goal of the fitting procedure is to match the parameters to the apparent Brillouin frequency shift ω_B and Brillouin linewidth Γ_B in the experimental spectra. The real part $m'(\omega)$ at the frequency of the Brillouin peak, must be adjusted to shift the Brillouin peak from ω_0 to ω_B, and the imaginary part $m''(\omega)$, at the frequency of the Brillouin peak, must be adjusted so that $\gamma_0 + m''(\omega)$ will give the correct Brillouin linewidth. If these two conditions are simultaneously satisfied, then the particular form chosen for $m(\omega)$ will only influence the details of the lineshape. By comparing Eq. (3.28) to Eq. (3.3) we see that ω_B and Γ_B are approximately given by

$$\omega_B^2 = \omega_0^2 + \omega m'(\omega)\Big|_{\omega\to\omega_B} \tag{3.34}$$

$$\Gamma_B = \gamma_0 + m''(\omega)\Big|_{\omega\to\omega_B} \tag{3.35}$$

The typical temperature dependence for some of the quantities is illustrated in Fig. 3.2 (following experimental data for PEO with 16% $LiClO_4$, presented in Chapter 6). The temperature behavior of ω_B and Γ_B is typical for samples with a relaxation process active in the gigahertz frequency range. At the high-temperature limit, the characteristic time for the process is short relative to the inverse Brillouin frequency, i.e. $\omega_B\tau \ll 1$ and the relaxation does not couple effectively with the sound wave. The limiting values for ω_B and Γ_B are ω_0 and γ_0, respectively. In the region of the relaxation, the characteristic time is of the order of the inverse Brillouin frequency, i.e. $\omega_B\tau \approx 1$ and the strong coupling results in dispersion of $\omega_B(T)$ (dispersion in the sound velocity) and a maximum in $\Gamma_B(T)$ (maximum in the sound attenuation). At lower temperatures, the relaxation time becomes long compared to the frequency of the sound wave, i.e. $\omega_B\tau \gg 1$

and ω_B and Γ_B approach their low temperature limiting values of ω_∞ and γ_0, respectively.

If all parameters I_0, ω_0, γ_0, Δ^2, τ and β_{CD} are kept as free fitting parameters, one can obtain excellent fits to the experimental spectra; however many of the parameters are rather strongly coupled making the fits unstable and the resulting values unreliable. It is preferable to fix as many parameters as possible using independently determined values. This is especially the case for ω_0 and γ_0 which can be inferred from low frequency (MHz) ultrasonic measurements of sound speed and attenuation. Here, we consider each of the parameters and their temperature behavior.

(1) I_0 is the integrated intensity of the Brillouin spectrum and it is not strongly coupled to the other parameters. It can be reliably determined from the fit provided that

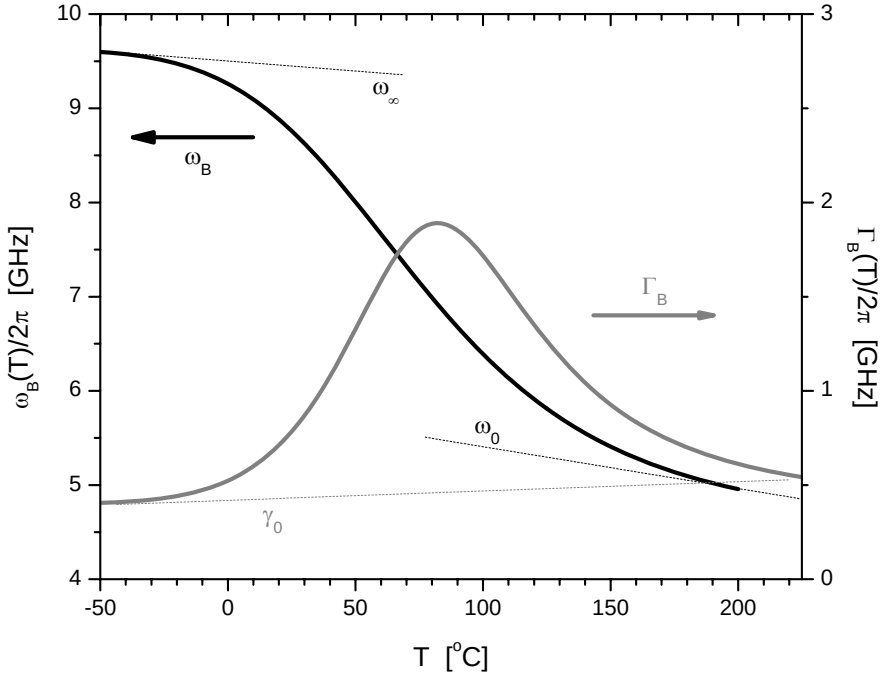

Fig. 3.2 – Temperature dependence of ω_B and Γ_B

the background is well determined.

(2) $\omega_0(T)$ can be determined from the low-frequency limiting value of the adiabatic sound velocity since $\omega_0 = v_0 q$. The value of $v_0(T)$ is usually measured by ultrasonic measurements in the MHz frequency range (typically in the range from 1 MHz to 15 MHz). Alternatively, $v_0(T)$ can be calculated using the thermodynamic relation $v_0 = \sqrt{\gamma / \beta_T \rho}$ if the heat capacity ratio, γ, the isothermal compressibility, β_T, and the mass-density, ρ are known as a function of temperature. In addition, the refractive index $n(T)$ must be known since it determines the value of the scattering wavevector $q(T) = (4\pi n(T)/\lambda)\sin(\theta/2)$ as a function of temperature. The fits to Eq. (3.28) are very sensitive to the value of $\omega_0(T)$; therefore the individual uncertainties of all the above quantities can render the calculated $\omega_0(T)$ unusable in the fits. The temperature dependence of ω_0 is usually weak. Nevertheless, regarding ω_0 as a constant or even a linear function of temperature, leads to unsatisfactory fits. $\omega_0(T)$ usually has a weak curvature with temperature.

(3) $\gamma_0(T)$ represents the "regular" damping of the sound waves by anharmonic processes not related to relaxations in the gigahertz frequency range. It can also represent a simple frequency-independent approximation for the fast limit of the structural relaxation not included in models such as the Maxwell-Debye or the Cole-Davidson relaxation. Usually, γ_0 is taken as a temperature-independent constant, fixed from the Brillouin linewidth at low temperature. However, since anharmonic damping processes often tend to become stronger with increasing temperature, γ_0 may increase with T.

Also, at temperatures well above the temperature of the maximum Brillouin linewidth, the linewidth due to γ_0 plus structural relaxation is approximately given by $\Gamma_B \approx \gamma_0 + \Delta^2\tau$. Fits with constant γ_0 often give Δ^2 values that increase at high temperatures, a result that appears to be unphysical. This apparent increase in Δ^2 can be avoided by allowing γ_0 to increase with increasing T, which unfortunately results in introducing additional parameters. The best solution is to calculate $\gamma_0(T)$ from independent ultrasonic data for sound attenuation, if available.

(4) $\Delta^2(T)$ represents the strength of the relaxation or the coupling between the propagating sound wave and the internal and external degrees of freedom in the system. Since at high temperatures $\omega_B \approx \omega_0$ and $\Gamma_B \approx \gamma_0 + \Delta^2\tau$, the effective fitting parameter at high temperature is the product $\Delta^2\tau$. So if Δ^2 and τ are both free parameters, the fits tend to be very unstable. $\Delta^2(T)$ is expected to monotonically decrease with increasing temperature, therefore any apparent increase of the values of Δ^2 with increasing temperature should be suspect.

(5) $\tau(T)$ is usually regarded as the parameter of greatest importance. On one hand, qualitatively it is desirable to not only determine the average relaxation time (the first moment of the distribution) but also the width and the shape of the distribution as a function of temperature. By assuming a particular model, such as the Maxwell-Debye (single-exponential) or the Cole-Davidson (stretched-exponential), we already impose restrictions on the form of the relaxation. In the former case, we merely determine an average value of τ, and in the later case, the width of the distribution is determined by β_{CD}. On the other hand, the temperature dependence of $\tau(T)$ and $\beta_{CD}(T)$ is also very

important. For example, the temperature dependence of $\tau(T)$ is considered a primary criterion for assigning the structural relaxation as primary or secondary relaxation.[45] Based on experimental results, several empirical forms for the temperature dependence of the average relaxation time have been used with varying success. Two of them are widely used in relation to the α and β relaxations, the Arrhenius equation

$$\tau = \tau_0 \exp\left(\frac{E_a}{RT}\right) \tag{3.36}$$

or the Vogel-Tammann-Fulcher (VTF) equation

$$\tau = \tau_a^{'} \exp\left(\frac{E_a^{'}}{R(T - T_0)}\right), \tag{3.37}$$

where E_a and $E_a^{'}$ are activation energies, R is the molar gas constant and T_0 is a temperature below the nominal glass transition temperature as determined by calorimetric measurements and is usually left as a free fitting parameter. In dielectric measurements of bulk polymer systems, it is generally accepted that Arrhenius temperature behavior is a signature of the secondary β-relaxation and VTF behavior is a signature of the primary α-relaxation.[45,46] The α-mode involves a larger range of the polymer chain and involves cooperative motion, while the β-mode is more local, limited to short range motions. Usually, the cooperative α-mode is too slow to have any effect on the high frequency Brillouin scattering. As was found in most experiments, the structural relaxation responsible for the maximum sound attenuation in Brillouin spectra is closely related to the β-relaxation.

3.5. Relaxation strength

As we already mentioned in the previous section, the coupling parameter Δ^2 can be interpreted as a measure of the relaxation strength observed in Brillouin scattering spectra. It is proportional to the integrated area under the sound loss peak. Once the origin of the relaxation is identified, it can be used to calculate other important properties. For example, in the Mountain model the relaxation is due to coupling of the acoustic modes to internal (vibrational) degrees of freedom. In this case, the relaxation strength, R_ω is defined as[29,47,48]

$$R_\omega = \frac{(C_p - C_i)C_V}{(C_V - C_i)C_p}. \tag{3.38}$$

In this way, R_ω is related to the coefficient b_1 defined in Eq. (3.8) since

$$R_\omega - 1 = \frac{(C_p - C_V)C_i}{(C_V - C_i)C_p} \tag{3.39}$$

therefore

$$b_1 = (R_\omega - 1)v_0^2\tau. \tag{3.40}$$

R_ω is also related to ω_0, ω_∞ and Δ^2 through the following equations

$$R_\omega = \frac{v_\infty^2}{v_0^2} = \frac{\omega_\infty^2}{\omega_0^2} \tag{3.41}$$

$$\Delta^2 = \omega_\infty^2 - \omega_0^2 = (R_\omega - 1)\omega_0^2. \tag{3.42}$$

Comparing (3.42) to Eq. (3.26) shows that $\Delta^2 = K_{22}(0)$ in the case of a structural relaxation.

Another useful way of defining the relaxation strength is through the complex longitudinal modulus $M^* = M' + iM''$, where M' is the storage modulus and is a

measure of the energy stored elastically during deformation, and M'' is the loss modulus – a measure of the dissipated energy. Both the storage and the loss moduli are functions of frequency and temperature. When the system undergoes relaxation, the complex modulus can be separated into a frequency-independent part M_0 and relaxing part proportional to the relaxation strength, M_r. For a process with a single relaxation time

$$M^*(\omega) = M_0 + M_r \frac{i\omega\tau}{1+i\omega\tau}. \tag{3.43}$$

We can also introduce the high-frequency limiting longitudinal modulus $M_\infty = M_0 + M_r$. This approach, which is preferred by many authors,[21,29,39] is equivalent to defining frequency-dependent relaxing longitudinal viscosity as in Eq. (3.7). The connection between the longitudinal modulus approach and the one given above for the memory function $m(\omega)$ is straightforward. The quantities are related through the following expressions:

$$M' = \frac{\rho}{q^2}\left(\omega_0^2 + \omega m'\right) \quad \text{and} \quad M'' = \frac{\rho}{q^2} m'' \tag{3.44}$$

$$M_0 = \frac{\rho}{q^2}\omega_0^2, \quad M_\infty = \frac{\rho}{q^2}\omega_\infty^2 \quad \text{and} \quad M_r = \frac{\rho}{q^2}\Delta^2 \tag{3.45}$$

Finally, we consider the difference between the Maxwell-Debye, Cole-Davidson and KWW functions. As we already pointed out, the exact form of the function $m(\omega)$ has only a weak effect on the Rayleigh-Brillouin spectrum itself. Hence, its determination from spectra alone is highly problematic and the result is in most cases ambiguous. On the other hand, if the experiment allows a measurement of ω_B and Γ_B as a function of frequency, there is a good chance the appropriate form of the relaxation can be identified. The most convenient representation follows from Eqs. (3.34) and (3.35):

$$\omega_B = \sqrt{\omega_0^2 + \omega m'(\omega)} \tag{3.46}$$

$$\omega\Gamma_B = \omega\gamma_0 + \omega m''(\omega) \tag{3.47}$$

Using realistic values for the various parameters involved, we plot ω_B and $\omega\Gamma_B$ as a function of ω for different forms of $m(\omega)$ in Fig. 3.3. The first pair of plots (a, d) compares Maxwell-Debye relaxation to Cole-Davidson relaxations with two different values of β_{CD}. The second pair of plots (b, e) compares a single-relaxation process to a two-step relaxation with the same overall relaxation strength. Both relaxations in the double-step relaxation are chosen as single-exponential steps for simplicity. The third pair of panels compares a Cole-Davidson relaxation to the Laplace transform in frequency space of a KWW function with $\beta_{CD} = \beta_{KWW}$. (The two functions can be forced

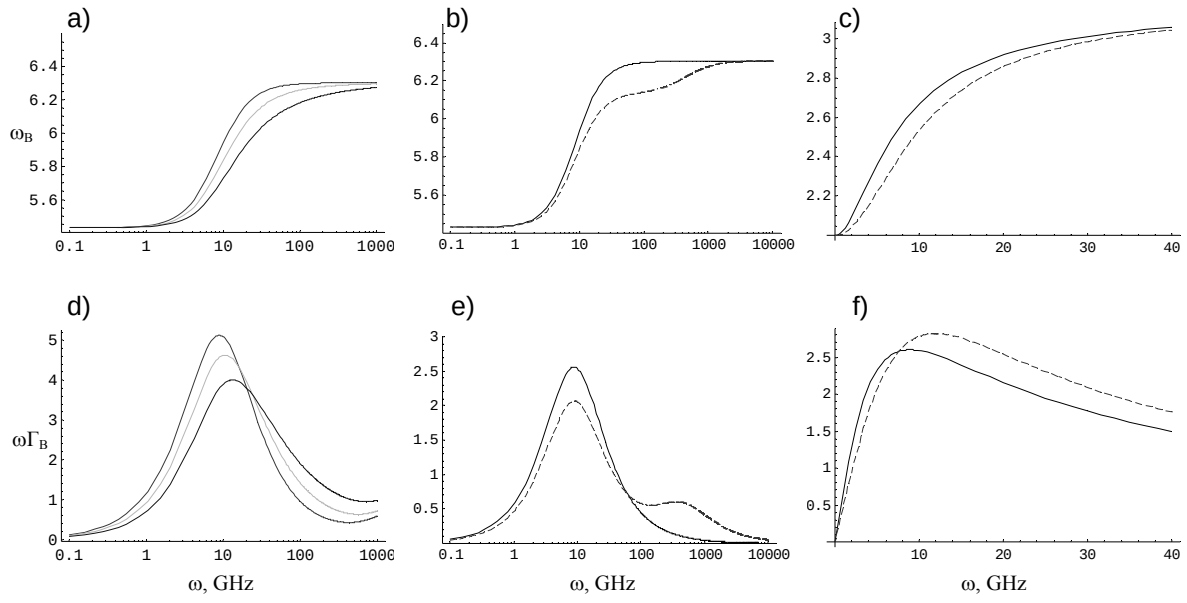

Fig. 3.3 – Comparison between different relaxation functions:
a) & d) from left to right: Cole-Davidson function with $\beta = 1$, 0.8 and 0.6;
b) & e) single Maxwell-Debye (solid) vs. two-step (dashed) relaxation;
c) & f) Cole-Davidson (solid) vs. KWW function (dashed) with $\beta_{CD} = \beta_{KWW}$ and $\tau_{CD} = \tau_{KWW}$; Note the logarithmic frequency scale in the first 4 panels.

to approximately overlap if certain relations between β_{CD} and β_{KWW} as well as between τ_{CD} and τ_{KWW} are imposed.[42,43]) Although the experimental frequency range of the Brillouin scattering experiment is not nearly as wide as the range used in these plots, useful information can still be obtained. For example, using this method we were able to clearly resolve a double step relaxation in the PEO/$LiClO_4$ system, as will be shown later. This approach is rarely mentioned in the literature, since frequency-dependent measurements of ω_B and Γ_B are very difficult to perform with conventional Fabry-Perot interferometers. One of the few successful examples is the series of experiments performed using the superheterodyne technique (which covers a lower frequency range than the Fabry-Perot interferometry – see Fig. 1.1) by Tanaka and Sonehara, briefly mentioned earlier.[13-15] Another example is an early attempt to demonstrate double-step relaxation in toluene by employing Fabry-Perot interferometry at six angles.[49] To our knowledge, this is the only Fabry-Perot based experiment of this kind and with the highest number of scattering angles reported in the literature to date. In contrast, the fiber-optic detection used in our experimental setup allows us to perform such measurements with the plane-parallel Fabry-Perot interferometer in a continuous range of angles in the range between 20^o and 160^o without any difficulty.

CHAPTER 4

DYNAMIC AND THERMODYNAMIC PROPERTIES OF POLYMER ELECTROLYTES

4.1. Glass-forming liquids – dynamics and relaxation phenomena

The complete description of both the thermodynamic and relaxation properties of glass-forming substances from a statistical-mechanics point of view is of great complexity. Such systems consist of densely packed interacting molecules and therefore considering the effects of many-body interactions is unavoidable. The various materials falling in the category of "glass-formers" are individually characterized by their chemical bonds and structure. In addition, during the glass-transition many thermodynamic properties such as specific volume, entropy, etc., undergo appreciable changes as a function of temperature (or pressure). All that complexity prevents the development of a complete theoretical description of the relaxation processes and the glass transition itself. Nevertheless, there is tremendous amount of experimental data on many kinds of materials, accumulated by different experimental techniques, which allow the materials and the observed phenomena to be organized into a number of well-established categories according to their general properties. One example is the categorization of the processes according to their characteristic time scale or relaxation rate, established on the basis of mechanical and broadband dielectric spectroscopy measurements and nowadays

commonly accepted in all dynamic methods dealing with glass-forming liquids. References to this categorization were already made in the previous chapter where we used the terminology for the "structural relaxation" to explain on a phenomenological level the underlying dynamics giving rise to the observed light-scattering spectra. In this chapter, we attempt to consider these phenomena in the much broader context of glass-former dynamics and to relate the light-scattering results to experimental data obtained by other dynamic techniques.

A schematic plot of broadband dielectric loss spectra demonstrating the most common relaxations for two typical classes of materials is shown in Fig. 4.1. The dominating peak at low frequencies is the structural α-peak. The decay is usually not a single-exponential function of time. Instead, it is well approximated by the KWW

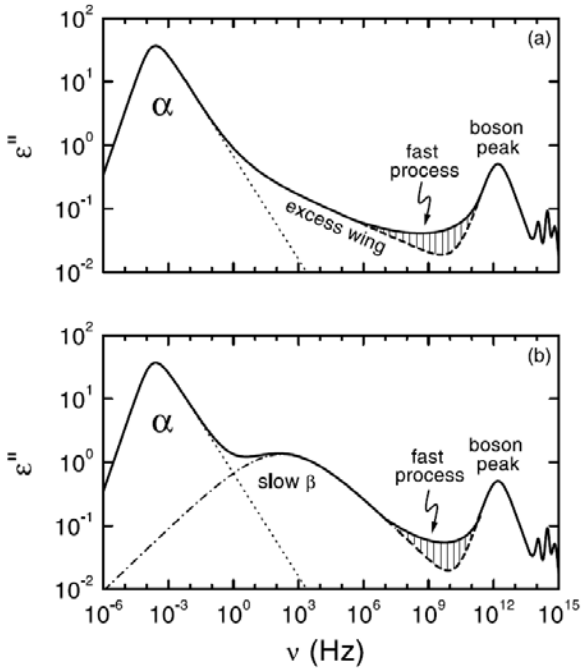

Fig. 4.1 – Schematic view of frequency dependent dielectric loss in two types of glass-forming materials: (a) type A glass-formers showing an excess wing and (b) type B glass-formers with well-resolved β-relaxation peak.

stretched exponential expression $e^{-(t/\tau)^{\beta_{KWW}}}$, with $0 < \beta_{KWW} \leq 1$. The KWW function does not have a closed analytical form in frequency space. The transformation into the frequency domain is done by infinite series expression derived by Williams, Watts *et al.*[50, 51] or by performing a numerical Laplace transformation of the KWW expression. The Havriliak-Negami (HN) function

$$H(\omega) = \frac{1}{\left[1 + (i\omega\tau)^a\right]^b}, \tag{4.1}$$

defined in frequency space is closely related to the KWW function.[42,43] In the HN function, a and b are empirical constants, $0 < a \leq 1$, $0 < b \leq 1$. For $b = 1$ the expression becomes the Cole-Cole (CC) function, whereas for $a = 1$ it is equivalent to the Cole-Davidson (CD) equation discussed in the previous chapter. The HN function is one of the most widely used functions for fitting the relaxation data for polymers. As was already mentioned, the temperature dependence of the average relaxation time for α-relaxations generally follows the VTF equation [Eq.(3.37)]. If the α-relaxation is studied over a very broad temperature range, a single VTF expression is not sufficient to fit the data. It was shown[52,53] that the data follows an Arrhenius expression at high temperatures with a crossover to a VTF expression at some temperature T_A and another crossover to a second VTF expression at a lower temperature T_B.

On the high-frequency side of the α-relaxation, one usually finds either an excess wing (also called "high-frequency wing") for one class of materials or a well resolved β-peak for another class of materials [Fig. 4.1 a) and b)]. Until recently, it was commonly believed that the excess wing and the β-relaxations are different phenomena and the two classes of glass-formers were named – "type A" with an excess wing and without a β-

peak, and "type B" – without excess wing but with a β-process.[54] However, a careful inspection of the available data shows that the so-called "excess wing" in type-A glass-formers can be explained by a β-peak submerged under the dominating α-peak whose high-frequency side appears as an excess wing to the α-peak. This notion was recently strongly corroborated by two different types of experiments: (1) by aging experiments by Lunkenheimer *et al*.[55,56] on several typical type-A systems, glycerol, propylene carbonate (PC), Salol and propylene glycol (PG), and (2) by dielectric measurements as a function of pressure by Roland and Casalini.[57,58] One of the conclusions of this debate and its resolution is that it is not unusual to observe multiple overlapping relaxations in complex materials, although it is often very difficult to resolve them experimentally. This makes our angle-dependent approach in the Brillouin spectroscopy especially appealing.

The β-processes are observed at higher frequencies than the α-processes and are commonly referred to as "secondary" relaxations. The secondary relaxation appearing closest to the α-relaxation is referred to as the slow β-relaxation. At yet higher frequencies contributions from other processes can sometimes be detected which are called the fast β-relaxation (or γ-relaxation). While in some materials, especially polymers, the β-relaxations can be explained by intramolecular degrees of freedom, Johari and Goldstein (JG) demonstrated that they exist even in glass-forming materials where the internal degrees of freedom can be excluded. The β-relaxation is a JG process if it involves motion of the entire molecule (or polymer repeat unit) as opposed to non-JG relaxations which are due entirely to intramolecular degrees of freedom (or motion of pendant groups in polymers). When observed, the JG relaxation is the slowest of the secondary relaxations. The β-relaxation data is often fit to the Cole-Cole function or even

to Debye-Maxwell single-exponential relaxation. The average relaxation time of the β-processes typically follows Arrhenius temperature dependence.

Beyond their importance as fundamental properties of a material, the relaxation processes are of particular significance for ion-conducting polymer electrolytes. The most important property in such systems, the ionic conductivity, is governed by two major factors: the concentration of free charge-carriers (ions) and the ion mobility. They are both strong functions of temperature and salt concentration. While the first factor is primarily a function of the solubility of the salt in the polymer host, the second factor depends strongly on the local flexibility of the polymer chains since the ion diffusion is coupled to and assisted by the local motions in the polymer. As was noted above, the various relaxations in the polymer material reflect the structural dynamics on different length- and timescales. Therefore, by studying the relaxation dynamics we gain information directly affecting the performance of the material as an electrolyte.

Fig. 4.2 shows the conductivity of PEO/$LiClO_4$ as a function of salt concentration for three different temperatures above the melting point.[59] When the salt is introduced into the polymer the conductivity increases rapidly due to the increased number of charge carriers. At large enough concentrations, the increase in the number of free charge carriers will slow down and eventually saturate due to recombination of the salt's anions and cations. Although this effect is clearly present, it is relatively weak at salt concentrations below 30wt.-% due to the large dielectric constant for PEO (in the melt $\varepsilon \approx 8$) and it is not sufficient to explain the early leveling followed by a steep decrease in the conductivity with increasing salt concentration. Therefore, reduced ion mobility is considered to play a significant role in the reduction of conductivity.

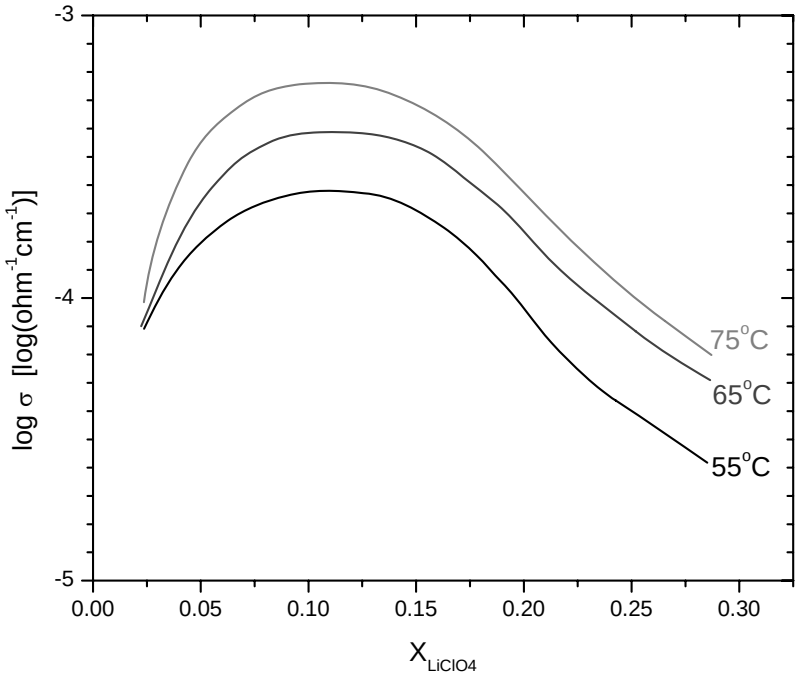

Fig. 4.2 – Conductivity of PEO-melt/$LiClO_4$ electrolytes as a function of salt concentration and temperature. [Ref. 59]

In the remainder of this chapter we summarize the results found in the literature on the thermodynamic and relaxation behavior of PEO and PEO/$LiClO_4$ complexes, primarily obtained by dielectric measurements and rheometry. Later, the Brillouin light-scattering results will be discussed in the context of the relaxation dynamics and the measured elastic and structural dynamic properties will be correlated to the reduced ion mobility in the electrolyte.

Some degree of caution should be exercised when comparing results from dielectric and light-scattering measurements. Some authors[60] emphasize that the two measurements, in principle, probe different microscopic mechanisms and based on the differences observed in the measured timescales and activation energies, they might even

probe different relaxations. As we noted above, relaxation modes that are coupled to longitudinal density fluctuations will be observed in a polarized (VV) light-scattering experiment. At the same time, in dielectric relaxation one measures the dynamic behavior of an ensemble of electric dipoles, presumably associated in a well-understood manner with the polymer backbone.[61] The dielectric α-process results from dipole reorientations associated with main-chain bond rotations. Although reorientations might couple to the density fluctuations through rotation-translation coupling, this is usually considered a weak mechanism. On the other hand, a secondary dielectric mechanism (a β-process) involving overdamped torsional (twisting) oscillations of chain segments about their equilibrium position is expected to couple well with the density fluctuations as it is more governed by local elastic restoring forces. Therefore, the secondary processes are more likely to be detected by Brillouin scattering measurements. Nevertheless, at high temperatures and high frequencies these two relaxations merge into a single process. As will become clear in the next section, the Brillouin measurements for PEO melts presented here are at temperatures and frequencies well above the merging region, where only a single dielectric relaxation process appears to exist.

4.2. Literature results for PEO and PEO/salt electrolytes

Fig. 4.3 shows a compilation of relaxation data for PEO found in the literature. It is presented in a typical "relaxation map" plot showing $\log f$ vs. $1/T$ dependence. There are two groups of data. The data labeled with the subscript "*c*" are identified with very low frequency processes in the crystalline phase and obtained by mechanical spectroscopy.[62,63] They are shown only for completeness and will not be discussed further

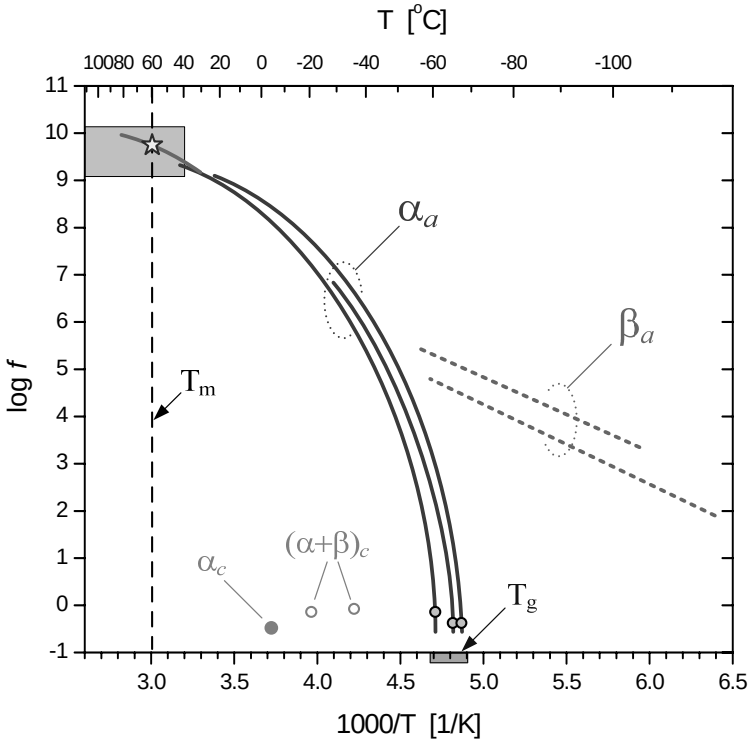

Fig. 4.3 – Relaxation map for poly(ethylene oxide) from mechanical and dielectric spectroscopy measurements (see the text for references). The single point (star) is from a Brillouin scattering measurement. The shaded area represents the range of the present experiment.

since the present study is concerned only with the amorphous phase. The rest of the relaxation data labeled by the subscript "*a*" pertain to the amorphous phase. The dominant process studied by broadband dielectric measurements[63,64] and mechanical measurements at low frequencies[62,63] is the main glass-rubber relaxation (also called the "dynamic" glass transition) labeled as α_a. It appears as a family of curves due to the different molecular weight and degree of crystallinity of the samples. At low temperatures and low frequencies the dielectric (lines) and mechanical data (circles) coincide and the curves extrapolate to the "static" glass transition temperature region. At the high-temperature and high-frequency end of the α_a relaxation, Porter and Boyd[64]

showed that the relaxation frequency is continuous through the melting point ($T_m \approx 60^o C$ for the high molecular weight samples used in their measurement). The latter result strongly confirms that the α_a relaxation is due to dynamics in the amorphous phase. The process labeled β_a was studied by Ishida *et al.*[65,66] and was identified as a local twisting motion of main chains in both non-crystalline regions and the defective regions within the crystal phase. As is evident in the plot, the two relaxations in the amorphous phase appear to merge near -35°C which is well below the melting temperature. It should be noted that in the original papers[62-66] as well as in Ref. 67 the relaxations are labeled as α, β and γ in increasing order with decreasing temperature without regard to the phase they appear in. The notation used in Fig. 4.3 follows the discussion in the previous section and stresses the notion that the α_a is the primary (glass-rubber) and β_a is the secondary (JG) relaxation in the amorphous phase of the polymer.

The shaded area at the high-temperature, high-frequency end of the diagram represents the range accessible for the Brillouin scattering experiment in the PEO melt. The lower temperature limit is set by the melting temperature, which for the PEO-1K sample is 40°C. At the high-temperature end, the present setup allows temperature as high as 150°C. The frequency range accessible using the plane-parallel Fabry-Perot interferometer is between 2 GHz and 20 GHz. The single data point represented by a star at $T = 60^{\circ}\mathrm{C}$ and $f \approx 6$ GHz corresponds to a Brillouin scattering measurement by Patterson and Latham[68] which is in excellent agreement with the dielectric data by Porter and Boyd.[64] This agreement suggests that the high-frequency dielectric and the Brillouin light-scattering measurements probe the same process which is the overlapping α_a and

β_a processes shown on the dielectric relaxation map. Finally, Gray, Vincent and Kent[59] used time domain dielectric spectroscopy to study the PEO/$LiClO_4$ electrolyte as a function of composition and temperature. Their data for pure PEO match the Porter and Boyd data shown on the relaxation map. With increasing salt concentration the characteristic time slowed down while the stretching parameter was reduced from close to 0.9 for pure PEO to about $\beta \approx 0.5$ at the highest salt concentration studied (28.7%-wt.). Both effects were attributed to the increased transient cross-link density due to the increased number of Li^+ ions.

Prior to the present work, Brillouin light-scattering techniques did not have the necessary resolution and frequency range to investigate the details of the relaxations in the high-frequency high-temperature range and to illuminate, for example, the very important question of the existence of multiple distinct relaxations vs. a single merged process. There is very strong evidence, at least in the case of PEO-melt/$LiClO_4$ and PEO-melt/LiTFSI (TFSI = $N(CF_3SO_2)_2$) electrolytes, that in this frequency range there are distinct relaxation processes. Mao *et al.*[69,70] reported quasielastic neutron scattering (QENS) and neutron spin-echo spectroscopy (NSES) measurements, clearly demonstrating multiple relaxations in the electrolyte systems. While they observe a single broad relaxation in the case of pure PEO melt with $\beta \approx 0.6-0.7$ and $\tau \approx 16$ ps, in the case of $LiClO_4$ electrolyte there are two relaxations and in the case of LiTFSI three relaxations. They identified the slower relaxation with an α-relaxation mode resulting from translational diffusion of the chain segments which is also similar to the process observed in pure PEO melt, but it is considerably slowed down upon addition of salt due to the increased transient cross-linking effect of the Li^+ ions. They observed that the

stretching β-parameter was considerably reduced by increasing salt concentration which is similar to the dielectric measurement result by Gray *et al*.[59] The faster mode of rotational character was attributed to conformal fluctuations of the chain segments between the transient cross-links formed by the Li^+ ions. For the β-process in the $LiClO_4$ electrolyte they found $\beta \approx 1$ and $\tau \approx 25$ ps (the characteristic time for the slow α-process was longer than 100 ps and was outside their experimental window).

In view of the above results it was apparent that it would be highly desirable to perform a detailed investigation of the relaxation dynamics using the Brillouin light-scattering technique. The fiber-coupled detection employed in the present experimental system facilitates measurements over a range of scattering wavevectors allowing measurement of the Brillouin frequency and linewidth as a function of frequency, as well as temperature and composition of the samples. As will be shown later, with this method it was possible to resolve the double-step relaxation in the PEO-melt/$LiClO_4$ electrolyte directly in the density fluctuation spectrum. To our knowledge, this is the first time such a result is reported.

CHAPTER 5

EXPERIMENTAL

5.1. Samples and sample preparation

In this work, experimental results using toluene, neat poly(ethylene oxide), (PEO) melts and PEO melt/$LiClO_4$ electrolytes are presented. High-purity spectrometric grade toluene, 99.9% minimum by gas chromatography (GC) was supplied by *Burdick & Jackson* (Muskegon, Michigan). A low molecular weight poly(ethylene glycol) dimethyl ether sample ($M_W = 1050$, $M_N = 1000$), designated here as "PEO-1K sample", with a narrow molecular weight distribution ($M_W / M_N = 1.05$) was custom synthesized by *Polymer Source (PS) Inc.* (Doval, Canada). PEO chain ends were "capped" with methyl groups to avoid complicating behavior associated with chain hydroxyl end groups. Based on rheological measurements, the critical value for the melt entanglement molecular weight is about 3500, therefore the PEO-1K sample is unentangled in the melt. The melting point is about 38°C, the glass transition temperature is $T_g \approx -40^{\circ}\mathrm{C}$, the density is $\rho \approx 1.1$ g/cm^3 at 50°C, and the viscosity is $\eta \approx 45$ cP at 50°C.[8,71] To produce optically clear samples, after receipt, the PEO is further purified using multiple dissolution rinses with methanol and diethyl ether, each rinse followed by precipitation at $-40^{\circ}\mathrm{C}$. After the final rinse and filtration, the PEO is dried in a desiccator under high vacuum and the sealed desiccator is then placed in a stainless-steel glove box (*Labconco*, Kansas City,

Missouri), where all subsequent sample preparation steps were carried out. The glove box was filled with dried and purified nitrogen with the moisture level maintained below 10 ppmV. Keeping PEO samples dry is essential; PEO is hygroscopic and even small amounts of absorbed water can dramatically affect PEO melt behavior. The absence of water in PEO prepared this way, as well as the complete capping of PEO chains, were previously verified by measuring the infrared absorption spectrum of a representative sample.[6] The lithium perchlorate used in this work was an anhydrous highly purified grade (*Fluka*, Buchs, Switzerland) first dried in a vacuum oven and then further dried under high vacuum in a desiccator before being placed in the glove box. The PEO/$LiClO_4$ solutions were prepared in the dry box by controlled evaporation of methanol from PEO/$LiClO_4$/methanol solutions (anhydrous methanol, *J. T. Baker*, Phillipsburg, New Jersey). All samples were filtered through 0.2 μm pore-size Teflon membrane filters (*Millipore*, Bedford, Massachusetts) into dust-free light-scattering cells. Two types of square spectrofluorometric cuvettes were used (5-mm and 10-mm, semi-micro cells from *Starna Cells*, Atascadero, California) in the 90^o scattering angle measurements. Standard 5-mm NMR tubes (*Wilmad Glass*, Buena, New Jersey) were used in the angle-dependent measurements.

5.2. Data collection and analysis

As it was shown in Fig. 2.1, a ramp generator provides the scanning voltage for one of the Fabry-Perot interferometer mirrors and the time-synchronizing signal for the multichannel scaler (MCS) from *Ortec* (Oak Ridge, Tennessee). One sweep of the F-P interferometer was typically 1 sec. and was recorded in 3000 channels of the MCS.

Typical accumulation times for the spectra were from 300 to 600 seconds except when scattering signals were weak, when they were as long as 3000 seconds. Each accumulated spectrum consisted of three consecutive orders of the F-P interferometer. A typical data file for toluene is shown in Fig. 5.1. The first and the last orders contain the instrumental function of the interferometer and the central order contains the sample's spectrum. The measurement was realized by using two mechanical beam shutters introduced in the optical setup (not shown in Fig. 2.1). The beam shutters were synchronized with the scanning ramp voltage and switched the signal at the input of the interferometer between attenuated laser light (in the first and the last part of the scan) and scattered light from the sample (in the central part of the scan). This format for recording the data files has

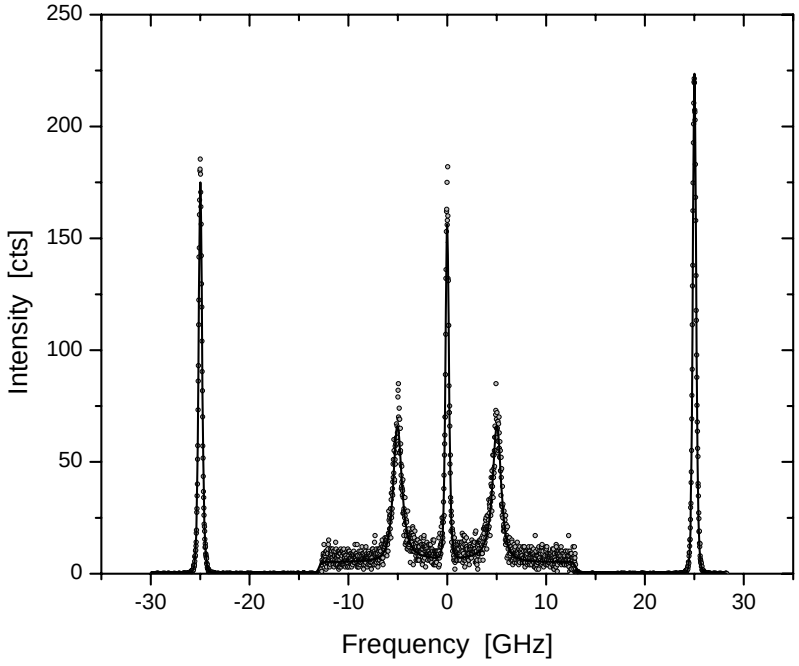

Fig. 5.1 – Representative data file containing two instrumental functions and the Rayleigh-Brillouin spectrum of toluene in the center, as well as the least-squares fit to the spectrum (solid line)

several practical advantages. First, recording two complete free spectral ranges (FSR) in each file allows for reliable calibration from MCS channel number to frequency of the horizontal axis, even if the interferometer scan is not perfectly linear. For example, in the range the F-P interferometer was used, it was estimated that the deviation from linearity is less than 0.1%, which is typical for the type of PZT elements used for scanning. Second, the first instrumental peak in each scan was used to monitor the drifts in the interferometer and for implementing a standard feedback algorithm to dynamically adjust the bias of the ramp generator and perform simple stabilization control. Third, the recorded instrumental function was used in the fitting procedure as described below.

The spectra obtained with the Fabry-Perot interferometer, such as the one shown in Fig. 5.1, are broadened by the instrumental function. The observed spectrum is a convolution of the true spectrum with the instrumental profile. For example, the first and the third instrumental peaks, as well as the central Rayleigh peak (in the central spectrum) should appear as δ-functions on this frequency scale and the two Brillouin peaks should have about 2/3 of their apparent width. In order to extract the actual underlying Rayleigh-Brillouin spectrum it is necessary to de-convolve the instrumental function from the experimental spectrum. In practice, mathematical deconvolution cannot be implemented since it involves a strongly ill-behaved procedure.[20] Instead, the theoretically calculated spectrum (fit) is convoluted with a realistic representation of the instrumental profile and the result is compared to the experimental data. Then the parameters are iteratively optimized using a nonlinear least-squares fitting routine. In order to obtain good deconvolution one is required to first obtain the proper instrumental function.

The instrumental profiles were briefly discussed in Section 2.2. Theoretically, for a triple-pass F-P interferometer, the instrumental function is best described by a Lorentzian to the third power, L^3. In practice, it can be slightly distorted or asymmetric in the real spectra due to various imperfections of the interferometer's components and alignment. Also the instrumental profile can slightly change during measurements with long duration or between measurements due to gradual misalignment, which in our experiment is not controlled by an active feedback adjustment. Although the described variations in the instrumental profile were, in practice, minuscule it was observed that they affected significantly the quantities extracted from the fit, especially the Brillouin linewidth. For example, about 10% to 15% error in the estimate of the instrumental function can result in a comparable error in the Brillouin linewidth, which is as big as the error bar due to all other contributions (see below). By collecting and recording the exact instrumental profile along with each spectrum (under the exact same conditions) and consecutively analyzing it within the fitting procedure, it was possible to reduce this significant source of error at least tenfold. The experimental instrumental profile is approximated by an L^3 function multiplied by a quadratic correction to account for the asymmetry mentioned above. The condition for equal area (integrated intensity) of the instrumental peaks is used as a constraint on the parameters. The described fitting function results in excellent fits to the instrumental profile, as is evident for the first and the last peaks in Fig. 5.1. This part of the fit also yields the overall background from the PMT dark count, typically about 1-5 counts/sec or about 10^{-3} counts/channel-sec. The additional intensity appearing as a higher background in the central part under the Rayleigh-Brillouin spectrum is due to

the anisotropic scattering contribution in the VV spectrum of toluene [see Eq. (3.4)] and is not a result of the instrumental background.

To fit the Rayleigh-Brillouin spectra, we used the simple form of Eq. (3.3) with only three adjustable parameters I_0, ω_B and Γ_B (with this definition, Γ_B is the full-width at half maximum of the Brillouin peak). A δ-function at zero frequency was added for the central Rayleigh peak and an additional constant background term was allowed to account for the broad anisotropic contribution. The theoretical spectrum constructed this way and numerically convolved with the instrumental function described above, yielded excellent fits to the experimental data. An example fit is shown in Fig. 5.1 with reduced $\chi^2 / DoF = 0.644$ (the raw $\chi^2 = 1755$ and degrees of freedom, DoF=2724). In most cases, for toluene the reduced χ^2 value was lower than 1.0 and for PEO and PEO/$LiClO_4$ was lower than 1.5 (in rare occasions up to 2.0, mainly due to the very strong central Rayleigh peak from the polymer melt which is typically 150-200 times stronger than the Brillouin peaks).

Fits were also attempted with the more complex forms of the spectrum such as Eq. (3.28) with memory function $m(\omega)$ as both Maxwell-Debye [Eq. (3.29)] and Cole-Davidson [Eq. (3.33)]. However, by introducing several additional fitting parameters these functions did not substantially improve the quality of the fit. On many occasions, especially at the high-temperature range, the fits became unstable due to the strong coupling between some of the parameters already mentioned in Section 3.4. This well recognized problem is broadly discussed in the literature.[29] A possible way around it is to have *a priori* knowledge of some of the parameter values such as ω_0, γ_0, β_{CD}, etc., or of the temperature behavior of $\tau(T)$. The literature values of β_{CD} are usually debatable and

they vary widely depending on the technique used in their determination. Furthermore, the determination of β_{CD} and τ and their temperature dependence is one of the objectives of this work; therefore we avoided making any *a priori* assumptions. The value of ω_0 is most commonly determined from an independent measurement (such as ultrasonic data) or is calculated using the thermodynamic relation $\omega_0 = q\sqrt{\gamma / \beta_T \rho}$ if the heat capacity ratio, γ, the isothermal compressibility, β_T, and the mass-density, ρ are known as a function of temperature. In addition, the refractive index $n(T)$ must be known since it determines the value of the scattering wavevector $q(T) = (4\pi n(T)/\lambda)\sin(\theta/2)$ as a function of temperature. There are several reasons we avoided "fixing" the parameter ω_0 in the manner described. Instead, it was used as a consistency check whenever it was possible (for example, in the q-dependent part of the experiment). The first argument is that the fits of the experimental spectra to Eq. (3.28) are very sensitive to the value of ω_0, therefore the uncertainties in the above quantities can bias the fits substantially. Another argument is that although there are good data in the case of toluene, in the case of PEO melt, the data were questionable due to the fact that the various quantities above had to be compiled from different sources which were inconsistent – the greatest discrepancy arising from the difference in the molecular weight of the polymer samples. In the case of PEO-melt/$LiClO_4$ electrolytes, most of the data simply did not exist.

To summarize the fitting procedure, for each experimental spectrum the instrumental function was fitted to the first and the last peaks in the spectrum, then the parameters for the instrumental function were fixed and the central Rayleigh-Brillouin spectrum was

fitted to the theoretical expression based on Eq. (3.3) convolved with the so determined instrumental function. Accordingly, the quantities determined from each spectrum were the Brillouin frequency, ω_B and linewidth, Γ_B. The data analysis was performed with self-written routines using Matlab. Some standard Matlab routines were incorporated, such as the numerical convolution [based on fast Fourier transformation (FFT)] and the nonlinear least-squares routine.

5.3. Error analysis

Some of the major contributions to the error bars of the main experimental quantities ω_B and Γ_B are summarized below.

1) The absolute frequency scale for the spectra is established through the relationship between the free spectral range (FSR) and the mirror spacing of the Fabry-Perot interferometer given by Eq. (2.6). The distance between the mirrors was calibrated by precision gauge blocks with two thicknesses $d = 6.620 \pm 0.001$ mm and $d = 6.000 \pm 0.001$ mm. In practice, the distance between the mirrors cannot be set with such precision since one has to be extremely careful not to scratch the reflecting surfaces. Nevertheless, the actual distance between the mirrors is within 10μm from the nominal value for the gauge blocks, resulting in about 0.15% error in *d*, which in turn results in about ± 0.04 GHz error bar in the frequency scale. Therefore, the resulting FSR is 22.66 ± 0.04 GHz or 25.00 ± 0.04 GHz respectively. The first value of the FSR was used in all temperature-dependent measurements of neat PEO melts and PEO-melt/$LiClO_4$ solutions, while the second value of the FSR was used in the toluene measurements as well as in the *q*-dependent measurements of PEO-melt/$LiClO_4$ solutions. This is the

major systematic error bar in the frequency scale and affects the accuracy of both the ω_B and Γ_B values.

2) The frequency resolution of the instrument imposes a limit on the smallest resolvable frequency difference between adjacent spectral peaks and is the major source of error in the determination of the spectral linewidths (through the deconvolution step), i.e. the error in Γ_B. There are three factors limiting the resolution:

- The instrumental resolution of the Fabry-Perot interferometer – it is estimated from the combination of the finesse and FSR, or even better, it is directly measured as the FWHM of the instrumental function. For the triple-pass interferometer used in all reported measurements the measured resolution was about 350 MHz or better (the experimental finesse was typically ~70 or better). It should be emphasized that the above linewidth (finesse) was measured for the same duration as for the typical data collection, therefore, it includes the effect of the small fluctuations of the interferometer during operation.

- The broadening due to the finite collection angle – the scattered light at the input of the detection fiber is collected from a finite range of scattering angles which depends on the detection optics used. In the case of a single-mode fiber, the relevant solid angle is equal to the divergence angle of the Gaussian beam defined by the fiber mode which is about 2.2 mrad (see Fig. 2.6). In the case of the 9.5 μm multimode fiber used in some of the measurements, the collection angle is the solid angle of the collecting microscope objective and it is calculated to be about 8.8 mrad. Even at the lowest angle used (30^o) this results in a less than 3% broadening of the instrumental lines for the multimode fiber

and less than 1% for the single-mode fiber. Therefore, this broadening is negligible in comparison to the interferometer resolution.

- Limitations on the resolution from digitizing the spectra – it was ensured the resolution was not considerably degraded by recording the spectra in data files with a limited number of channels. The number of channels of the MCS and the F-P range scanned resulted in about 15-20 MHz per channel resolution, which is about 20 times better than the limitation set by the interferometer itself.

Considering all of the above factors, the limiting frequency resolution is 0.35 GHz or better. Therefore, we only report results for well-resolved Brillouin peaks with $\omega_B \geq 2.0\,\mathrm{GHz}$ and $\Gamma_B \geq 0.6\,\mathrm{GHz}$. Peaks with smaller frequency shifts (which overlap with the wings of the central Rayleigh peak) or narrower linewidths did not always yield acceptable fits and their values were excluded.

3) Uncertainty in the absolute scattering angle – as it was mentioned in Sec. 2.3, the optical alignment procedure enables an estimate for the uncertainty in the scattering angle due to alignment of the center of rotation of the goniometer setup. It was found that an upper limit of this error is $\pm 0.05^{o}$. In addition, the nominal resolution of the stepper motor for the goniometer is 0.01^{o}. However, it was found that the angles are not reproducible to that accuracy and a more realistic estimate for longtime operation is reproducibility within $\pm 0.05^{o}$. Combining these two independent errors in quadrature results in an error bar of $\pm 0.07^{o}$ (or ±1.23 mrad) in the value of the scattering angle. This error was ignored since it introduces only insignificant error in the experimental values of ω_B and Γ_B.

4) Temperature uncertainty and fluctuations

- As it was mentioned in the description of the experimental setup, the accuracy of the set temperature of the sample was $\pm 0.5\,^{o}$C and during the measurement it was kept stable within $\pm 0.1\,^{o}$C for the goniometer setup and $\pm 0.05\,^{o}$C for the high-temperature cell. In the temperature range of maximum dispersion of ω_B (strongest temperature dependence of ω_B) it has a slope of 0.033 GHz per 1^{o}C, which makes the maximum error in the value of ω_B due to temperature fluctuations less than 0.1%.

- It was observed that fluctuations in the room temperature affected the experimental values of ω_B and Γ_B mainly through its effect on the interferometer, which although passively well isolated from the room, did not have an active temperature stabilization control. More specifically, there are systematic variations by as much as 3^{o}C in the room for the duration of the day which showed noticeable but very reproducible effect on the values of ω_B and Γ_B, evident as a smooth trend from the morning to the afternoon measurements. Due to the reproducibility of the effect and its slow variation during the day, for each reported data point multiple measurements were performed, at different times of the day, which allowed to effectively cancel the effect of the room variations. Most of the reported data represent an average of three measurements done on different days and at different times of the day, with some of the key measurements (such as the 90^{o} and the 160^{o} scattering angles) repeated up to six times. The residual scatter in the data was within the overall error bar (cited below) and appeared random in nature.

5) Counting statistics and fitting of the spectra – the signal is collected by a photomultiplier tube (PMT) in a photon counting mode at low counting rates and very low dark count rate (typically ~ 1-5 counts/sec). Therefore, standard counting (Poisson)

statistics apply with an error bar $\pm\sqrt{N}$, where N is the number of counts in a channel and the fitting procedure uses $1/N$ weighting for the data points.

Considering all of the above factors we assigned an error bar due to random errors of $\pm 0.04\,\mathrm{GHz}$ in the value of ω_B and $\pm 0.08\,\mathrm{GHz}$ in the value of Γ_B. In addition, there is the systematic error bar of $\pm 0.04\,\mathrm{GHz}$ in the absolute frequency scale due to the calibration of the interferometer as discussed in "1)" above, which can only amount to a constant shift of the frequency scale for all data.

CHAPTER 6

RESULTS AND DISCUSSION

6.1. Results for PEO melt and PEO-melt/$LiClO_4$ – temperature dependence

Several representative Rayleigh-Brillouin spectra obtained from neat PEO-1K melts at different temperatures are shown in Fig. 6.1. The solid lines represent the best fit to the experimental spectra. The central Rayleigh line is very strong, which is typical for the

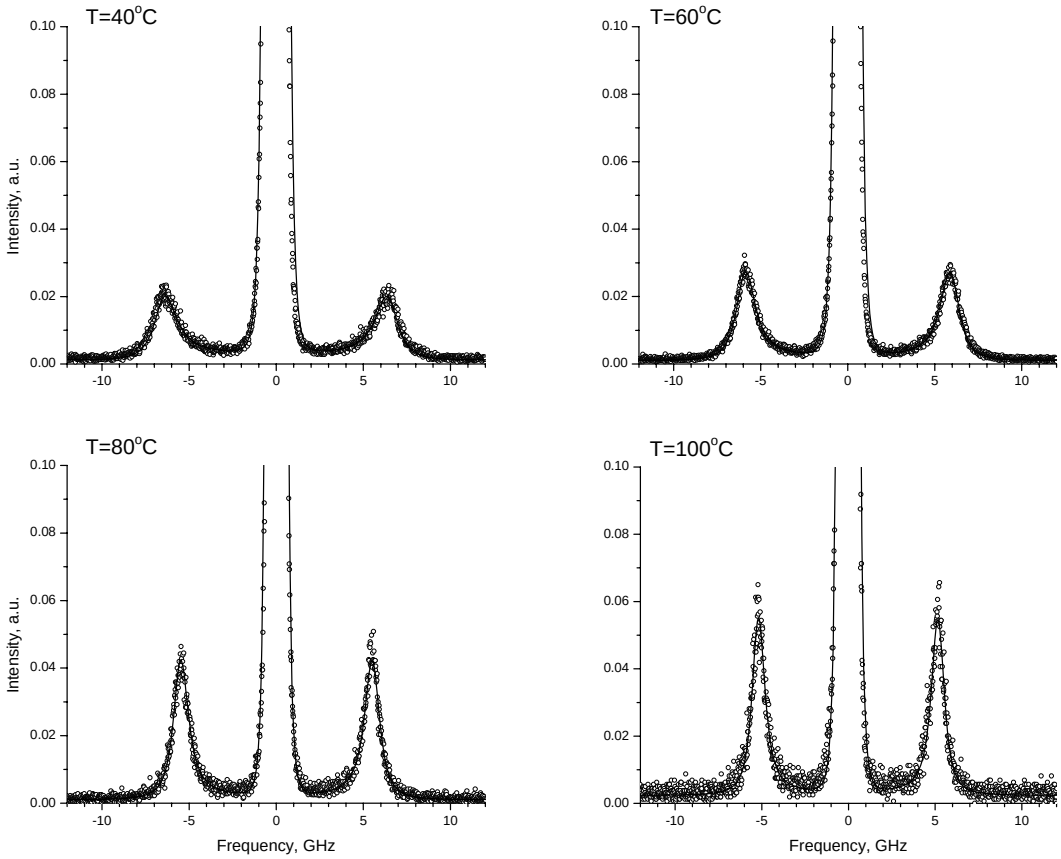

Fig. 6.1 – Rayleigh-Brillouin spectra of PEO-1K melt at different temperatures

light-scattering spectrum of polymer melts. Nevertheless, due to the triple-pass operation of the Fabry-Perot interferometer, the wings of the strong Rayleigh line are substantially suppressed and the Brillouin peaks are very well resolved. The relaxation behavior in the system is evidenced by the change in the Brillouin frequency and linewidth at different temperatures. With increasing temperature, the frequency shift becomes smaller and the width of the peaks becomes narrower.

The temperature dependence of the parameters ω_B and Γ_B for neat PEO-1K melt is shown in Fig. 6.2. The solid lines shown in the graphs are fits of the experimental data to the following expressions

$$\omega_B = \omega_0 \left[1 + \frac{1}{2} \frac{\Delta^2 \tau^2}{1 + \omega_0^2 \tau^2} \right], \tag{6.1}$$

$$\Gamma_B = \gamma_0 + \frac{\Delta^2 \tau}{1 + \omega_0^2 \tau^2}, \tag{6.2}$$

which are approximations of Eqs. (3.34) and (3.35) in the case of a single-exponential

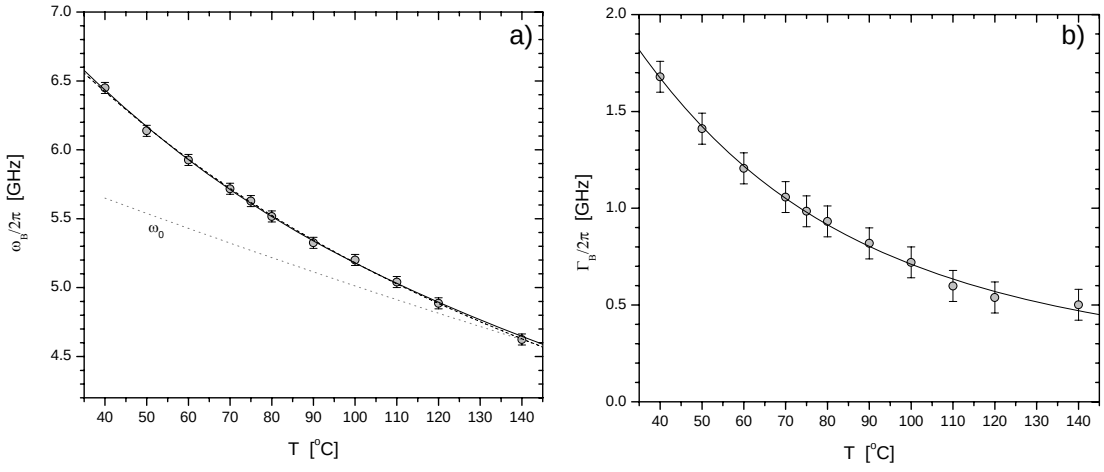

Fig. 6.2 – Brillouin frequency shift and linewidth as a function of temperature for neat PEO-1K melt

relaxation with relaxation time, τ. Furthermore, an Arrhenius temperature behavior is assumed for τ [Eq. (3.36)]. The values for $\omega_0(T)$, used in the fit and shown as the dotted line in Fig. 6.2-a, are obtained from the thermodynamic relation $\omega_0 = q\sqrt{\gamma / \beta_T \rho}$, where the values of the thermodynamic quantities based on equation of state data for PEO are:

$$\rho(T) = 1.142 \exp(-7.087 \times 10^{-4} \times T),$$

$$\beta_T = \frac{0.0894}{2077} \exp(0.003947 \times T),$$

$$\gamma = C_p / (C_p - \alpha^2 T / \rho \beta_T),$$

where the values of $\alpha(T)$ and C_p were taken from the literature.[71,72,73,74] The parametric expressions above are calculated per gram substance and the temperature is in K. Subsequently, all quantities were converted to SI units.

These results showed that the peak of the relaxation (the maximum in the linewidth, Γ_B) is below 40°C, which is the lower temperature limit accessible in the neat PEO-1K melt. The fits are very sensitive to the functions chosen for $\omega_0(T)$ and $\gamma_0(T)$. While the above thermodynamic relations provide some information about the function $\omega_0(T)$, the parameters from the literature are a compilation of data for polymer samples tested in different laboratories, originating from different suppliers and, in general, with different molecular weights. Therefore, the temperature dependence was retained, but a shift by a constant factor between the relative positions of $\omega_0(T)$ and $\omega_B(T)$ was allowed, which amounts to a vertical shift of $\omega_0(T)$ of about 5% of its value. This shift is justified by the uncertainties in the calculated values for $\omega_0(T)$ from the above parameters, as well as the uncertainty of the absolute frequency scale in the present measurement, which can result

in a systematic shift of $\omega_B(T)$. While a reasonable estimate for $\omega_0(T)$ was possible, no literature information about $\Delta(T)$ and $\gamma_0(T)$ could be found. In order to keep the number of fitting parameters as low as possible, constants were chosen for both parameters. The best fit shown in Fig. 6.2-b is obtained with $\Delta/2\pi = 5.4$ GHz and $\gamma_0/2\pi = 0.095$ GHz. Considering all of the above, any results for τ and E_a from such fits should be used with caution. Nevertheless, the values obtained from the fit to $\omega_B(T)$, were very consistent with values obtained from fitting individual spectra at different temperatures to Eq. (3.28) with a single exponential form for $m(\omega)$ (Fig. 6.3). As discussed above, these fits tend to be very unstable due to strong coupling between some of the fitting parameters. Consequently, values of τ for some of the temperatures in the range, for which the fits

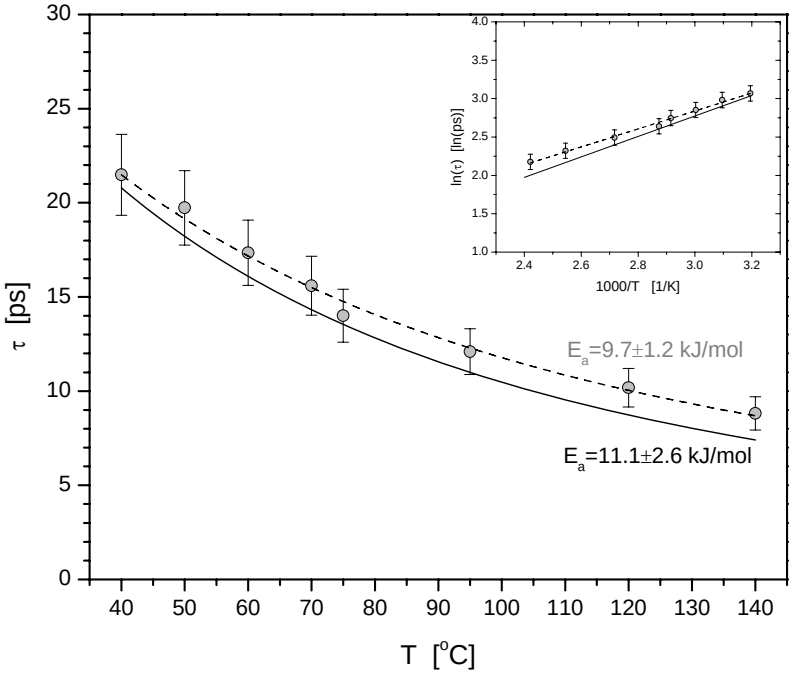

Fig. 6.3 – Temperature dependence of the relaxation time for PEO-1K melt.
The dashed line is a fit to the data points, while the solid line is from the best fit in Fig. 6.2-a.

were not stable had to be omitted. The values of τ from this procedure, which resulted from satisfactory fits, are represented by the data points in Fig. 6.3. The dashed line in the figure is an Arrhenius fit to the data points, which yielded an activation energy of $E_a = 9.7 \pm 1.2$ kJ/mol. The solid line below the data points is the Arrhenius equation plotted with parameters from the best fit to $\omega_B(T)$ (solid line in Fig. 6.2-a) with activation energy $E_a = 11.1 \pm 2.6$ kJ/mol. The two values for the activation energy of τ are consistent within the error bars. Although there is a slight discrepancy between the two Arrhenius laws, the agreement is remarkable considering all the uncertainties described above. The inset in Fig. 6.3 shows the temperature dependence in a typical Arrhenius plot of $\ln\tau$ vs. $1/T$. Further argument that the two Arrhenius laws are consistent is also the fact that the fits with both functions for $\tau(T)$ are overlapping almost exactly (solid and dashed lines in Fig. 6.2-a), with insignificant difference in the χ^2 values. Finally, it is noted that the characteristic time for the relaxation is about 9 ps at the high-temperature range. Upon cooling, it slows down to about 22 ps at temperature close to the melting point of the polymer.

The temperature dependence of the parameters $\omega_B(T)$ and $\Gamma_B(T)$ was also studied for several different salt concentrations of the PEO-melt/$LiClO_4$ electrolyte. The results are summarized in Fig. 6.4. For a given temperature, the value of ω_B increases significantly with increasing salt concentration. We note that the adiabatic sound speed in the medium, v_s, is directly proportional to ω_B and the elastic part of the adiabatic longitudinal modulus, M', is proportional to ω_B^2, i.e.

$$v_s = \frac{1}{q}\omega_B \tag{6.3}$$

$$M' = \frac{\rho}{q^2}\omega_B^2 . \tag{6.4}$$

Therefore, the sound speed and the elastic modulus in the medium increase with increasing salt concentration. To illustrate this increase, in Fig. 6.5 the value of ω_B^2, which is proportional to the elastic modulus, M', is plotted as a function of salt concentration for several representative temperatures. The increase is attributed to the increased concentration of the dissociated Li^+ ions, which in turn results in an increase of the density of the transient physical crosslinks due to lithium-oxygen interactions. Increased elasticity of the medium has significant implications for the performance of the system as an electrolyte. As mentioned previously, the charge transport in the electrolyte is closely related to the polymer chain mobility. Since the Li^+ ions are preferentially coordinated by several PEO ether oxygens, they act as additional tie points in the network

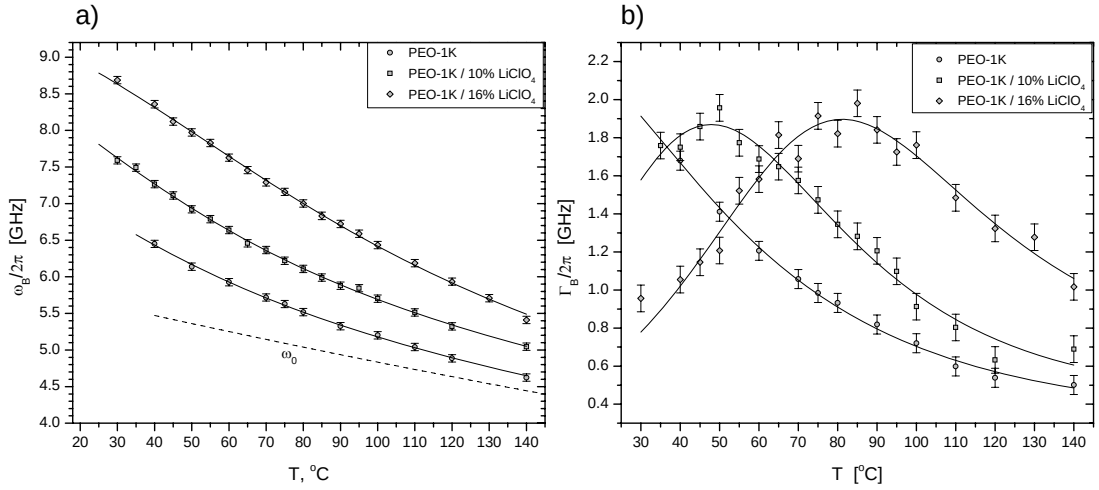

Fig. 6.4 – Brillouin frequency shift and linewidth as a function of $LiClO_4$ concentration and temperature

structure formed in the melt and as such are restricted in their motions by the mobility of the surrounding segments of the polymer chains. They can effectively diffuse through the medium when assisted by local motions of the polymer. The increased elasticity, in effect, results in a stiffer network structure, which in turn results in reduced ion mobility. This experimental result is consistent with our earlier results[7,8] from a PCS study of the PEO-melt/$LiClO_4$ system, where the observations on a very different timescale were also interpreted in terms of consolidation and stiffening of the transient network with increasing salt concentration. It is also consistent with the findings by Torell *et al.*[11,12] in similar electrolytes consisting of poly(propylene glycol) complexed with lithium and sodium salts. Qualitatively, the present result confirms the expectation derived from the

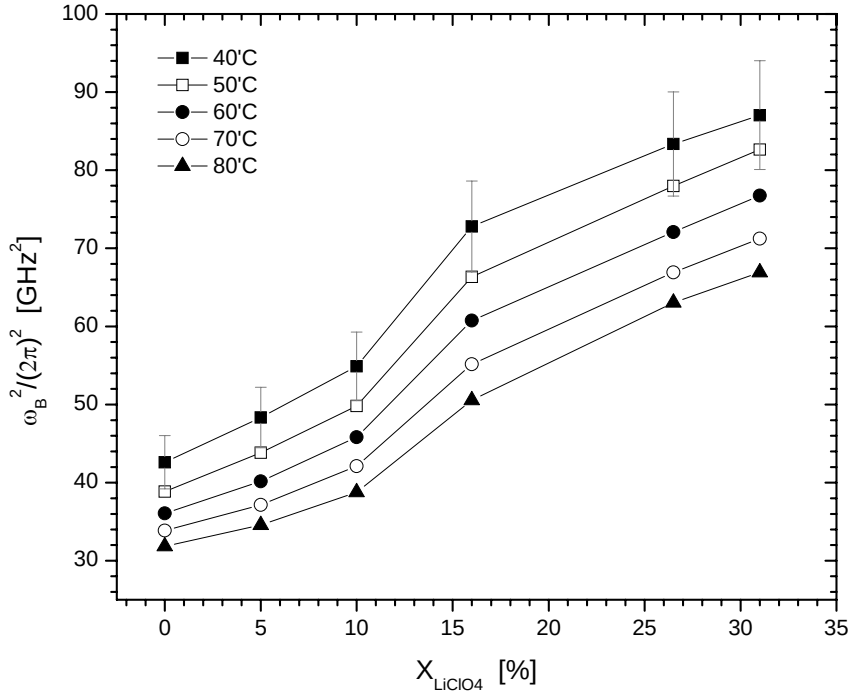

Fig. 6.5 – Behavior of the adiabatic longitudinal elastic modulus, $M' \sim \omega_B^2$ as a function of $LiClO_4$ concentration and temperature. The error bars are shown only on the 40^{o}C data set for clarity.

conductivity plots (Fig. 4.2) that, at salt concentrations higher than few percent, the major factor suppressing the conductivity of the electrolyte is the reduced Li^+ cation mobility. In addition, it provides a quantitative measure of the elastic modulus as a function of temperature and salt concentration, which might prove useful in modeling the behavior of the conductivity as a function of these parameters.

Returning now to the discussion of the results shown in Fig. 6.4 it is evident, especially in the plot for $\Gamma_B(T)$ (Fig. 6.4-b), that with increasing salt concentration, the relaxation process occurs at higher temperatures. The peak of the sound attenuation (which is proportional to Γ_B) moves from temperatures below the melting point* of the polymer electrolyte, to higher temperatures inside the experimental window. According to the dielectric relaxation map of PEO, shown in Fig. 4.3, in this temperature-frequency region, one expects to find the glass-rubber α_a- relaxation, which has merged with the lower temperature β_a- relaxation. It is significant that the calorimetric glass transition (Fig. 6.6) also moves to higher temperatures with increasing salt concentration.[75,76] This supports the argument that the observed relaxation is indeed the glass-rubber relaxation, which is often referred to as the "dynamic glass transition". At zero frequency, it extrapolates to the static glass transition temperature (see Fig. 4.3) and it is believed that the properties of both the static and the dynamic glass transitions, including their concentration dependence, are closely related. For the above reasons, this relaxation observed in pure PEO melt[68] and in similar experiments with PPO and PPO-salt electrolytes[11,12] was identified with the dielectric glass-rubber relaxation.

* The melting point of the PEO/$LiClO_4$ complex shifts slightly to lower temperatures (by about 5°C), with increasing salt concentration up to the eutectic point ($LiClO_4$ ~18-19 wt.-%) in the phase diagram of the system [see Ref. 2].

Here several reasons support the idea that the relaxation observed in the temperature dependence of the parameters ω_B and Γ_B for both the neat PEO-1K melt and the PEO-melt/$LiClO_4$ solutions, in fact, results from at least two underlying β-relaxations. Although they are not resolved in the temperature-dependent experiment, they were resolved in the frequency-dependent experiment in the case of 5wt.-% $LiClO_4$ solution (see below), which is in agreement with a result from recent QENS and NSES experiments.[69,70] According to the authors of these experiments, evidence of the slower α-process was observed at characteristic times longer than 100 ps (frequencies below 1.5 GHz), which is barely outside of the current experimental range for our F-P setup.

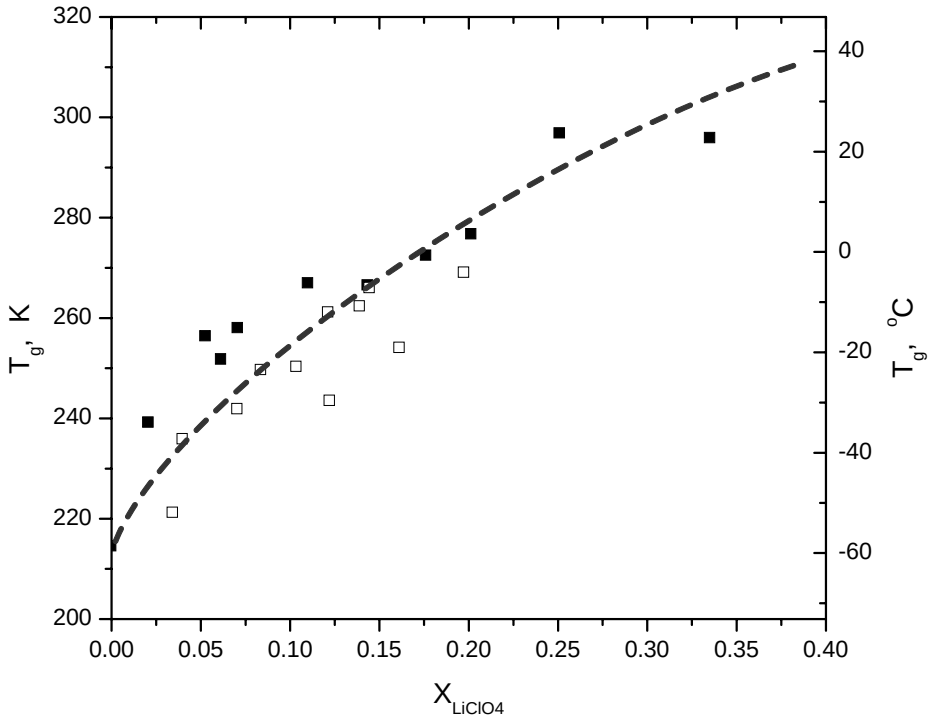

Fig. 6.6 – Glass-transition temperature as a function of salt concentration. Filled symbols from Ref. 77 and open symbols from Ref. 78; the dashed line is only a guide for the eye.

The facts that the relaxation time $\tau(T)$ shows Arrhenius temperature dependence, instead of VTF and the stretching parameter was determined to be $\beta = 1$, offer strong support for the argument that the relaxation observed in the present experiment has the character of a secondary β-relaxation.

Another important consequence of the analysis of the data in Fig. 6.4 is the behavior of the relaxation time as a function of salt concentration. In Fig. 6.7 we show Arrhenius plots of the relaxation time for neat PEO-1K melt, as well as for PEO-melt/$LiClO_4$ electrolytes with 10% and 16% salt content. These functions are extracted from the best-fit results in Fig. 6.4-b. The analysis is limited to the qualitative features, with the reminder of the possible ambiguity of the absolute values for τ and E_a due to the lack of

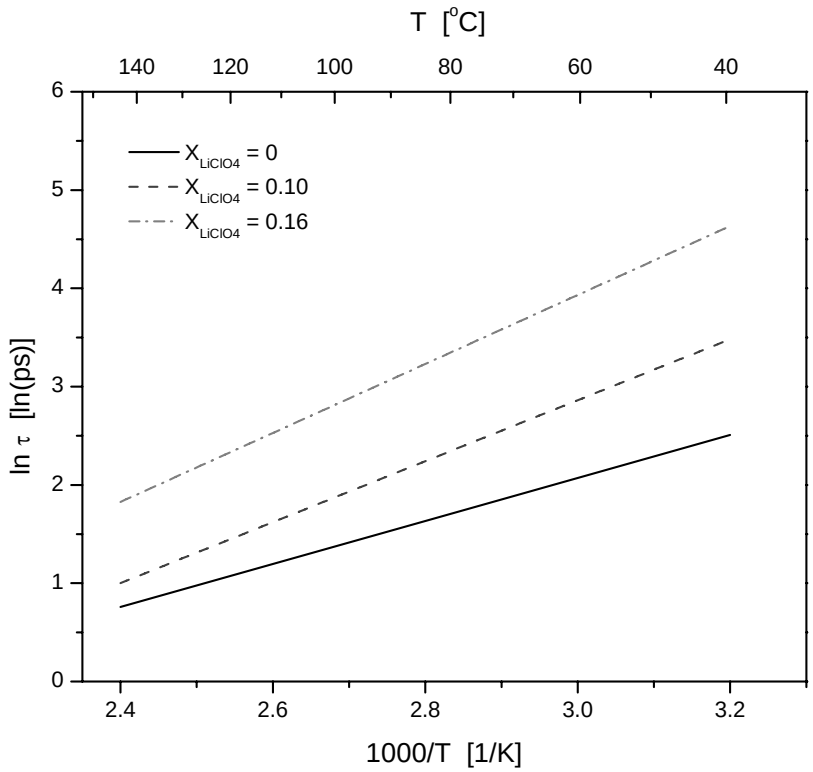

Fig. 6.7 – Arrhenius behavior of the relaxation time for different salt concentrations. The lines represent the Arrhenius equation with parameters from the fits in Fig. 6.4

any independent reference data for the two electrolytes. Nevertheless, the graph suggests that by increasing the salt content in the electrolyte the characteristic time of the process slows down. This effect is more pronounced at lower temperatures and with increasing temperature the Arrhenius laws for the two electrolytes (broken lines) seem to converge back towards the neat polymer melt values (solid line). This is consistent with the interpretation emerging from this and other experiments and computer simulations (see below) showing that with increasing temperature, the complexation of lithium ions by ether oxygens is significantly reduced at the expense of increased anion-cation recombinations, which results in an overall reduced effect of the salt on the polymer network at higher temperatures.

6.2. Frequency dependence of ω_B and Γ_B

As noted in the preceding chapters, the relaxation process discussed above can be investigated in much more detail if the parameters ω_B and Γ_B are studied as a function of frequency. An obvious advantage of this approach is the fact that for a fixed temperature, instead of a single data point, as in the traditional temperature-dependence method (above), data may be collected for $\omega_B(\omega)$ and $\Gamma_B(\omega)$ in a range of frequencies between approximately 2 and 10 GHz. Although this range is rather modest in comparison to other techniques, it proved useful in resolving the two-step relaxation in the PEO-melt/$LiClO_4$ system. Furthermore, the frequency range can, in principle, be extended by using tandem Fabry-Perot interferometers and/or including some form of heterodyne detection in the experimental system. The fiber-optic detection approach developed in the present effort makes such an extension trivial. Another significant advantage is that the functions

$\omega_B(\omega)$ and $\Gamma_B(\omega)$ are analyzed at fixed temperature, and therefore all the fitting parameters are now constants as opposed to unknown functions of temperature hence eliminating all the guesswork required otherwise.

The frequency-dependent measurements are made by changing the scattering wavevector, **q,** of the detected light by varying the scattering angle, θ. Indeed, by changing **q**, different wavelengths and therefore different frequency components of the thermally excited acoustic waves in the sample are probed. At given scattering angle, θ, the values obtained experimentally are ω_θ and Γ_θ. In order to remove the explicit q-dependence in these quantities* and to facilitate the comparison with 90° scattering angle data (such as the data reported earlier in this chapter), the quantities

$$\omega_{90} = \frac{q_{90^\circ}}{q_\theta}\omega_\theta \quad \text{and} \quad \Gamma_{90} = \frac{q_{90^\circ}^2}{q_\theta^2}\Gamma_\theta$$

were formed, where q_θ is the scattering wavevector at angle θ and q_{90° is the scattering wavevector at angle $\theta = 90^\circ$ [using Eq. (2.17)]. The quantities ω_{90} and Γ_{90}, which can be understood as the "equivalent Brillouin frequency and linewidth at 90° scattering angle", are directly proportional to the traditional adiabatic sound velocity, v_s, and loss modulus, M'', respectively. Since the fractional error bars on the two quantities should be preserved (the uncertainty in the value of q is negligible), the absolute error bar scales with the angle, the same way the main quantities do. As a result, the uncertainties at the lower scattering angles are much larger than the uncertainties in the higher angles.

---

* If one considers the parameters in Eqs. (3.46) and (3.47) with $m(\omega)$ given by any of the functional forms described in the text, ω_0 and Δ are q-dependent, and γ_0 is q^2-dependent. Therefore, ω_B is q-dependent and Γ_B is q^2-dependent.

In order to check the validity of the method, a series of measurements using toluene as the scattering medium were performed, for which there is an abundance of information in the literature. Several spectra at representative scattering angles are shown in Fig. 6.8. The fits to the spectra, as well as the reduced χ^2 values are also included in the plots.

Although toluene has been studied extensively using Brillouin light-scattering techniques,[49,77,78] there are no measurements to date offering the kind of frequency resolution available in the present experiment. Relaxation processes (α and β) in the gigahertz frequency range in toluene are observed at temperatures way below 20°C, which is the lower-temperature limit in the present light-scattering setup. Although, in principle, they can be studied by the angle-dependence technique, they were outside our present experimental capabilities. The data collected from toluene for $\omega_{90}(\omega)$ and $\Gamma_{90}(\omega)$

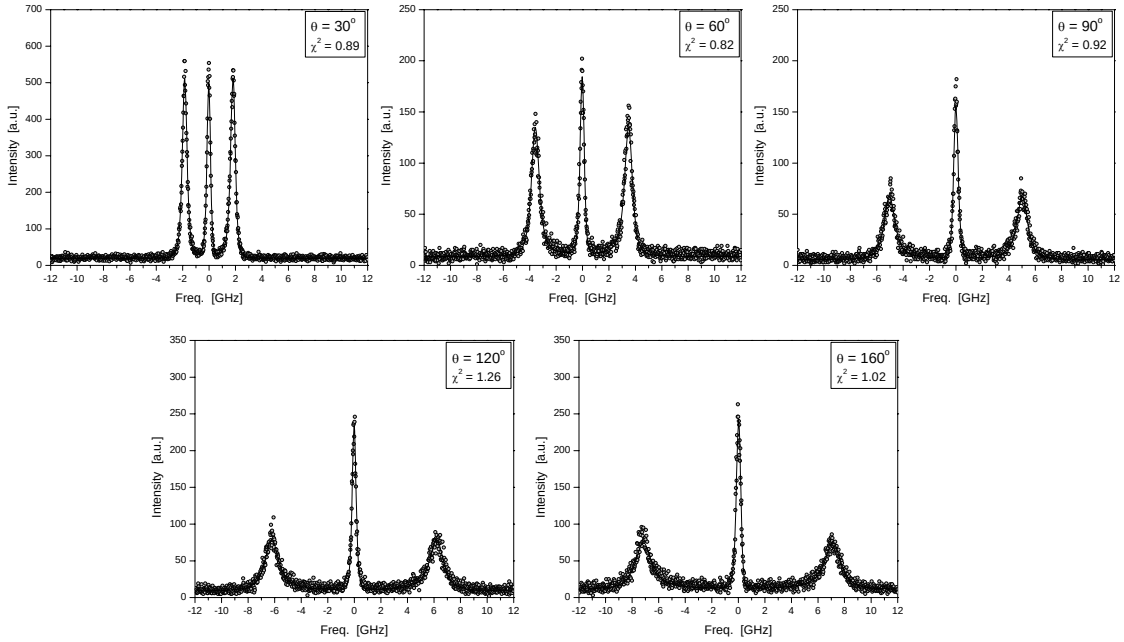

Fig. 6.8 – Rayleigh-Brillouin spectra for toluene at 50°C and different scattering angles

are presented in Fig. 6.9. For clarity, the error bars are shown only in few data points at the highest temperature data set (50°C).

In Fig. 6.9-a, the experimental data for $\omega_{90}(\omega)$ were fit to Eq. (3.46). The open symbols at zero frequency are calculated values for $\omega_0 = q\sqrt{\gamma/\beta_T\rho}$, with the parameters for toluene found in the literature.[77] These points were excluded while performing the fit. Fits with all forms of $m(\omega)$ described in the earlier chapters, i.e. Cole-Davidson, Cole-Cole and KWW (via numerical Laplace transformation in frequency space) were attempted. It was found that the best fits to the data are consistent with a stretching parameter $\beta = 1$, i.e. a Maxwell-Debye single-exponential relaxation. For the relaxation time, it was found $\tau \approx 18$ ps and for the relaxation strength, $\Delta/2\pi = 2.7$ GHz. These values are in agreement with the ones reported in a recent Brillouin light-scattering study of toluene.[77] There was no detectable temperature dependence for τ, which was expected since the experiment spans a relatively narrow temperature range and does not include

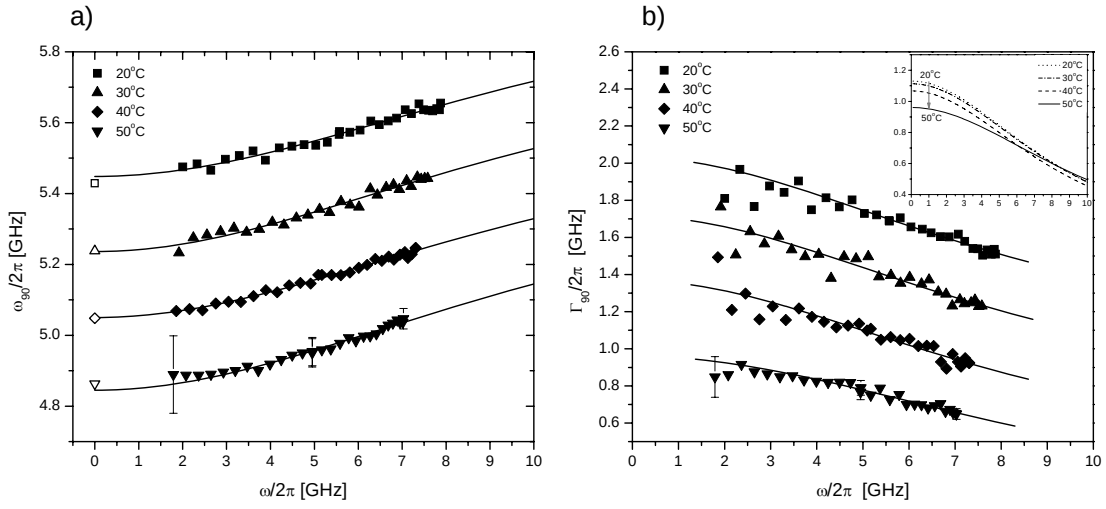

Fig. 6.9 – Brillouin frequency-shift and linewidth as a function of frequency for toluene

the center of the relaxation. The result of an old experiment[49] which reports a two-step relaxation process were not confirmed. On the other hand, recently performed polarized and depolarized light-scattering experiments[77,78] do not give any indications of a relaxation process in the temperature range studied in the present work.

The experimental data for $\Gamma_{90}(\omega)$ are shown in Fig. 6.9-b. Since the data sets at different temperatures were overlapping, for clarity the data for 40°C, 30°C and 20°C were shifted vertically by 0.3, 0.6 and 0.9 GHz, respectively, along with the corresponding fits to Eq.(3.35). The data points and the fit for the 50°C data set are not shifted. To facilitate comparison between the different temperatures, the unshifted fits without the data points are plotted in the inset of the figure.

The Brillouin frequency shift and linewidth were measured for the 5%-salt, PEO-melt/$LiClO_4$ sample, as a function of frequency and temperature. The results for $\omega_{90}(\omega)$ along with the best fits to Eq. (3.46) are summarized in Fig. 6.10-a, and the results for $\omega\Gamma_{90}(\omega)$ with fits to Eq. (3.47) are summarized in Fig. 6.10-b. The striking feature evident in the graphs is the two-step relaxation process, which is more apparent at the lower temperatures. In fact, the attempts to fit the data sets with single exponential relaxation did not produce satisfactory fits. Once it was established that a two-process function for $m(\omega)$ is required, we attempted using combinations of different relaxation functions, including Cole-Davidson, Cole-Cole and Laplace transform of KWW. In all cases, the fits converged robustly to values of $\beta = 1$, indicating that both underlying relaxations are best fit by a Maxwell-Debye single-exponential relaxation functions. This was clearly the case when both $\omega_{90}(\omega)$ and $\omega\Gamma_{90}(\omega)$ were analyzed. Therefore, the form of $m(\omega)$ used to fit the data is given by the following expressions:

$$m'(\omega) = -\Delta_1^2 \frac{\omega\tau_1^2}{1+\omega^2\tau_1^2} - \Delta_2^2 \frac{\omega\tau_2^2}{1+(\omega-\omega_2)^2\tau_2^2}, \tag{6.5}$$

$$m''(\omega) = \Delta_1^2 \frac{\tau_1}{1+\omega^2\tau_1^2} + \Delta_2^2 \frac{\tau_2}{1+(\omega-\omega_2)^2\tau_2^2}, \tag{6.6}$$

where Δ_1 and τ_1 are the relaxation strength and time for the first process (slow), and Δ_2 and τ_2 are the relaxation strength and time for the second process (fast), respectively. The parameter ω_2 is necessary to account for the relative frequency shift between the centers of the two relaxations.

The relaxation strength parameters extracted from the fits described above are summarized in Fig. 6.11. The lines in all the panels are to guide the eye. The relaxation strengths for both relaxations, Δ_1 and Δ_2, the total relaxation strength, $\Delta = \left(\Delta_1^2 + \Delta_2^2\right)^{1/2}$, and the zero-frequency limiting value ω_0, are all monotonically decreasing with increasing temperature. The lower-frequency relaxation is stronger than the higher-frequency one. The relative strengths of the relaxations are easily compared in

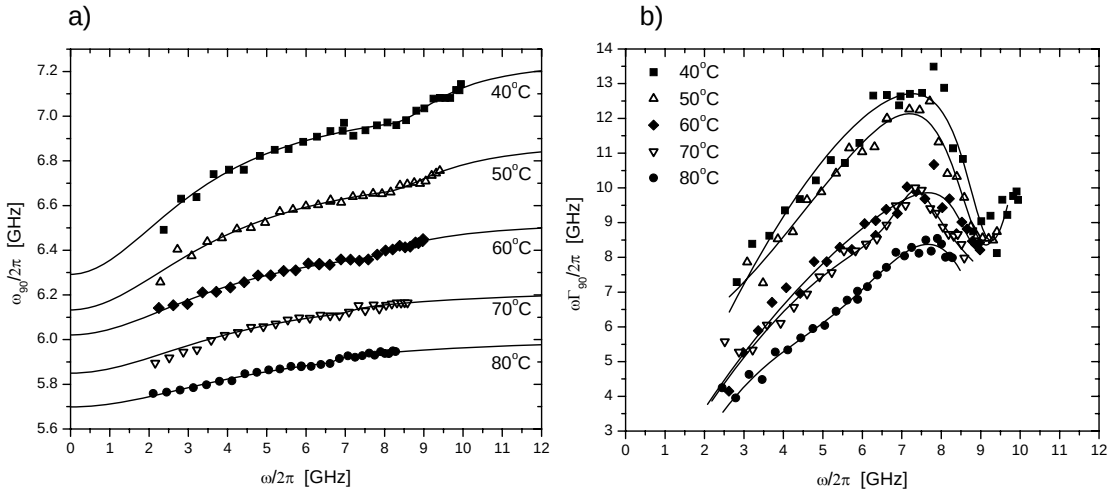

Fig. 6.10 – Brillouin frequency-shift and linewidth as a function of temperature for 5wt.-% PEO-melt/LiClO4 solution

Fig. 6.11-d, where the values of ω_0, $\omega_\infty = \left(\omega_0^2 + \Delta^2\right)^{1/2}$, and the intermediate limit $\omega_1 = \left(\omega_0^2 + \Delta_1^2\right)^{1/2}$ are shown. Starting at the high-temperature limit, the Brillouin frequency shift, ω_B will be close to its thermodynamic or "zero-frequency" limit, ω_0. With decreasing temperature, ω_B will first undergo dispersion to the intermediate limiting value, ω_1, due to the first relaxation process. When the temperature is further reduced, ω_B undergoes additional dispersion to its high-frequency limiting value, ω_∞.

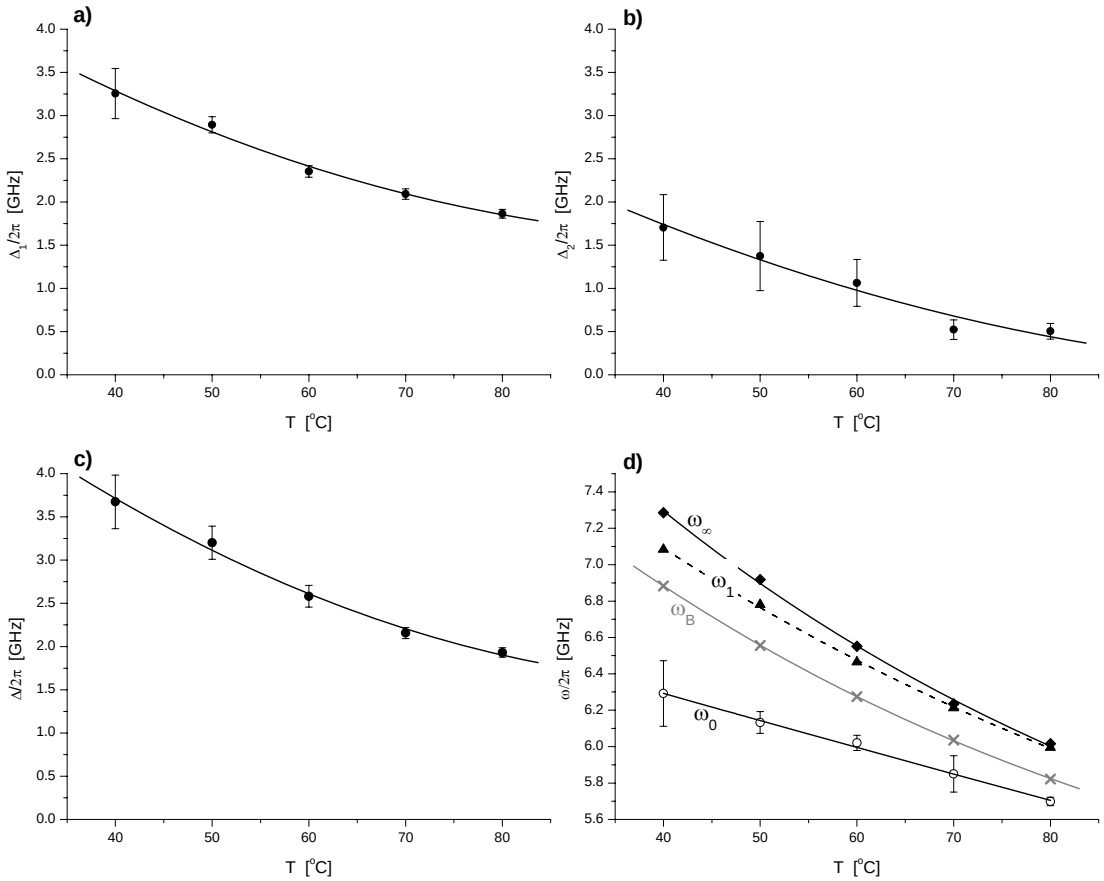

Fig. 6.11 – Relaxation strength parameters for the 5wt.-% PEO-melt/$LiClO_4$ electrolyte. a) lower-frequency, and b) higher-frequency relaxation strength; c) total relaxation strength $\Delta = (\Delta_1^2 + \Delta_2^2)^{1/2}$; d) two-step dispersion in the Brillouin frequency shift.

Strictly speaking, it is possible that there are other relaxations at frequencies below and/or above our experimental window. In fact, it is highly likely that the α_a relaxation is present at frequencies below 1.5 GHz, as mentioned above, although it cannot be detected in the experiment described here. Therefore, the values of ω_0 are not the true "zero-frequency" values but rather, the high-frequency limit of the preceding relaxation process. The same can be said for the values of ω_∞, which can be the considered as a "low-frequency limit" for yet another, faster process, active at frequencies higher than the range probed experimentally here (if such a process exists).

The values of ω_B measured directly are also included in the plot and represented by the crossed symbols (the line through the data points is a fit as in Fig. 6.4-a). It can be concluded that, in general, the behavior of $\omega_B(T)$ is consistent with the two-step relaxation scenario, described above. However, it is obvious that from the temperature dependence of the 90^o scattering angle data alone, it is not possible to extract any information about the two separate underlying relaxations. If this was the single available measurement, it can only be concluded that the dispersion in $\omega_B(T)$ results from a single relaxation, which may or may not appear broader than a Maxwell-Debye relaxation. Resolving the details of the two relaxations is possible solely due to the ability to perform angle-dependent measurements.

The temperature dependence of the relaxation times for both relaxations is shown as an Arrhenius plot in Fig. 6.12. The characteristic time for the slower relaxation, τ_1 decreases with increasing temperature from about 45.3 ps at 40^{o}C to about 33.5 ps at 80^{o}C. The activation energy for the process, extracted from the Arrhenius plot is

$E_a = 6.23$ kJ/mol. While the slower process (filled squares) shows the usual behavior of slowing down of the dynamics with decreasing temperature, the faster process (open diamonds) with characteristic time τ_2 shows a somewhat unexpected trend of slowing down with increasing temperature. The relaxation time for the faster process increases from about 16.5 ps at 40°C to about 23.5 ps at 80°C. Although, a possible mechanism resulting in such atypical temperature behavior is proposed in the discussion section below, a fit to the data set was not attempted since there is currently no conclusive model explaining the unusual behavior.

As is evident in Fig. 6.12, at higher temperatures the two relaxations move closer

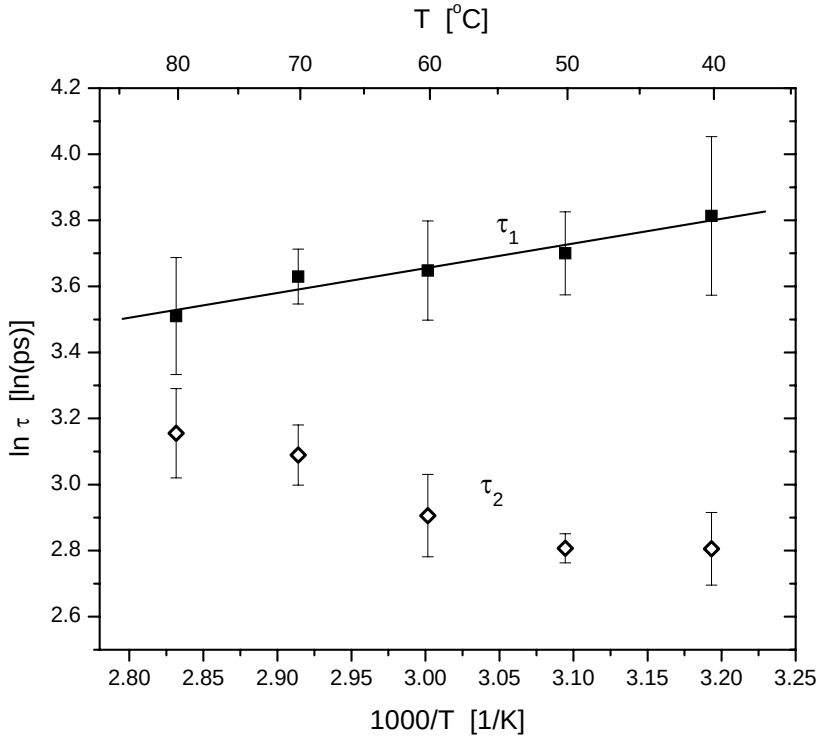

Fig. 6.12 – Temperature dependence of the characteristic relaxation time for the 5wt.-% PEO-melt/$LiClO_4$ solution. The slower process, τ_1, follows Arrhenius temperature dependence (solid line), while the faster process, τ_2, cannot be explained by an Arrhenius law.

together and the higher-frequency one becomes considerably weaker (see also Fig. 6.11). In the neutron scattering study by Mao, *et al.*,[69] a single relaxation was observed in the case of the PEO-melt/$LiClO_4$ electrolyte and two relaxations were observed in the case of the PEO-melt/LiTFSI electrolyte (with $T=75^oC$ and EO:Li=7.5:1 salt concentration for both electrolytes). The relaxation time reported in their experiment for the $LiClO_4$ electrolyte is $\tau_{QENS} \approx 25$ ps, and the stretching parameter is $\beta_{QENS} = 1$. At the same temperature, but much lower salt concentration (EO:Li=46:1), we find $\beta = 1$ and $\tau_1 \approx 35$ ps, and $\tau_2 \approx 22$ ps, respectively for the two relaxations. The apparent agreement between the two experiments suggests that in both cases the same underlying phenomena are observed. At this higher temperature, the two relaxations resolved in the Brillouin scattering experiment are almost entirely overlapping and this may be the reason they were not resolved in the QENS study.

6.3. Discussion of the experimental results

The nature of the observed relaxations and their implications for the polymer chain and Li^+ mobility in the polymer electrolyte are among the most important problems before this study. In order to identify the relaxation processes, the magnitude of the characteristic times typically observed in PEO-melt/Li-salt polymer electrolytes are considered. The Li^+ diffusion constant is typically $\sim 2\times10^{-7}$ cm^2/s at 400K.[4] Together with the distance between neighboring ether oxygens of ~3Å, this diffusion constant implies a characteristic jump time of the order of a few nanoseconds. It was determined by computer simulations[79] (for a PEO-melt/LiI complex, and for similar temperatures and salt concentrations) that the average lifetime of the transient EO–Li^+ bond is on the order

of at least 400 ps or longer. Therefore, the processes of transient-link formation and breakage are too slow to have an effect on the dynamics observed in our experimental range. On the other hand, according to the same study, the characteristic relaxation times for the dihedral angle dynamics in the neat melt are on the order of 5-20 ps. For the 5%-salt electrolytes, only about 10% of the dihedrals are complexed with a Li^+ cation and about 90% are uncomplexed.* While the relaxation time for the complexed dihedrals is slowed down considerably compared to the pure melt to about 175-180 ps at 90°C, it is relatively unchanged for the uncomplexed dihedrals (5-24 ps). This dramatic slowdown of the characteristic time affects the collective α-relaxation mode which involves translational diffusion of the chain segments on a larger length-scale and inevitably involves complexed dihedrals. The results from the QENS and NSES experiments mentioned above[69,70] confirm that with increasing salt concentration, this mode becomes slower than 100 ps, and therefore is outside our experimental window. Another strong argument that the observed relaxations in the present study cannot be identified with the α-relaxation mode is the value of β. While it has been observed by several experimental[59,69] and computational techniques[79] that typical values for the α-relaxation in PEO melts and low-concentration PEO-melt/LiClO4 electrolytes are on the order of $\beta \sim 0.5-0.6$, in the present work it is found that $\beta = 1$ for both relaxations. In addition, the temperature dependence of the relaxation time for the α-relaxations typically follows VTF behavior, in contrast with the Arrhenius behavior observed here, which is characteristic for β-relaxations. All of the above arguments strongly suggest that the

* A dihedral is considered complexed when a Li^+ cation is found in the first coordination shell of an ether oxygen, i.e., within 4.0Å from an ether oxygen belonging to the dihedral.

relaxations observed in Fig. 6.10 are not α-relaxations, but rather they are secondary β-relaxations.

Considering the timescales mentioned above, it is reasonable to assume that for the processes observed in the present study, the segmental motions involve uncomplexed dihedrals along the polymer backbone, while complexed dihedrals cannot be involved due to their very long relaxation times. Of the processes that can effectively couple to the density fluctuations and have a direct effect on the observed Brillouin spectra, there are two prime candidates: librational motion and conformational transitions of the backbone dihedrals. The two motions are usually difficult to resolve because they occur on a similar time (frequency) scale. The processes should, however, differ in their temperature dependence. The librational frequencies should be independent of temperature as long as the motion is approximately harmonic, whereas the conformational transition rate typically displays an Arrhenius temperature behavior. Lowering the temperature should therefore separate these two contributions along the frequency axis. We compare the values for τ_1 in our experiment to conformational transition rates calculated using molecular dynamics (MD) simulations for PEO-melt/LiI solutions with very similar concentrations of Li^+ at 90°C.[79] The results from the MD calculation show characteristic times for the conformational transitions of the uncomplexed dihedrals of about 29-34 ps, compared to $\tau_1 \approx 32$ ps in our measurement. The apparent agreement of the timescale, as well as the Arrhenius temperature dependence strongly suggest that at least the first (slower) relaxation observed in our study can be identified with conformational motions involving uncomplexed dihedrals of the polymer backbone. This conclusion is in agreement with the interpretation of the QENS results in PEO-melt/Li-salt complexes,

where the authors also concluded that the fast processes observed "arise from rapid conformal fluctuations of the chain segments between crosslinks; these fluctuations have a largely rotational character and correspond to the dihedral-angle relaxation observed in computer simulations".[69]

As far as the second (faster) relaxation is concerned, its interpretation at this point is much more uncertain, especially because of the unusual temperature dependence. One possible explanation can be sought in the density of the transient crosslinks in the melt and its temperature dependence. Torell *et al.*[80] have studied the temperature dependence of the Brillouin frequency shift in methyl-capped low-molecular-weight PEO-melt/$LiCF_3SO_3$ systems and have suggested that the density of the transient crosslinks is strongly temperature-dependent and increases with decreasing temperature. This result was supported by MD simulation study,[81] where it was found that the strong EO–Li^+ interactions favor complexation of Li^+ cations by long sequences of ether oxygens belonging to a single polymer chain (Fig. 6.13). Although complexation of Li^+ by long EO sequences is enthalpically favored, there are relatively few PEO

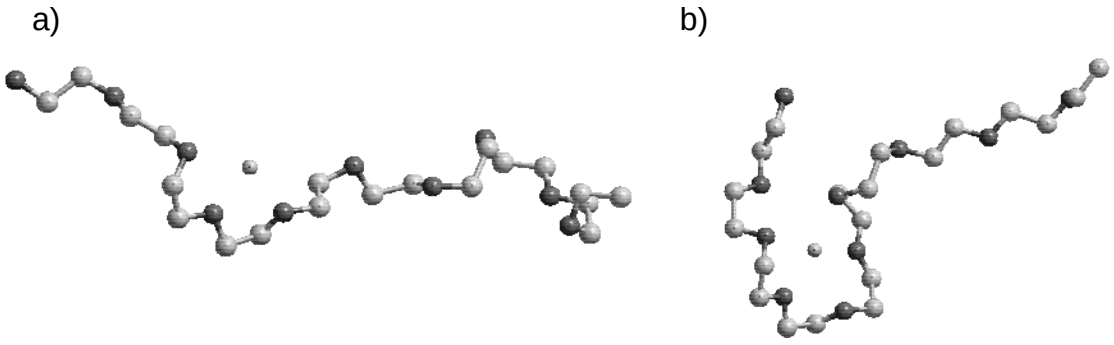

Fig. 6.13 – Lithium cation coordination by a) three and b) by six PEO ether oxygens. Coordination by shorter EO sequences is entropically favored at higher temperatures, while coordination by longer EO sequences in enthalpically favored at lower temperatures.

conformations allowing such complexation. At higher temperatures the entropic penalty for these long sequences increases. The result for dilute salt concentrations (lower than about 15-20%, before saturation is reached) is that at higher temperatures the salt anions compete more effectively with EO in Li^+ complexation, while the PEO chain is entropically forced to adopt shorter EO complexing sequences. Consequently, the number of ether oxygens involved in Li^+ complexation decreases with increasing temperature, while the number of cation-anion recombinations increases. One possible implication for the conformal fluctuations of the chain segments is that with decreasing temperature, the transient crosslink density is increased reducing the number of uncomplexed polymer chain segments between neighboring tie-points. In effect, this will lead to a reduction of the characteristic length of the motions, forcing higher-frequency fluctuations.

To conclude this Chapter, in Fig. 6.14 we show the two relaxations as a function of both temperature and frequency. The plot is calculated using smooth functions for Δ_1, Δ_2, τ_1 and τ_2, obtained with parameters from the best fits to the experimental data. It is only intended for better visualization of the relative strength and position in frequency-temperature space of the two relaxations. The real relaxation in the material is the sum of the two individual components shown here.

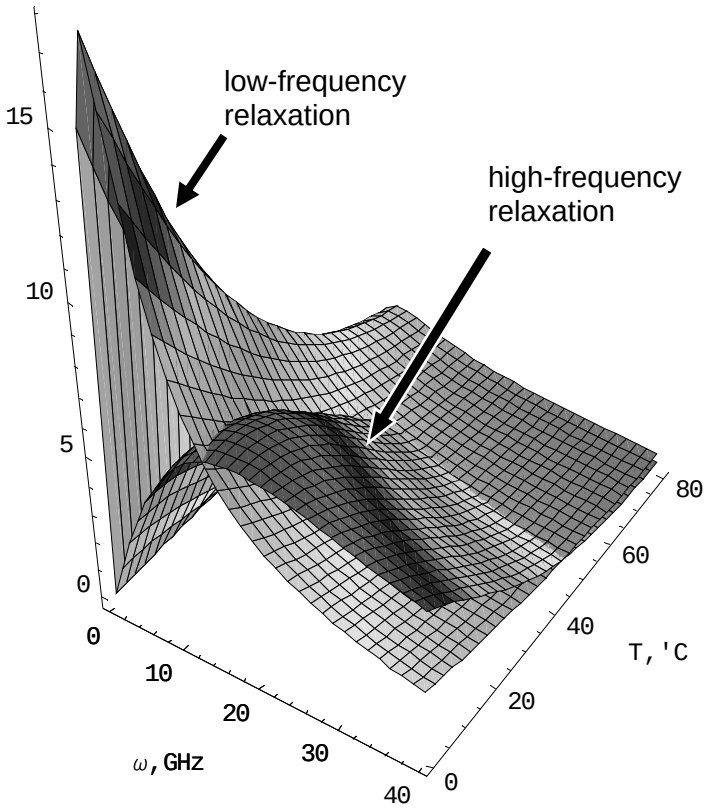

Fig. 6.14 – Slow and fast relaxations in 5wt.-% PEO-melt/$LiClO_4$ electrolytes.

CHAPTER 7

SUMMARY AND CONCLUSIONS

In this dissertation, a comprehensive study of the viscoelastic and dynamic properties of PEO melts and PEO-melt/$LiClO_4$ solutions using the Brillouin light-scattering technique was reported. The properties of the system as a function of composition, temperature and frequency were investigated. The composition range extended from the neat melt up to 31wt.-% salt concentration; the temperature range extended from the melting point of the samples (~40^{o}C) up to 140^{o}C and the frequency range extended from 2 to 10 GHz. It was found that in this temperature-frequency range, both the neat polymer melt and the polymer electrolyte complexes undergo structural relaxation which significantly affected the viscoelastic and dynamic properties of the system, and therefore affected the polymer segmental mobility and the lithium ion transport in the electrolyte. The Rayleigh-Brillouin spectra were analyzed using generalized hydrodynamic theory which considers the effects of structural relaxations in polymeric liquids. The observed relaxation processes were interpreted in the more general framework of relaxation dynamics in glass-forming liquids, allowing the present results to be compared to other experimental observations, such as mechanical and dielectric spectroscopy, neutron scattering, etc.

The temperature dependence of the Brillouin frequency shift and linewidth reveals some of the important characteristics of the relaxation processes probed, such as the relaxation strength and the temperature dependence of the relaxation time. For neat PEO-1K melt, the relaxation has a Maxwell-Debye single-exponential form with $\beta = 1$. Furthermore, the relaxation time, τ, follows an Arrhenius temperature dependence with an activation energy of about 10-11 kJ/mol and τ values from about 9 ps at 140^{o}C to about 22 ps at 40^{o}C. Upon addition of salt, the character of the relaxation persists with $\beta = 1$, and the relaxation time continues to follow Arrhenius temperature dependence. However, with increasing salt concentration, the characteristic time of the process slows down, while the activation energy seems to increase slightly. The slowdown of the dynamics is more pronounced at lower temperatures and the effect of the salt is reduced as the temperature increases. This is consistent with the interpretation emerging from this and other experiments and computer simulations that with increasing temperature, the complexation of lithium ions by ether oxygens is significantly reduced. Another important result of the temperature dependent experiment is the effect of salt concentration on the viscoelasticity of the system. With increasing salt concentration the elastic modulus increases significantly making the medium stiffer at all temperatures, while at the same time the maximum of the storage modulus moves to higher temperatures. This is in agreement with the interpretation that the increased salt concentration results in an increase in the density of transient crosslinks formed by complexation of lithium cations and ether oxygens in the melt. It is also consistent with the increase in the calorimetric glass-transition temperature with increased salt content.

The effects summarized above should have a profound effect on the polymer chain segmental mobility, and therefore on the lithium ion diffusion through the electrolyte. A stiffer polymer network clearly hinders the segmental mobility, which is also reflected in the apparent slowdown in the dynamics and the increased energy barriers of the spontaneous fluctuations in the melt. Qualitatively, this confirms the interpretation of the conductivity vs. salt-concentration data and the assumption that after the initial sharp increase in conductivity due to the rapidly increased number of free charge carriers, the conductivity levels off and eventually decreases primarily due to decreasing ion mobility. On the other hand, the present study provides quantitative measures of various viscoelastic and dynamic parameters, which will prove useful in validating proposed models for the conductivity mechanism in polymer electrolytes.

Even more detailed information about these relaxation processes is obtained using the scattering-angle dependence of the Brillouin spectra. This study became possible after a unique fiber-optic detection and coupling to the Fabry-Perot interferometer was implemented as a part of the light-scattering setup. In essence, the angle-dependent measurement provides the Brillouin frequency shift and linewidth as functions of frequency. The frequency window available in the experimental setup was between 2 and 10 GHz. Applying this technique to 5wt.-% PEO-melt/$LiClO_4$ solutions revealed that the relaxation described above consisted of two underlying relaxations, very close in frequency and impossible to resolve using the temperature-dependence data alone. Both relaxations were identified as secondary β-relaxations with Maxwell-Debye single-exponential character ($\beta = 1$) and Arrhenius temperature behavior of the relaxation time of the slower process. The two-step relaxation is more apparent at lower temperatures. As

the temperature is increased, the strength of the higher-frequency component decreases and the two relaxations become less separated on the frequency axis. Very high sensitivity in the experiment is required to detect the presence of the double-step feature, which was also observed by quasielastic neutron scattering experiments in PEO-melt/LiTFSI solutions. It is possible to extract various characteristic parameters as a function of temperature for both relaxations, e.g. parameters such as the relaxation strength, relaxation time, "relaxed" adiabatic sound velocity, etc. Both relaxations were identified as resulting from conformal fluctuations of the chain segments between transient crosslinks formed by the EO–Li^+ complexation in the melt. These conformal rearrangements include largely twisting and bending segmental motions due to dihedral-angle relaxation involving uncomplexed dihedrals in the polymer backbone. This conclusion is consistent with results from QENS experiments and molecular dynamic simulations.

The results from this work, along with previous PCS experiments done by our group, demonstrate clearly the utility of the dynamic light-scattering techniques in studies of the structural, viscoelastic and dynamic properties of complex macromolecular liquids such as polymer melts and polymer electrolytes. For example, the techniques of mechanical and dielectric spectroscopy, viscometry, rheometry, etc. can only capture the general viscoelastic characteristic of the system as a homogeneous macromolecular liquid. Cooperative (network) behavior due to dipole-dipole interactions in the neat polymer melt are hardly observable by any of these other techniques, and the effects of salt complexation in the polymer electrolytes are only evidenced by effects on the macroscopic viscosity and conductivity. On the other hand, noninvasive light-scattering

techniques are much more sensitive to the existence and properties of the transient network structure resulting from these interactions. As was observed earlier in PCS measurements and is demonstrated in the present work by Brillouin light-scattering, this physical network is formed in the neat PEO melt primarily due to PEO chain dipole-dipole interactions and is enhanced by the EO–Li+ interactions as the salt concentration is increased in PEO-melt/$LiClO_4$ electrolytes. It persists at temperatures from the melting point up to at least 140^{o}C, although the effects of the salt complexation are reduced with increasing temperature. The dynamic characteristics of the transient network were investigated in detail on two very different experimental timescales: from the collective diffusive mode observed on 0.1–10 second timescale in PCS measurements, to the structural segmental relaxation mode with characteristic times on the order of 10^{-11} seconds, observed in Brillouin light-scattering experiments. Only the technique of dielectric spectroscopy can probe a comparable frequency range (~11-12 orders of magnitude), but as was clear in the examples given in the preceding chapters, it cannot detect the presence and the characteristics of the of the transient network structure. Instead, it sees the melt as a homogeneous viscoelastic liquid and detects the main glass-rubber relaxation, but cannot detect the presence of the multiple overlapping β-relaxations. On the other hand, techniques such as neutron scattering and molecular dynamics simulations are sensitive enough to detect the presence of the physical network and its consequences on the liquid dynamics, but they lack the broad range of probe frequencies provided by light-scattering techniques. The implementation of the fiber-optic detection in the light-scattering setup combines several dynamic light-scattering techniques covering a frequency range of about 15 orders of magnitude (not including

possible extension with grating spectrometers to study Raman scattering). In addition, fiber-optic detection made possible implementation of angle-dependent measurements of both the Brillouin frequency and the linewidth using a plane-parallel Fabry-Perot interferometer. A highly desirable future addition to the experimental setup will be the implementation of the techniques of heterodyne or superheterodyne detection which will allow extension of Brillouin light-scattering studies to frequencies below 1GHz where the as yet elusive α-relaxation mode is expected to be observed in the $LiClO_4$-containing PEO melts. Such an extension can be easily incorporated using the fiber-optic detection feature in the present setup.

REFERENCES

[1] For more information see the "white papers" available at: www.avestor.com

[2] F. M. Gray, Polymer electrolytes, Materials Monographs, R. Soc. Chem. (Cambridge, 1997)

[3] C. Berthier, W. Gorecki, M. Minier, M. B. Armand, J. M. Chabagno, P. Rigaud; *Microscopic investigation of ionic conductivity in alkali metal salts-poly(ethylene oxide) adducts*, Solid State Ion. 11(1), 91-95 (1983)

[4] P. G. Bruce, C. A. Vincent, *Polymer electrolytes*, J. Chem. Soc. Faraday Trans. 89, 3187 (1993)

[5] M. A. Ratner, in *Polymer Electrolyte Reviews – 1*, eds. J. R. McCallum and C. A. Vincent, pp. 173-236, Elsevier (London, 1987)

[6] R. Walkenhorst, J. C. Selser, G. Piet; *Long-ranged relaxations in poly(ethylene oxide) melts: Evidence for network behavior*, J. Chem. Phys. 109(24), 11043 (1998)

[7] R. Walter, R. Walkenhorst, M. Smith, J. C. Selser, G. Piet, R. Bogoslovov; *The role of polymer melt viscoelastic network behavior in lithium ion transport for PEO melt/$LiClO_4$ SPEs: the "wet gel" model*, J. Power Sources 89, 168-175 (2000)

[8] R. Walter, J. C. Selser, M. Smith, R. Bogoslovov, G. Piet; *Network viscoelastic behavior in poly(ethylene oxide) melts: Effects of temperature and dissolved $LiClO_4$ on network structure and dynamic behavior*, J. Chem. Phys. 117(1), 417-440 (2002)

[9] R. B. Bogoslovov, Thesis, Graduate College, University of Nevada, Las Vegas (2003)

[10] T. Tanaka, L. O. Hocker, G. B. Benedek; *Spectrum of light scattered from a viscoelastic gel*, J. Chem. Phys. 59(9), 5151-5159 (1973)

[11] J. Sandahl, S. Schantz, L. Borjesson, L. M. Torell, J. R. Stevens; *Elastic and dynamic properties of polymer electrolytes: A Brillouin scattering study of poly(propylene glycol)-$NaCF_3SO_3$ complexes*, J. Chem. Phys. 91(2), 655-662 (1989)

[12] L. M. Torell, S. Schantz, in *Polymer Electrolyte Reviews – 2*, eds. J. R. McCallum and C. A. Vincent, pp. 1-42, Elsevier (London, 1989)

[13] H. Tanaka, T. Sonehara, *New method of superheterodyne light beating spectroscopy for Brillouin scattering using frequency tunable lasers*, Phys. Rev. Lett. 74(9), 1609 (1995)

[14] T. Sonehara, H. Tanaka, *A new method of scattering-angle scanning for optical beating light scattering spectroscopy*, Rev. Sci. Instrum. 73(2), 263 (2002)

[15] H. Tanaka, T. Sonehara, *Superheterodyne light beating spectroscopy for Rayleigh-Brillouin scattering using frequency-tunable lasers*, Rev. Sci. Instrum. 73(5), 1998 (2002)

[16] R. Brown, *Dynamic light scattering using monomode optical fibers*, Appl. Opt. 26(22), 4846 (1987)

[17] J. Rička, *Dynamic light scattering with single-mode and multimode receivers*, Appl. Opt. 32(15), 2860 (1993)

[18] R. B. Bogoslovov, D. P. Shelton, J. C. Selser, G. Piet, S. Peng, *Versatile fiber-coupled system for simultaneous photon correlation spectroscopy and Fabry–Perot interferometry*, Rev. Sci. Instrum. 75(10), 3216 (2004)

[19] M. Born and E. Wolf; *Principles of Optics*, 6-th Ed., Pergamon Press (New York, 1980)

[20] J. M. Vaughan; *The Fabry-Perot Interferometer: History, Theory, Practice and Applications*, Adam Hilger (Bristol, Philadelphia, 1989) and references therein

[21] G. D. Patterson; *Rayleigh-Brillouin scattering in Polymers* in *Methods of experimental physics*, vol.16A, pp.170-204, Academic Press (New York, 1980)

[22] J. R. Sandercock, *Brillouin scattering study of SbSi using a double-passed, stabilized scanning interferometer*, Opt. Commun. 2(2), 73 (1970)

[23] J. R. Sandercock in *Proceedings of the Second International Conference on Light Scattering*, ed. M. Balkanski, p. 9, Flammarion, Paris (1971)

[24] T. Gisler, H. Rüger, S. U. Egelhaaf, J. Tschumi, P. Schurtenberger, and J. Rička, *Mode-selective dynamic light scattering: theory versus experimental realization*, Appl. Opt. 34(18), 3546 (1995)

[25] Suparno, K. Deurloo, Ph. Stamatelopolous, R. Srivastva, J. C. Thomas, *Light scattering with single-mode fiber collimators*, Appl. Opt. 33(30), 7200 (1994)

[26] J. Vanhoudt, J. Clauwaert, *Experimental comparison of fiber receivers and a pinhole receiver for dynamic and static light scattering*, Langmuir 15, 44 (1999)

[27] S. M. Lindsay, I. W. Shepherd, *A high-contrast multipass Fabry-Perot spectrometer*, J. Phys. E: Sci. Instrum. 10, 150 (1977)

[28] J. P. Boon and S. Yip, *Molecular Hydrodynamics*, McGraw-Hill, New York (1980)

[29] J. C. Montrose, V. A. Solovyev, T. A. Litovitz, *Brillouin scattering and relaxation in liquids*, J. Acoust. Soc. Am. 43(1), 117 (1968)

[30] D. A. Pinnow, S. J. Candau, J. T. LaMacchia, T. A. Litovitz, *Brillouin scattering: Viscoelastic measurements in liquids*, J. Acoust. Soc. Am. 43(1), 131 (1968)

[31] T. A. Litovitz and C. M. Davis, *Structural and shear relaxation in liquids*, in *Physical Acoustics* (ed. W. P. Mason), vol. II Part A: *Properties of Gases, Liquids and Solutions*, pp. 281–349, Academic Press (1965)

[32] D. Fioretto, L. Comez, G. Socino, L. Verdini, *Dynamics of density fluctuations of a glass-forming epoxy resin revealed by Brillouin light Scattering*, Phys. Rev. E 59(2), 1899 (1999)

[33] G. Monaco, D. Fioretto, L. Comez, G. Ruocco, *Glass transition and density fluctuations in the fragile glass former orthoterphenyl*, Phys. Rev. E 63, 061502 (2001)

[34] R. D. Mountain, *Thermal Relaxation and Brillouin Scattering in Liquids*, J. Res. Natl. Bur. Stand. 70A(3), 207 (1966)

[35] R. D. Mountain, *Spectral Distribution of Scattered Light in a Simple Fluid*, Rev. Mod. Phys. 38(1), 205 (1966)

[36] B. Berne and R. Pecora, *Dynamic light scattering*, Dover (New York, 2000)

[37] P. J. Carroll, G. D. Patterson, *Rayleigh-Brillouin spectroscopy of simple viscoelastic liquids*, J. Chem. Phys. 81(4), 1666 (1984)

[38] Y.-H. Lin and C. H. Wang, *Rayleigh-Brillouin scattering and structural relaxation of a viscoelastic liquid*, J. Chem. Phys. 70(2), 681 (1979)

[39] G. D. Patterson, *Light scattering from bulk polymers*, Ann. Rev. Mater. Sci. 13, 219, (1983)

[40] G. D. Patterson, P. J. Carroll, J. R. Stevens, W. Wilson, H. E. Bair, *Hypersonic attenuation in poly(dimethylsiloxane) as a function of temperature and pressure*, Macromolecules 17(4), 885 (1984)

[41] R. Kohlrausch, Ann. Phys. (Poggendorf's Annalen, Leipzig) 12, 393 (1847); G. Williams and D. C. Watts, Trans. Faraday Soc. 66, 80 (1970)

[42] C. P. Lindsey, G. D. Patterson, *Detailed comparison of the Williams-Watts and Cole-Davidson functions*, J. Chem. Phys. 73(7), 3348 (1980)

[43] F. Alvarez, A. Alegria, J. Colmenero, *Relationship between the time-domain Kohlrausch-Williams-Watts and frequency-domain Havriliak-Negami relaxation functions*, Phys. Rev. B 44(14), 7306 (1991)

[44] A. Brodin, M. Frank, S. Wiebel, G. Shen, J. Wuttke, H. Z. Cummins, *Brillouin scattering study of propylene carbonate: An evaluation of phenomenological and mode coupling analyses*, Phys. Rev. E, 65, 051503 (2002)

[45] W. Gotze, L.Sjogren, *Relaxation processes in supercooled liquids*, Rep. Prog. Phys. 55, 241 (1992)

[46] A. R. Blythe, *Electrical Properties of Polymers*, p. 38, Cambridge University, London (1979)

[47] E. F. Carome, W. H. Nichols, C. R. Kunsitis-Swyt, S. P. Singal, *Ultrasonic and light-scattering studies of carbon tetrachloride*, J. Chem. Phys. 49(3), 1013 (1968)

[48] G. Fytas, Y.-H. Lin, B. Chu, *Rayleigh-Brilouin spectra of polymer fluids: Polyphenylmethyl siloxane and polydimethylphenylmethyl siloxane*, J. Chem. Phys. 74(6), 3131 (1981)

[49] K. Oda, R. Hayakawa, Y. Wada, *Brillouin-scattering study of acoustic relaxations in liquid toluene*, Jap. J. Appl. Phys. 12(9), 1326 (1973)

[50] G. Williams, D. C. Watts, S. B. Dev, A. M. North, *Further considerations of non symmetrical dielectric relaxation behaviour arising from a simple empirical decay function*, Trans. Faraday Soc. 67, 1323 (1971)

[51] G. Williams in *Dielectric spectroscopy of polymeric liquids: Fundamentals and applications*, ed. J. P. Runt and J. J. Fitzgerald, Chapter 1, pp.3-65, Am. Chem. Soc., Washington, DC (1997)

[52] C. Hansen, F. Stickel, T. Berger, R. Richert, E. W. Fisher, *Dynamics of glass-forming liquids. III. Comparing the dielectric α- and β-relaxation of 1-propanol and o-terphenyl*, J. Chem. Phys. 107, 1086 (1997)

[53] C. Hansen, F. Stickel, R. Richert, E. W. Fisher, *Dynamics of glass-forming liquids. IV. True activated behavior above 2 GHz in the dielectric α-relaxation of organic liquids*, J. Chem. Phys. 108, 6408 (1998)

[54] A. Kudlik, S. Benkhof, T. Blochowicz, C. Tschirwitz, E Rössler, *The dielectric response of simple organic glass formers*, J. Mol. Struc. 497, 201 (1999)

[55] U. Schneider, R. Brand, P. Lunkenheimer, A. Loidl, *Excess Wing in the Dielectric Loss of Glass Formers: A Johari-Goldstein beta Relaxation?*, Phys. Rev. Lett. 84, 5560 (2000)

[56] P. Lunkenheimer, R. Wehn, Th. Riegger, A. Loidl, *Excess wing in the dielectric loss of glass formers: further evidence for a β-relaxation*, J. Non-Cryst. Solids 307-310, 336 (2002)

[57] R. Casalini and C. M. Roland, *Pressure Evolution of the Excess Wing in a Type-B Glass Former*, Phys. Rev. Lett. 91, 015702 (2003)

[58] R. Casalini and C. M. Roland, *Excess wing in the dielectric loss spectra of propylene glycol oligomers at elevated pressure*, Phys. Rev. B 69, 094202 (2004)

[59] F. M. Gray, C. A. Vincent, M. Kent, *A study of the dielectric properties of the polymer electrolyte PEO-$LiClO_4$ over a composition range using time domain spectroscopy*, J. Polym. Sci. B: Polym. Phys. Ed. 27, 2011 (1989)

[60] S. Yano, R. R. Rahalkar, S. P. Hunter, C. H. Wang, R. H. Boyd, *Studies of molecular relaxation of poly(propylene oxide) solutions by dielectric relaxation and Brillouin scattering*, J. Polym. Sci.: Polym. Phys. Ed. 14, 1877 (1976)

[61] A. Schonhals in *Dielectric spectroscopy of polymeric liquids: Fundamentals and applications*, ed. J. P. Runt and J. J. Fitzgerald, Chapter 3, pp.81-106, Am. Chem. Soc., Washington, DC (1997)

[62] B. E. Read, *Mechanical relaxation in some oxide polymers*, Polymer 3, 529 (1962)

[63] T. M. Connor, B. E. Read, G. Williams, J. Appl. Chem. 14, 74 (1964)

[64] C. H. Porter and R. H. Boyd, *A dielectric study of the effects of melting on molecular relaxation in poly(ethylene oxide) and polyoxymethylene*, Macromolecules 4(5), 589 (1971)

[65] Y. Ishida and S. Matsuoka, Am. Chem. Soc., Polymer Preprints 6(2), 795 (1965)

[66] Y. Ishida, M. Matsuo, M. Takayanagi, *Dielectric behavior of single crystals of poly(ethylene oxide)* , J. Polym. Sci. B 3, 321 (1965)

[67] N. G. McCrum, B. E. Read, and G. Williams, *Anelastic and dielectric effects in polymeric solids*, Dover, New York, NY (1991)

[68] G. D. Patterson and J. P. Latham, *Hypersonic relaxation in poly(ethylene oxide)*, Macromolecules 10(6), 1414 (1977)

[69] G. Mao, R. Fernandez Perea, W. S. Howells, D. L. Price, M.-L. Saboungi, *Relaxation in polymer electrolytes on the nanosecond timescale*, Nature 405, 163 (2000)

[70] G. Mao, M.-L. Saboungi, D. L. Price, M. Armand, F. Mezei, S. Pouget, *α-relaxation in PEO-LiTFSI polymer electrolytes*, Macromolecules 35, 415 (2002)

[71] J. E. Mark, ed., *Physical properties of polymers handbook*, AIP Press (Woodbury, NY 1996)

[72] Advanced THermal AnalysiS Laboratory (ATHAS) database: *Recommended data of thermodynamic properties of macromolecules* (1993)

[73] P. A. Rodgers, *Pressure-Volume-Temperature relationships for polymeric liquids: A review of equations of state and their characteristic parameters for 56 polymers*, J. Appl. Polym. Sci. 48, 1061 (1993)

[74] R. K. Jain, R. Simha, *Equation of state of semicrystalline polymers*, J. Polym. Sci. B, Polym. Phys. 17, 1929 (1979)

[75] P. Ferloni, G. Chiodelli, A. Magistris, M. Sanesi, *Ion transport and thermal properties of poly(ethylene oxide)-$LiClO_4$ polymer electrolytes*, Solid State Ionics 18-19, 265 (1986)

[76] P. W. M. Jacobs, J. W. Lorimer, A. Russer, M. Wasiucionek, *Phase relations and conductivity in the system poly(ethylene oxide)-$LiClO_4$*, J. Power Sources 26, 503 (1989)

[77] J. E. F. Rubio, V. G. Baonza, M. Taravillo, J. Núñez, M. Cáceres, *A dynamic light scattering study of the hypersonic relaxation in liquid toluene*, J. Chem. Phys. 115(10), 4681 (2001)

[78] J. Wiedersich, N. V. Surovtsev, E. Rössler, *A comprehensive light scattering study of the glass former toluene*, J. Chem. Phys. 113(3), 1143 (2000)

[79] O. Borodin, G. D. Smith, *Molecular dynamics simulations of poly(ethylene oxide)/LiI melts. 2. Dynamic properties*, Macromolecules 33, 2273 (2000)

[80] L. M. Torell, P. Jacobsson, D. Sidebottom, G. Petersen, *The importance of ion-polymer crosslinks in polymer electrolytes*, Solid State Ionics 53-56(2), 1037 (1992)

[81] O. Borodin, G. D. Smith, *Molecular dynamics simulations of poly(ethylene oxide)/LiI melts. 1. Structural and conformational properties*, Macromolecules 31, 8396 (1998)

VITA

Graduate College
University of Nevada, Las Vegas

Radoslav B. Bogoslovov

Local Address:
2301 Redwood St.; Apt. 3205
Las Vegas, NV 89146-0837

Degrees:

Master of Science, Physics, 2003
University of Nevada, Las Vegas, Las Vegas, Nevada

Master of Science, Engineering Physics, 1996
Sofia University, Sofia, Bulgaria

Publications:

R. B. Bogoslovov, D. P. Shelton, J. C. Selser, G. Piet, S. Peng, Rev. Sci. Instrum. 75(10), 3216 (2004)

S. Peng, J.C. Selser, R. Bogoslovov, G. Piet; J. Chem. Phys. 120(18), 8841 (2004)

R. B. Bogoslovov, Thesis, University of Nevada, Las Vegas (2003)

R. Walter, J. C. Selser, M. Smith, R. Bogoslovov, G. Piet; J. Chem. Phys. 117(1), 417 (2002)

R. Walter, R. Walkenhorst, M. Smith, J. C. Selser, G. Piet, R. Bogoslovov; J. Power Sources 89(2), 168 (2000)

Dissertation Title:

Effects of Temperature and Dissolved $LiClO_4$ on the Viscoelastic and Dynamic Properties of Poly(ethylene oxide), (PEO) Melts

Dissertation Examination Committee:

Chairperson, Dr. James Selser, Ph. D.
Committee Member, Dr. David Shelton, Ph. D.
Committee Member, Dr. Stephen Lepp, Ph. D.
Graduate Faculty Representative, Dr. Boyd L. Earl, Ph. D.